STUDYING THE CORRELATION BETWEEN SWELLING, RADIATION DAMAGE RATE, AND TEMPERATURE IN NUCLEAR REACTOR MATERIALS USING ION IRRADIATIONS

A Dissertation

by

AARON JAMES FRENCH

Submitted to the Graduate and Professional School of
Texas A&M University
in partial fulfillment of the requirements for the degree of

DOCTOR OF PHILOSOPHY

Chair of Committee,	Lin Shao
Committee Members,	Karl T. Hartwig
	Sean McDeavitt
	Pavel Tsvetkov
Head of Department,	Michael Nastasi

December 2022

Major Subject: Nuclear Engineering

ABSTRACT

The radiation damage community has increasingly turned toward ion irradiations to fill a gap arising from the absence of high flux reactors in the testing of alloys for Generation IV reactors and current reactor fleet applications. While ion irradiation has numerous advantages in this testing realm, there are also a number of neutron-atypical variables that distinguish ion damage from neutron damage, including damage rate effects, microchemical phase changes, the injected interstitial effect, and the surface effect. Focusing on the radiation-induced swelling in particular, these atypical variables can significantly alter the observed results of ion experiments from that which would be seen in a reactor environment. This thesis addresses the credibility of ion simulation of swelling applied to neutron environments by presenting a series of ion irradiations on the simple chemical system of relatively pure iron across a range of irradiation conditions. The objective is to clarify the physics of void swelling under ion irradiation and demonstrate a microstructurally-based experimental method for determining, in self-ion-irradiated metals, the regions that are relatively free from injected interstitial and surface effects. A method for determining the optimum combination of dpa damage rate and temperature to avoid these phenomena and more accurately predict neutron-induced swelling trends is also presented. Finally, the results of the developed methodology resulting from the pure iron work is applied to simulate neutron induced swelling using "neutron-preconditioned" samples with experiments performed on AISI 304 SS samples previously irradiated in the EBR-II fast reactor. These specimens were irradiated to higher damage levels over a range of temperatures using 5MeV iron ions. The results

show that preconditioning followed by the right range of ion irradiation parameters can yield incredibly valuable predictions of higher neutron-induced swelling levels without the difficulties arising from trying to achieve such high dose levels in a reactor environment.

DEDICATION

This work is dedicated to all those who have aided and encouraged me over the past many years in my professional and personal advancement. In particular, I extend my thanks to my family, especially my parents Lawrence and Kathleen French, who have been an unwavering source of support and encouragement. I also want to thank my colleagues at the TAMU Accelerator Laboratory for the countless hours of assistance: working through nights and weekends, working long hours at the microscopes, and helping me refine and development my own ideas.

ACKNOWLEDGEMENTS

This work was overseen by a dissertation committee consisting of Professor Lin Shao (committee chair), Professor Pavel Tsvetkov and Professor Sean McDeavitt of the department of Nuclear Engineering and Professor Karl Hartwig of the department of Materials Science and Engineering. I would like to thank them for their support and guidance throughout this research process. In particular, I would like to extend my deepest gratitude to my committee chair and advisor, Professor Lin Shao for the countless hours of assistance, guidance and insight that he has given me. Both through the personal and professional struggles of graduate school, his guiding hand has made this work possible.

I would also like to thank our laboratory manager Xuemei Wang for her guidance and support in the countless hours of experiments. So many of the skills I now possess, I learned under her tutelage. Additionally, without her support in keeping the laboratory running, the experiments detailed in this work would not have been possible.

Dr. Frank Garner also deserves special thanks for all of his guidance, for being an incredibly valuable source of information regarding the radiation damage community, for his countless hours spent reviewing manuscripts and helping refine presentations, and for being a personal friend who supported me in the struggles of graduate school.

Laura Hawkins helped with the electron microscopy on many of the specimens in the following studies, especially during periods of restricted access due to Covid-19. Her work was vital in moving this research forward during this period and included

preparing TEM lamellas, collecting bright field TEM images and gathering EELS thickness data. Adam Gabriel was very helpful in contributing to the ion irradiations of these samples and in keeping the lab running smoothly under Xuemei Wang. Miguel Peña helped collect EELS data for the thickness measurements.

Yongchang Li also deserves special thank for all of his incredible effort. We worked side by side on many research projects together since we were both conducting research on pure iron. Consequently, much of our work has overlapped and he deserves incredible thanks and acknowledgement especially for his work in taking the lead on the single crystal samples. He also was an immense help with a lot of the microscopy, especially collecting EELS data.

Zhihan Hu took the lead on the modeling work under the guidance of Professor Shao and I thank him for all of his efforts there. Hyosim Kim, ChingHeng Shiau, and Assel Aitkaliyeva did the electron microscopy on the radioactive specimens for the last part of this work. Hyosim Kim and Laura Hawkins also helped with some of the analysis on these specimens.

Professor Lin Shao, Frank Garner, Yongchang Li, Zhihan Hu all helped with the writing and editing of the manuscripts that published much of this work. I also want to thank these individuals as well as Adam Gabriel for the extensive dialogue and conversations that helped refine my own thinking on these topics.

I want to thank all the members of TAMU accelerator laboratory who took shifts watching the accelerator and contributed with their time towards making this work

possible. This includes Trevor Parker, Andres Morell Pacheco, Jiangyuan Fan, ChingHeng Shiau, Adam Gabriel, Yongchang Li, Zhihan Hu, and Kenneth Cooper.

Finally, I want to thank all the staff members of both the Materials Characterization Facility and the Microscopy and Imaging Center for all the incredible work they do in keeping the microscopes and equipment available for research use. Their hard work, knowledge, and support are incredibly appreciated.

The work was partially supported by Triad National Security, LLC, through award M2101345-01- 47042-00001.

NOMENCLATURE

ATR	Advanced Test Reactor
BWR	Boiling Water Reactor
dpa	displacements per atom
EBR-II	Experimental Breeder Reactor II
FFTF	Fast Flux Test Facility
FIB	Focused Ion Beam
HIFR	High Flux Isotope Reactor
pka	primary knock-on atom
PWR	Pressurized Water Reactor
SEM	Scanning Electron Microscopy
TEM	Transmission Electron Microscopy
US-LMR	US Liquid Metal Reactor Program
VTR	Versatile Test Reactor

TABLE OF CONTENTS

Page

LIST OF FIGURES

Page

LIST OF TABLES

Page

1. INTRODUCTION *

1.1. The Need for Ion Irradiation Testing in Nuclear Reactor Materials

Reactors subject materials to a very harsh environment with combined effects from radiation, stress, and high temperature. For Generation IV reactors especially, the environment can be extremely harsh with vessel materials needing to withstand even higher total neutron damage levels and higher temperatures. The two most serious materials degradation issues, both related to radiation, are void swelling and irradiation assisted stress corrosion cracking [1] though this project will only focus on the former. Void swelling can cause large dimensional changes in materials with one particularly famous case showing a 33% volume change of a cold worked 316 stainless steel flux cladding tube after ~80 dpa neutron irradiation in the EBR-II reactor [2]. For a power plant, dimensional changes larger than several percent are not tolerable.

As the radiation damage level and temperature increase, the impact of these material degradation issues becomes more prevalent. Thus, the radiation resistance of advanced alloys is a foundational research area in nuclear materials.

---

* A part of this chapter is reprinted with permission from "A quantitative method to determine the region not influenced by injected interstitial and surface effects during void swelling in ion-irradiated metals," Y. Li, A. French, Z. Hu, A. Gabriel, L.R. Hawkins, F.A. Garner, and L. Shao, Journal of Nuclear Materials 573 (2023) 154140

Alloys are being developed and tested for roles as structural components and cladding in future reactors both on the near horizon, such as the Versatile Test Reactor (VTR), and in further out applications including many Generation IV reactor concepts. This research is also vital in supporting the life extension of light water-cooled power-producing reactors.

Some of the materials being developed have a limited data base of neutron irradiation data from the FFTF high flux test reactor such as the D9 austenitic alloy, HT9 ferritic-martensitic alloy and MA957 dispersion-hardened ferritic-martensitic alloy, but these irradiations were completed in the early 1990s. In the interim, there has been no opportunity to test advanced versions of these alloy classes using neutron irradiation or to test various production variants of individual alloys such as 14YWT. The currently available testing reactors, the Advanced Test Reactor (ATR) and the High Flux Isotope Reactor (HIFR), both have relatively low dpa rates and this has caused a restriction in the ability to get very high neutron dpa testing data. For instance, HT-9 has been selected as the main structural material for the VTR, but there is no neutron testing data on this alloy greater than 150 dpa. In the absence of a current high flux neutron test facility, the radiation damage community has employed charged particle irradiation as a surrogate for neutrons with varying levels of success. In particular, the use of self-ion irradiation to very high damage levels is of special utility especially as alloys are being considered for applications in the very high dose regimes seen in Gen IV reactor concepts. It is important then to close the gap between ion irradiation and neutron irradiation testing.

Why can ion irradiations be used to partially fill the deficiency in neutron irradiation facilities? There is a strong background for this claim. In the mid-1970s and early 1980s, charged particle simulation (electrons, protons and self-ions) was a major component of the US Liquid Metal Reactor Program, (US-LMR) providing insight on alloy development and assessment of radiation resistance, and providing direction for the DOE program on what alloys to put into the EBR-II reactor experiments, where dose was accumulated at only ~15 dpa/year or less. When FFTF started providing data at 40-50 dpa per year, the use of charged particle simulation gradually declined in relative importance as data became available from both EBR-II and FFTF at doses <120 dpa: a dose that emerged as the recognized swelling-related limit of austenitic alloys [3]. However, many of the second-generation studies in FFTF on austenitic and high-nickel alloys were based on the results and insights obtained using charged particle irradiation. To support this dual-track approach the USA conducted several comprehensive inter-laboratory programs involving comparison of neutron, electron, proton and self-ion irradiation of identical specimens. These programs were designated as "intercorrelation" experiments [4]. It has been well accepted that electrons, ions and neutrons create equivalent radiation hardening if their doses are normalized using dpa units. However, other irradiation phenomena such as swelling and boundary segregation seem not to be dependent only on dpa, but instead require the use of additional variables, especially dpa rate [1].

This is an important variable to understand because charged particle simulation techniques typically are undertaken at vastly accelerated dpa rates, especially with

respect to void swelling and irradiation creep. This is one of the advantages of ion irradiation testing. A commercial ion accelerator of terminal voltage range of 100 kV to 5 MV provides a beam current of 100 nA to 100 μA. For the most popular NEC tandem accelerator, heavy ions of a few MeV can reach currents of 100s of nanoamps, equivalent to a dpa rate on the order of 10^{-3}dpa/s, which is about five orders of magnitude higher than the typical thermal reactor damage rate. In other words, one day of an ion irradiation is equivalent to more than 10 years of reactor neutron irradiation, as judged by using dpa values.

Building off this past history, the current radiation damage research field has developed accelerator-based ion irradiation into a highly efficient testing method to evaluate the relative irradiation behavior of alloys developed for use in a neutron reactor environment [5-7], especially when considering the phenomenon of void swelling [8-13]. Most recently, ion irradiations up to 500 or 1000 peak dpa have become routine [8-13]. While such high ion-induced dpa values appear to be rather unrealistic, this high level is required to explore the neutron-induced 300-500 dpa levels being considered for some advanced reactor concepts, since the highest-dose portion of an ion-induced damage profile must be discarded due to the impact of a phenomenon called the injected interstitial effect. This subject will be discussed in more detail later.

1.2. Ion Testing Benefits and Neutron Atypical Considerations

Ion irradiation has numerous benefits besides its fast pace. It introduces no or minimal radioactivity, depending on the ion choice and energy, which makes post-

irradiation characterization much easier. The use of self-ions at energies of ≤5 MeV induces no radioactivity. Additionally, ion irradiation can easily allow for different parameters to be decoupled and studied separately, such as temperature, dpa rate, and stress for parametric dependency studies. In reactor-conducted studies, these variables are frequently strongly coupled, and their unique influences are difficult to separate. The combination of ion irradiation and in-situ characterization is therefore a powerful tool to understand fundamental behavior but also to assist in forecasting potential behavior in neutron environments.

However, ion irradiation also has numerous limitations and previous studies have identified a number of neutron-atypical challenges in the use of accelerator-driven ion testing and post-irradiation characterization [5-9]. Some examples of these challenges include:

(1) the surface effect in which a free surface acts as a strong defect sink to remove point defects or defect aggregations and dislocations [14-16];

(2) the surface effect associated with sputtering losses, contributing to a backward movement of the surface with increasing dose [17];

(3) the injected interstitial effect in which the injected ion comes to rest but serves as an unmatched half of a Frenkel pair, producing excessive interstitials at the projected range region, which may significantly affect local microstructural evolution, especially that for void swelling [18];

(4) the dpa rate effect in which the ion flux plays a critical role to change defect evolution and elemental segregation, producing a shift in the temperature regime, especially for void swelling [19-21];

(5) penetration depth limitations which challenge interpretation of subsequent mechanical testing results;

(6) the pulsed beam effect in which a pulsed beam or rastered beam creates microstructures that are quite different from that obtained using a static beam, especially when considering void swelling [22,23];

(7) The anisotropic and compressive stress state of the swelling layer and its consequences on void swelling [24,25];

(8) The added mass of the injected interstitials at the end of the range which thereby contributes to range extension, resulting in a forward movement of the ion-incident surface. Also, the accumulation of void swelling, extending the range of the ion and impacting any measurements of dose vs. depth while also moving the ion-incident surface forward [10,17].

Various methods have been proposed to understand and mitigate the above neutron atypical issues. For the combined influence of surface and injected interstitial effects on void swelling, analytical formulas have been proposed to estimate the depth range of affected regions, thereby identifying the "safe" zone for data analysis [6]. For the dpa rate effect, a "temperature shift" model was proposed to determine equivalent irradiation temperatures that would counteract differences in dpa rate, thereby obtaining defect

"equivalence" and hopefully comparable void swelling [19,21]. These and others will be discussed in further detail later in this work.

1.3. Physics Principles of Radiation Damage and Void Swelling

This work will particularly focus on radiation damage in the form of swelling. Swelling arises from cavity growth due to the accumulation of vacancies created during collision cascades. Collision cascades are caused by high energy incident neutrons or ions hitting matrix atoms and knocking them from their lattice positions with some fraction of the original incident particles energy. These are called primary knock-on atoms (pkas). As these pkas go recoiling through the matrix, they lead to violent nuclei-nuclei collisions. Collision cascades generated along the path of an energetic atom extend over typical distances of a few nanometers [26]. Within a few picoseconds after a cascade is formed, point defects (interstitials and vacancies) begin to recombine and the structure recovers toward its original state. However, a small fraction of the damage will be left behind without recovery. This residual damage accumulates in various ways to form various extended defects, with dislocations being a strongly biased sink for interstitials. Additionally, interstitial diffusion is several orders of magnitude higher than that of vacancies[26]. These factors lead to incomplete defect recombination, void nucleation and material growth.

Understanding the behavior of these defects then plays an important role in being able to accurately model and predict the swelling behavior of alloys both under ion irradiation and extrapolated to neutron reactor environments. It necessary to consider

factors such damage rate (defect generation rate), temperature, diffusivity of the different defect types, chemical microstructural influences on defect behavior, void nucleation rates, varying sink strengths for defects across sink types, and void stability. In addition, the neutron atypical variables mentioned in the previous section can have additional influences on these factors and thus influence how data must be understood if it is to have reliability in predicting swelling trends for the same alloys in neutron reactor environments.

1.4. Scope of the Present Dissertation

The above considerations are quite extensive and the work of many doctoral dissertations; thus, this work has no hope of covering all those factors. Instead, the author of this work hopes to provide insight and new knowledge into 5 keys areas that will further the radiation damage community's fundamental understanding of the physics involved in void swelling, as well as provide useful boundaries to help design ion irradiations and analyze the resulting data for accuracy in predicting trends for neutron reactor swelling behavior. To accomplish these goals this work encompasses several different experimental matrices as well as modeling work. Single crystal and polycrystalline pure iron were used for a number of the experiments to eliminate any chemical complexity and allow for a focus on the fundamental physics of void growth, especially when influenced by the surface and injected interstitial effects. Additionally, preconditioned AISI 304H stainless steel—steel that had previously been irradiated in the EBR-II reactor—was also studied. The five focus areas are:

1) Demonstrating microstructure-based and experimentally derived “safe zones” within the swelling data of ion irradiated pure iron samples that avoids the neutron atypical surface effect and injected interstitials effect. This thus shows a methodology to give boundaries for the region where useful data can be taken to from ion based testing to relate ion and neutron radiation induced swelling trends.
2) Showing how the surface effect in connection with the effective vacancy migration energy is related to the width of the void denuded zone and also provide further clarification on the safe zone surface boundary from an analysis of this denuded zone. This also helps explain certain parallel shifting in certain consecutive dose swelling curves.
3) Demonstrating how there is a threshold that can cause a near surface swelling peak in certain cases as an artifact of the surface effect and providing insight into how to design an experiment with an appropriate dpa rate and temperature to avoid this neutron atypical parameter. This also demonstrates that just because there is swelling data does not necessarily mean that the data accurately predicts trends in neutron reactor enviroments.
4) Demonstrate a novel approach for fast irradiation testing of real reactor materials by using a “preconditioned” material where the void and chemical microstructure are already established through a starting irradiation to low dpa levels in a reactor. Then by accounting for the dpa rate effect and avoiding neutron atypical

effects through only analyzing data from a “safe zone” swelling trends can be extrapolated through subsequent ion irradiations to much high dose levels.

1.5. References

1. G.S. Was, “Fundamentals of radiation materials science: metals and alloys”, Springer, New York, 2007

2. L K Mansur, “Theory and experimental background on dimensional changes in irradiated alloys”, J. Nucl. Mat., 216, 97 (1994)

3. F.A. Garner, Chapter 6: Vol. 10A of Materials Science and Technology: A Comprehensive Treatment, VCH Publishers, 1994, pp. 419-543.

4. F. A. Garner and J. J. Laidler, Proceedings of Workshop on Correlation of Neutron and Charged Particle Damage, Oak Ridge, TN, June 4, 1976, pp. 177-240

5. G.S. Was, Z. Jiao, E. Getto, K. Sun, A.M. Monterrosa, S.A. Maloy, O. Anderoglu, B.H. Sencer, M. Hackett, Emulation of reactor irradiation damage using ion beams, Scripta Materialia 88, 33-36 (2014).

6. Steven J. Zinkle, LL Snead, Opportunities and limitations for ion beams in radiation effects studies: Bridging critical gaps between charged particle and neutron irradiations, Scripta Materialia 143, 154-160 (2018).

7. L. Shao, Jonathan Gigax, Di Chen, Hyosim Kim, Frank A. Garner, Jing Wang, Mychailo B. Toloczko, Standardization of accelerator irradiation procedures for simulation of neutron induced damage in reactor structural materials, J. Nucl. Mat. 409, 251-254 (2017).

8. V.V. Bryk, O.V. Borodin, A.S. Kalchenko, V.N. Voyevodin, V. Ageev, A. Nikitina, V.Novikov, V. Inozemtsev, A. Zeman, F.A. Garner, Ion issues on irradiation behavior of structural materials at high doses and gas concentrations, 11th International Topical Meeting on Nuclear Applications of Accelerators, Bruges, Belgium, 2013.

9. F. A. Garner, L. Shao, M. B. Toloczko, S. A. Maloy, V. N. Voyevodin, "Use of self-ion bombardment to study void swelling in advanced radiation-resistant alloys", Proc. 17th International Conference on Environmental Degradation of Materials in Nuclear Power Systems – Water Reactors August 9–12, 2015, Ottawa, Ontario, Canada.

10. Hyosim Kim, Jonathan G. Gigax, Jiangyuan Fan, Frank A. Garner, T.-L. Sham, Lin Shao, “Swelling resistance of advanced austenitic alloy A709 and its comparison with 316 stainless steel at high damage levels”, J. Nucl. Mater. 527 (2019) 151818.

11. J. G. Gigax, T. Chen, Hyosim Kim, J. Wang, L. M. Price, E. Aydogan, S. A. Maloy, D. K. Schreiber, M. B. Toloczko, F. A. Garner, Lin Shao, "Radiation response of

alloy T91 at damage levels up to 1000 peak dpa", J. Nucl. Mater. 482 (2016) 257-265.

12. Jonathan G. Gigax, Hyosim Kim, Tianyi Chen, F. A. Garner, Lin Shao, "Radiation instability of equal channel angular extruded T91 at ultra-high damage levels", Acta Materialia 132 (2017) 395-404.

13. M. B. Toloczko, F. A. Garner, V. N. Voyevodin, V. V. Bryk, O. V. Borodin, V. V. Mel'nychenko, and A. S. Kalchenko¸ "Ion irradiation-induced swelling of ODS ferritic alloy MA957 tubing to 500 dpa", J. Nucl. Mater. 453 (2014) 323-333.

14. Tai-ni Yang, Chenyang Lu, Ke Jin, Miguel L. Crespillo, Yanwen Zhang, Hongbin Bei, Lumin Wang, The effect of injected interstitials on void formation in self-ion irradiated nickel containing concentrated solid solution alloys, J. Nucl. Mat. 488, 328-337 (2017).

15. Tianyao Wang, Hyosim Kim, Frank A Garner, Kenneth L Peddicord, Lin Shao, The effect of internal free surfaces on void swelling of irradiated pure iron containing subsurface trenches, Crystals 9, 252 (2019).

16. N.Q. Lam, S.J. Rothman, R. Sizmann, Steady-state point-defect diffusion profiles in solids during irradiation, Radiat. Eff. 1974, 23, 53–59 (1974).

17. Jing Wang, Mychailo B. Toloczko, Nathan Bailey, Frank A. Garner, Jonathan Gigax, Lin Shao, "Modification of SRIM-calculated dose and injected ion profiles due to sputtering, injected ion buildup and void swelling", Nuclear Instruments and Methods in Physics Research B 387 (2016) 20–28.

18. Lin Shao, C.-C. Wei, J. Gigax, A. Aitkaliyeva, D. Chen, B.H. Sencer, F.A. Garner, Effect of defect imbalance on void swelling distributions produced in pure iron irradiated with 3.5 MeV self-ions, J. Nucl. Mat. 453, 176-181 (2014).

19. Mansur, L. K. Correlation of neutron and heavy-ion damage. II. The predicted temperature shift if swelling with changes in radiation dose rate. J. Nucl. Mater. 78, 156–160 (1978).

20. C.D. Hardie, C.A. Williams, S. Xu, S.G. Roberts, Effects of irradiation temperature and dose rate on the mechanical properties of self-ion implanted Fe and Fe–Cr alloys, J. Nucl. Mat. 439, 33-40 (2013).

21. S. Taller, G.V. Coevering, B.D. Wirth, G.S. Was, Predicting structural material degradation in advanced nuclear reactors with ion irradiation, Scientific Reports 11, 2949 (2021).

22. Jonathan Gigax, Eda Aydogan, Tianyi Chen, Di Chen, Lin Shao, Y. Wu, W.Y. Lo, Y. Yang, F.A. Garner, The influence of ion beam rastering on the swelling of self-ion irradiated pure iron at 450°C, J. Nucl. Mat. 465, 343-348 (2015).

23. M.T. Myers, S. Charnvanichborikarn, L. Shao, S.O. Kucheyev, Pulsed ion beam measurement of the time constant of dynamic annealing in Si, Phys. Rev. Lett. 109, 095502 (2012).

24. F. A. Garner, G. L. Wire and E. R. Gilbert, "Stress Effects in Ion-Bombardment Experiments," in Radiation Effects and Tritium Technology for Fusion Reactors, CONF-750989, 1976, p. I-474.

25. W. G. Wolfer and F. A. Garner, "Swelling-Induced Stresses in Ion-Bombarded Surfaces: Effects of Crystalline Orientation," J. Nucl. Mater., 85-86 (1979) 583-589.

26. M. Nastasi, J.W. Mayer, J.K. Hirvonen, “Ion-solid interactions: fundamentals and applications”, Cambridge University Press, New York, 1996

2. A QUANTITATIVE METHOD TO DETERMINE THE REGION NOT INFLUENCED BY INJECTED INTERSTITIAL AND SURFACE EFFECTS DURING VOID SWELLING IN ION-IRRADIATED METALS *

2.1. Introduction

The injected interstitial effect is well known to suppress void swelling in ion-irradiated metals, especially in the deeper portion of the ion range [1-10]. The effect arises from two contributions: directly from the implanted ions toward the end of ion range, acting as extra atoms introduced into the matrix and from the spatial depth-dependent difference between collision-produced interstitials and vacancies [11]. Interstitials are distributed slightly deeper than vacancies for each Frenkel pair, and local defect recombination will therefore create excess interstitials, especially over the projected range. The spatial difference between interstitials and vacancies within a Frenkel pair is difficult to obtain using Monte Carlo simulations due to insufficient statistics for reasonable computation times. The difference can be computed using Boltzmann transport code calculations as reported by Shao and coworkers [1].

---

* A part of this chapter is reprinted with permission from "A quantitative method to determine the region not influenced by injected interstitial and surface effects during void swelling in ion-irradiated metals," Y. Li, A. French, Z. Hu, A. Gabriel, L.R. Hawkins, F.A. Garner, and L. Shao, Journal of Nuclear Materials 573 (2023) 154140

Additionally, the injected interstitial effect may include a chemical component if the injected ion is not a major elemental component of the alloy. In the early phase (1970s-1980s) of ion-induced swelling studies, nickel ions were routinely used to study the swelling of iron-base alloys, significantly modifying the composition in the end of range depths of the specimen.

Some insight on the injected interstitial effect can be also gained from other material studies. The injected interstitial effect is well known in the semiconductor industry for modeling of dopant diffusion [12,13]. Dopants such as boron in silicon diffuse exclusively via an interstitial diffusion mechanism in which boron needs the assistance of a silicon interstitial for diffusion [14]. Silicon has a high efficiency for point defect recombination. Hence, the point defects created from collisions are usually ignored in modeling efforts. The interstitials responsible for boron diffusion come from excess interstitials introduced at the projected range. As a good practice in computational simplification, interstitials are assumed to be equal to the implanted dopants. This is called "+1" model in semiconductor modeling [13].

In the "+1" model, Si interstitials are assumed to be equal to implanted ions, regardless of the type of ion species implanted. This is due to the fact that implanted atoms quickly occupy the available lattice locations, but an equal number of new interstitials are created. The same process occurs in metals. Interstitials in metal diffuse as dimers. This means that a newborn interstitial will partially push out a lattice atom to form a dimer. One of the interstitials in the dimer will push the next neighbor to form a new dimer, and the other atom in the original dimer will take the lattice site to become a

substitutional atom. In other words, trace atoms or implanted ions can cease to diffuse, but the induced interstitials will continuously diffuse as dimers.

The major key point of the above discussion is that the diffusivity of the implanted ion species should not be used in modeling the injected interstitial effect. Rather, the diffusivity of self- interstitials should be used. When the self-ion and target metal are the same material, such as Fe into Fe, this distinction is not important, but for a multicomponent material or for injection of an alien ion (e.g., Ni into Fe) this is an important consideration. The second key point is that, since interstitials interact with defect sinks of various types, rate theory modeling needs to be used, considering in detail processes of defect clustering, defect-sink interactions, and sink evolution. Such a full-scale modeling capability at experimental time and length scales, however, is yet to be developed.

Such a complicated issue can be better addressed by conducting an experiment specifically aimed at addressing the combined effects of all surface-related and injected-interstitial related processes as a function of depth and actual damage-produced microstructures for a range of incident-ion energies, while minimizing the effect of other confounding variables. Here, we present a method that can experimentally determine the "safe" analysis zone for void swelling analysis. "Safe" in this usage means that any relationship developed for an ion-neutron correlation will not be contaminated by the two most important neutron-atypical variables, the combined surface processes, and the injected interstitial effect.

In this first study to demonstrate the validity of our approach, we will minimize or avoid entirely the confounding effects of (1) minor element doping effects arising from starting composition, injected beam or carbon contamination, (2) major element segregation associated with multicomponent alloys, (3) crystal orientation and (4) grain boundaries. However, the method can be easily extended to other more complex alloy systems. Most importantly, such experimental results can serve as input to theoretical efforts or benchmarks for modeling efforts.

In this study we used high-purity single crystal Fe as a model system free of grain boundaries, with all specimens presenting the same orientation to the ion beam. The ion irradiation used Fe self- ions of 1 MeV, 2.5 MeV, 3.5 MeV, and 5 MeV, which represent typical beam energies currently or previously used in the ion irradiation community. While lower energies of ≤500 keV were used in many studies in the 1970s-1980s, we did not address these lower energies because one of our previous efforts had already shown that 500 keV irradiations were too heavily influenced by surface and injected interstitial effects [15]. As also noted in that report, sputtering is known to be measurably affected by surface orientation and surface quality.

2.2. Experimental procedure

A <111> oriented single-crystal Fe of purity 99.94+% (purchased from Accumet Materials Inc., Ossining, NY, USA) was used. The high purity and the absence of grain boundaries avoids or minimizes complexity from defect-impurity trapping and defect-grain boundary interactions. The specimens were cut into small pieces of 3 mm×3

mm×1 mm, mechanically polished by using SiC papers from 400 grit down to 4000 grit, and electropolished as the last step. The electropolishing used a twin-jet electro polisher and a solution of 5% perchloric acid in methanol.

Specimens were irradiated with Fe^{2+} ions of 1.0, 2.5, 3.5, and 5.0 MeV, respectively, all to 100 peak dpa, with all specimens oriented to ~7 degrees from the sample normal direction. The 7-degree offset is used to ensure that channeling of the ions does not occur in this single crystal specimen. Otherwise, the ion projected range would be extended and the dose distribution along the ion path would be everywhere lowered in magnitude. The SRIM code does not account for channeling effects on the distribution of damage.

No gases (He, H) were coinjected. The irradiation temperature was 475 ℃, chosen based on our previous studies using pure Fe. A static beam of a spot size of 5 mm in diameter was used to avoid the pulsed beam or rastering effect [16]. The technique of multiple-beam-deflection was used to filter out contaminants (O, N, and C) originating in the accelerator vacuum [17]. The vacuum was kept at 6×10^{-8} torr or better during irradiation. Multiple thermocouples were mounted on the hot stage for temperature monitoring. The temperature fluctuation during irradiations was less than ± 5°C. All irradiations were performed using the same peak dpa rate at 1.2×10^{-3} dpa/s. Fluence determination and damage calculation used the Stopping and Range of Ions in Matter (SRIM) code [18]. The Kinchin-Pease (KP) model was selected [19]. The Fe displacement energy chosen was 40 eV [20]. Table 2.1 shows an important feature of our choice of ion energies. Although all energies and currents were chosen to produce

100 dpa at the peak with comparable peak dpa rates, the dpa rates at the specimen surface increased with decreasing ion energy, introducing a rate dependence that affected the denuded zone width, as will be discussed shortly.

Table 2.1: dpa rates at the surface and at the dpa peak locations for all irradiations.

dpa rate (dpa/s)	**1 MeV**	**2.5 MeV**	**3.5 MeV**	**5 MeV**
At the dpa peak	1.2×10^{-3}	1.2×10^{-3}	1.2×10^{-3}	1.2×10^{-3}
At the surface (averaged from 0-200 nm)	8.91×10^{-4}	4.99×10^{-4}	4.04×10^{-4}	3.06×10^{-4}

The focused ion beam (FIB) technique was used to prepare the transmission electron microscopy (TEM) lamella. 30 keV Ga ions from a Tescan Lyra-3 were used for rough cutting, and 5 keV Ga ions were used for fine thinning. Specimen thickness at multiple positions was measured using electron energy loss spectroscopy (EELS). The statistics of measured thickness variations were included in the error bar calculations. TEM characterization used the FEI Tecnai F20 operated at 200 kV. The ImageJ computer code was used for void analysis [21]. Local swelling was calculated using $Swelling\ \% = V\%/(1 - V\%)$, where $V\%$ is the volume fraction of voids.

2.3. Results and discussion

2.3.1. Measurement of void distributions

Figures 2.1(a-d) present cross-sectional TEM micrographs of Fe irradiated to 100 peak dpa by 5 MeV, 3.5 MeV, 2.5 MeV, and 1 MeV Fe ions, respectively. Voids appear

in all micrographs. Void distributions qualitatively agree with the SRIM-predicted damage profiles (red curves). The SRIM- calculated Fe implant profiles are also plotted (black dashed curves). The damage peak locations are 280 nm (1 MeV), 720 nm (2.5 MeV), 1020 nm (3.5 MeV), and 1305 nm (5 MeV). The projected ranges of Fe ions are 400 nm (1 MeV), 910 nm (2.5 MeV), 1190 nm (3.5 MeV), and 1770 nm (5 MeV). Voids from the 1 MeV irradiation are obviously smaller than the other three irradiations. The largest voids observed from the 1 MeV irradiation are about 15-25 nm, while the largest voids from 2.5 MeV, 3.5 MeV, and 5 MeV irradiations are consistently at 25-35 nm. Figures 2.2(a-d) are corresponding swelling depth profiles of 5 MeV, 3.5 MeV, 2.5 MeV, and 1 MeV irradiations, respectively. It is easily seen that for the three highest ion energies, the suppressive effect of the injected interstitial on swelling is clearly observed in the injected zone and that the maximum swelling along the ion path (but outside the injected zone) is approximately the same for all three ion energies at ~4-5%. For the 1.0 MeV ion case, however, the swelling curve has been significantly depressed over the entire dose range, primarily by the injected interstitial effect.

For all irradiation conditions, void-denuded zones are observed. The widths of the void-denuded zones are 90 nm for 5 MeV, 82 nm for 3.5 MeV, 73 nm for 2.5 MeV, and 61 nm for 1 MeV. The widths were measured from the edges of the nearest voids away from the surface. The decreasing zone width with increasing beam energy appears to be caused by two combined but opposing operating effects. One is the surface sputtering, and the other is the dependence of void-denuded zones on the near-surface dpa rate.

Note that the near-surface sputtering rate increases with decreasing ion energy. Employing the SRIM simulation using the monolayer collision option, the calculated sputtering yields are 0.95 atoms per ion for 5 MeV, 1.16 for 3.5 MeV, 1.35 for 2.5 MeV, and 2.11 for 1 MeV. The calculated sputtering ignores any possibility of beam-specimen orientation dependence. For 100 peak dpa, the calculated equivalent thickness loss at the surface is 11.2 nm for 5 MeV, 13.7 nm for 3.5 MeV, 15.9 nm for 2.5 MeV, and 24.9 nm for 1 MeV. The sputtering calculations used 4.34 eV as the surface binding energy, which is the default value of the SRIM code, and assumes that the Fe atomic density is 8.48×10^{22} atoms/cm^3. If we assume that we can add the sputtering loss to the TEM measured width of void-denuded zones, the widths are 101 nm for 5 MeV, 95 nm for 3.5 MeV, 88 nm for 2.5 MeV, and 77 nm for 1 MeV.

The zone widths gradually decrease with decreasing ion energy, both before and after adding the sputtering loss. This decrease is primarily attributed to local dpa rate differences at the specimen surface. SRIM predictions show that the dpa rate at the specimen surface increases for decreasing incident ion energy, a condition that decreases the denuded width since characteristic depths of vacancy depletion at a surface follow $\Delta x \propto (D/K)^{1/4}$ [22], where D is vacancy diffusivity and K is local dpa rate.

Figures 2.3(a-d) present a statistical analysis of void density and void size at each depth for 1 MeV, 2.5 MeV, 3.5 MeV, and 5 MeV, respectively. On the left side are typical cross-sectional TEM micrographs. Also shown are SRIM-calculated dpa and Fe implant profiles. On the right side are plots of void density as a function of void size at each depth point. The chosen depth interval for statistical analysis is 200 nm for 5, 3.5,

and 2.5 MeV but is only 100 nm for 1 MeV, reflecting the much lesser swelling range at 1 MeV. Note that the analysis regions chosen for data collection are much wider than shown in the selected TEM image. Thus, the void counts at each depth are much larger than the voids present on the presented TEM micrograph. The total number of counted voids are 1300 (for 5 MeV), 2200 (for 3.5 MeV), 1785 (for 2.5 MeV), and 997 (for 1 MeV). At each depth point, the curve height is scaled to the number of voids counted for a given size. Overall, the statistics are good and exhibit Gaussian-like size distributions. The mean void sizes, therefore, can be extracted from each depth with error bars representing the uncertainty of the mean value (not the standard deviation). The dashed curves in the figures are used as guidance to show the changes of mean void size as a function of depth.

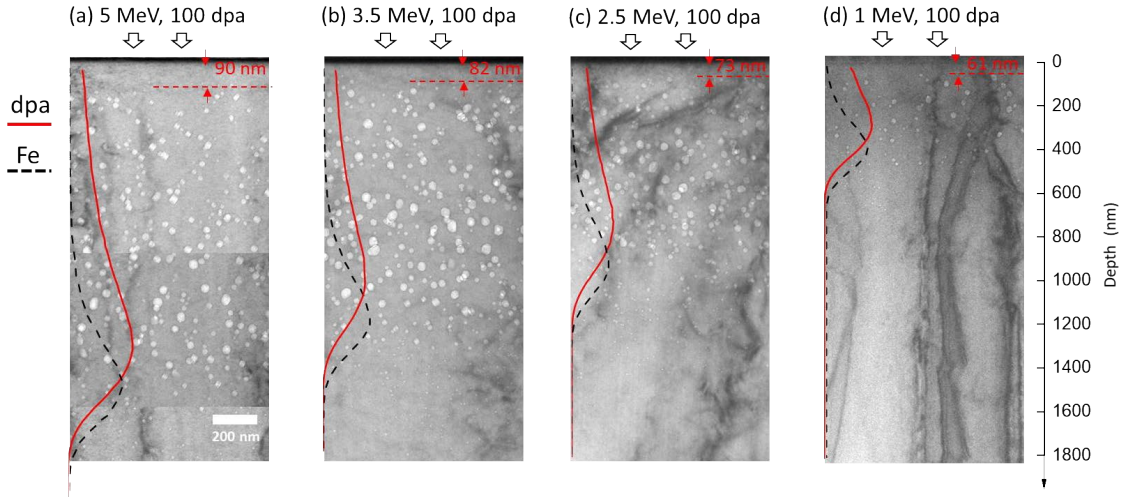

Figure 2.1: Cross-sectional TEM micrographs of Fe irradiated at 475 °C to 100 peak dpa by Fe ions of (a) 5 MeV, (b) 3.5 MeV, (c) 2.5 MeV, and (d) 1 MeV. The arrows indicate the beam irradiation direction. The red curves are SRIM-calculated dpa profiles and the black dashed curves are the implanted Fe profiles.

For all irradiation conditions, void sizes (dashed lines) gradually increase with increasing depth, reaching the maximum at a depth slightly shallower than the depth of the damage peak. Using 5 MeV as an example (as shown in Figure 3a), the mean void size starts at 15 nm at a depth of 100 nm, increases to a maximum of 29 nm at a depth of 1100 nm, and then decreases to 11 nm at a depth of 2000 nm. Comparing all irradiation conditions, the three irradiations using 5 MeV (Figure 3a), 3.5 MeV (Figure 3b), are 2.5 MeV (Figure 3c) are consistent with each having voids of a comparable size range (up to ~40 nm). At 1 MeV (Figure 3d), however, the voids are obviously smaller, indicating that its damage-dependent swelling deviates from that of the other energy irradiations. This observation is to be cited later as one evidence of no "safe" analysis zone at 1 MeV.

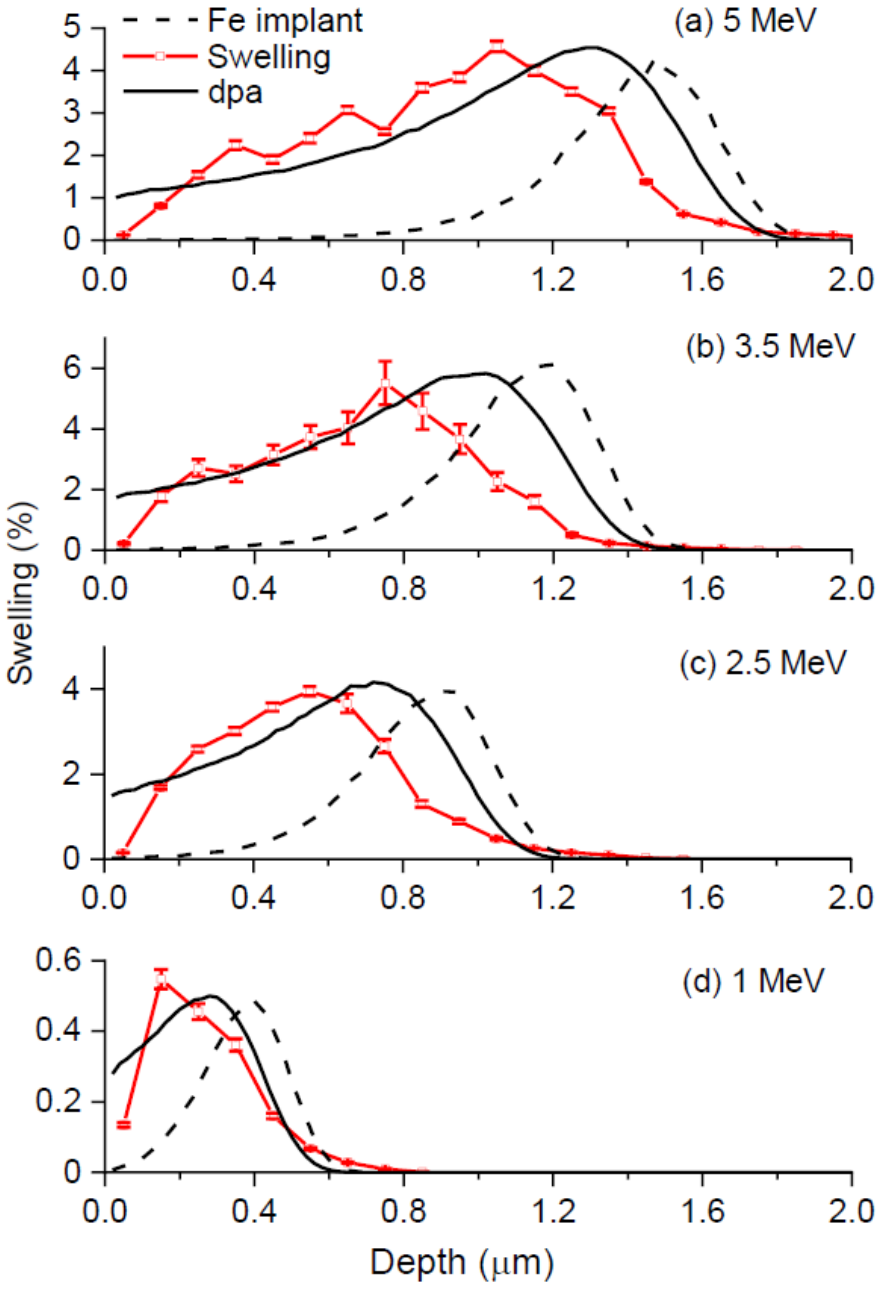

Figure 2.2: Plots of swelling vs. depth in Fe irradiated at 475°C to 100 peak dpa by Fe ions of (a) 5 MeV, (b) 3.5 MeV, (c) 2.5 MeV, and (d) 1 MeV. SRIM-calculated dpa profiles and implanted Fe profiles are also shown.

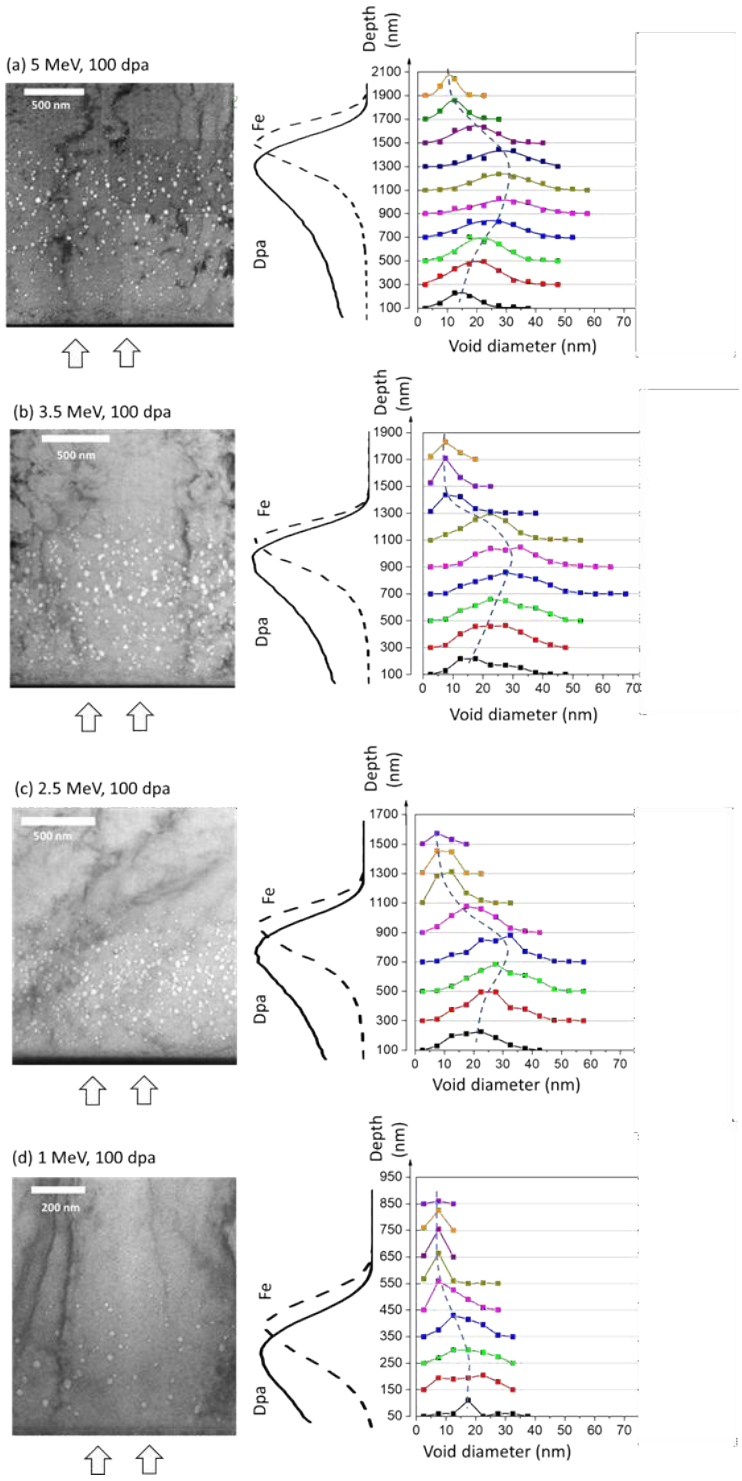

Figure 2.3: Cross-sectional TEM micrographs and void statistical analysis as a function of depth for (a) 5 MeV, (b) 3.5 MeV, (c) 2.5 MeV, and (d) 1 MeV Fe ion irradiation at 475°C. SRIM-calculated dpa and implanted Fe profiles are also shown.

To quantitatively determine the "safe" zone for reliable void swelling analysis, we first present our method to determine the boundary of the surface effect and then we present our method to determine the boundary of the injected interstitial effect. Both methods rely on a statistical analysis of void swelling at each depth point but each uses a different parameter to define the boundary. Forecasting a short summary, we note that for studying the surface effect, void density profiles are used. For studying the injected interstitial effect, void size profiles are used.

2.3.2. Identifying the region affected by combined surface effects

Our method to determine the region affected by the surface effect is to identify the depth where the void density deviates from the "expected" trend, using the plot of void densities vs. local dpa over the whole irradiated region. There are two regions having relatively low local dpa. One is at the near-surface region, and the other is at a depth beyond the Fe projected range. The projected range refers to the peak of Fe implants.

We found that density-dpa curves at deep depths represent the "expected" trend undisturbed by the boundary. Hence it can be used as the reference curve to compare with the near-surface density-dpa curve to identify the point where deviation starts. For this purpose, the easiest way is to plot void density as a function of local dpa so the trend curves at both regions can be directly compared.

Figure 2.4 (left side) compares the plots of void density as a function of depth. For depth-dependent plots, all irradiations show that void densities have steep rises in the near-surface region. Then at depths about 100 to 200 nm depths, the densities begin to

decrease gradually with increasing depth. At the depth roughly corresponding to the peak dpa, void densities reach a minimum. Then the densities recover and gradually increase back to a local maximum at a deeper depth, which is about 200 to 400 nm deeper than the dpa peaks for all four irradiations.

Alternatively, Figure 4 (right side) also shows the void densities as a function of local dpa. Consistent observations were found in all irradiations: (1) void densities decrease with increasing local dpa values, and (2) both regions corresponding to depths less than the dpa peak and depths greater than the dpa peak follow roughly the same dependence on local dpa. Note that the blue arrowed lines refer to the direction of increasing depth towards the dpa peak depths less than the dpa peak, while the red arrowed dotted lines refer to the direction of increasing depth beyond the dpa peak: depth greater than the dpa peak. There are no obvious differences in density-dpa dependence for both depth regions, especially considering scatter associated with observed data fluctuations.

The density-dpa curves in Figure 4 suggests that the injected interstitial effect does not influence void densities (or such effect is minimal or ignorable). The injected interstitial effect may change overall swelling (and consequently, void sizes due to the size-swelling relationship) but does not diminish the number of voids. Otherwise, the curves for depths greater than the dpa peak would be systematically lower than in the depth region shallower than the dpa peak since the peak of the injected interstitial is located deeper than the dpa peak.

If the injected interstitial effect does not reduce void densities, the curve of regions of depths greater than the dpa peak represents the expected density-dpa relationship. The curves are also not influenced by the surface effect due to the obvious reason that they are far away from the surface. Hence the curves can be used as the reference curves to identify the depth where the surface effect causes a deviation. In Figure 2.4, the green arrows point to the depth where the steep rise of the density-dpa curves begins to intersect the reference curves. The measured depths of the intersecting points are 202 nm (for 5 MeV), 193 nm (for 3.5 MeV), 136 nm (for 2.5 MeV), and 110 nm (for 1 MeV). The above depths decrease with decreasing beam energy. Such a trend is expected considering that the near- surface local dpa rates increase with decreasing beam energy. Although the depths of the surface- affected zones are deeper than the void-denuded zones (as observed in this study), both are related to the vacancy profiles at the surface, which have characteristic depths proportional to $(DV/K)^{1/4}$ [23].

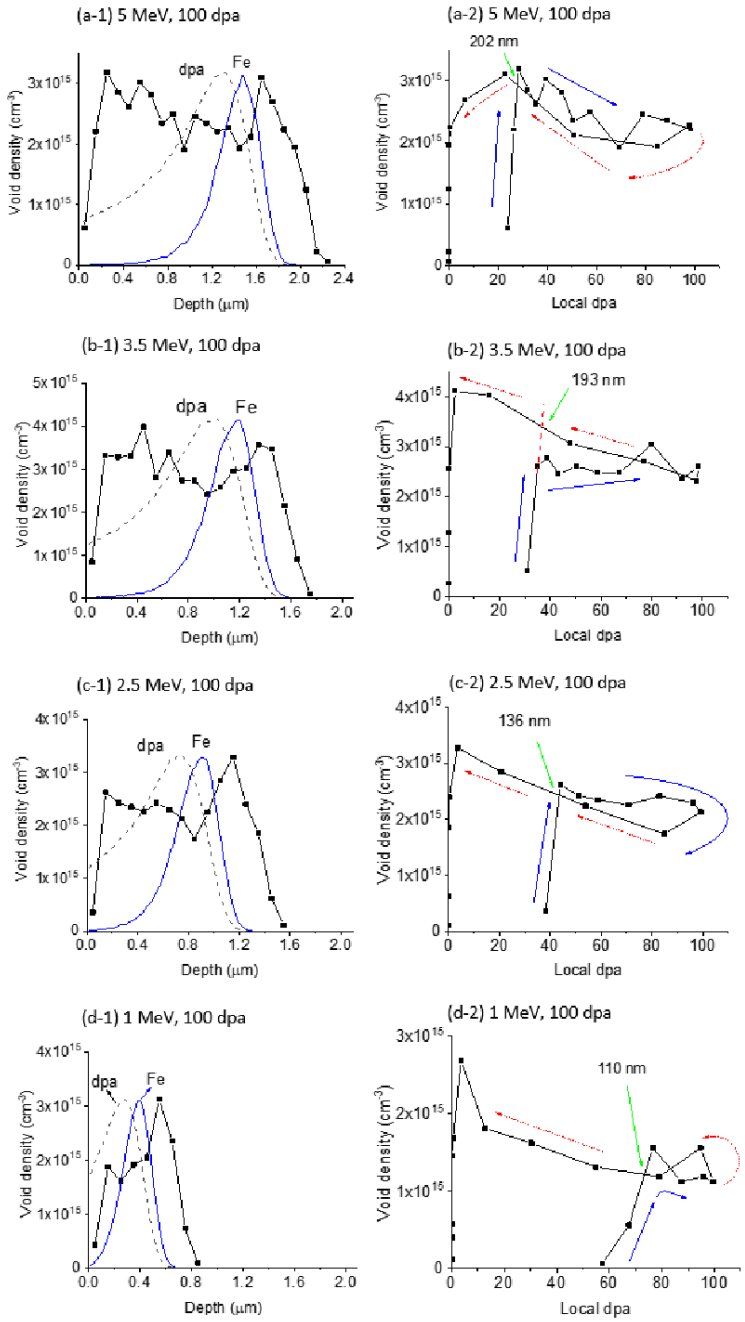

Figure 2.4: Void density as a function of depth for irradiation of (a-1) 5 MeV, (b-1) 3.5 MeV, (c-1) 2.5 MeV, and (d-1) 1 MeV Fe, and void density as a function of local dpa for irradiation of (a-2) 5 MeV, (b-2) 3.5 MeV, (c-2) 2.5 MeV, and (d-2) 1 MeV. The dashed curves are dpa profiles and the solid curves are Fe profiles. The arrowed blue lines refer to increasing depth towards the dpa peak location, and the arrowed red dot lines refer to increasing depth away from the dpa peak location.

2.3.3. Identifying the region affected by the injected interstitial effect

Figure 5 compares void sizes as a function of depth (left) and local dpa (right) for all irradiation conditions. For the depth-dependent void size profiles, all void sizes peak at depths shallower than the dpa peaks as a consequence of the injected interstitial effect. Otherwise, both void sizes and dpa values should peak at the same depth. The impact of the injected interstitial effect is amplified when plotting the void size as a function of local dpa. If there is no injected interstitial effect, voids should grow bigger with increasing local dpa values and reaches their maximum sizes at the peak dpa. Furthermore, the dpa dependence curves should be the same for depth less than the dpa peak and depths greater than the dpa peak. In contrast, all dpa dependence curves in Figure 5 show a common feature that void sizes for depths greater than the dpa peak are systematically smaller than those less than the dpa peak.

Determination of the depth where void sizes begin to deviate from the "expected" curves requires a few assumptions. The first assumption is that the local swelling is proportional to the local dpa, which can be easily justified from the well-known observation that swelling in the post-transient regime increases linearly as a function of dpa, i.e. about 1% per dpa for some FCC iron-base alloys and about 0.2% per dpa for various BCC iron-base alloys [24]. The second assumption is that void swelling under irradiation follows competitive growth Ostwald ripening (also called the non-zero volume approach). In classical (conservative, zero volume approximation) Ostwald ripening theory, precipitates increase their size and decrease their density as a function of time.

Under the non-zero volume approximation, precipitate size changes have an additional dependence on total precipitate volume. The sizes are proportional to the square root of the total volume. One key step to link conservative Ostwald ripening to non-conservative Ostwald ripening is to assume that newly added void volume during ripening can be approximated as the starting void volume. If so, void sizes will evolve as a function of the square root of total swelling, or alternatively, of local dpa values. The dashed lines in Figure 5 are the plot of $\sqrt{dpa}$ dependence with proportionality of $\sqrt{dpa}$ to void sizes employed as a fitting parameter. The dashed lines are used as reference curves to identify the depth when deviation starts. The depths are determined to be 950 nm (for 5 MeV), 750 nm (for 3.5 MeV), and 550 nm (for 2.5 MeV). The 1 MeV curve has decreasing void sizes as a function of depth, which is inconsistent with the trend of the other ion energies. The deviation is considered as evidence that the whole depth region for 1 MeV irradiation is affected by the combined effects of the surface and injected interstitials, especially the latter.

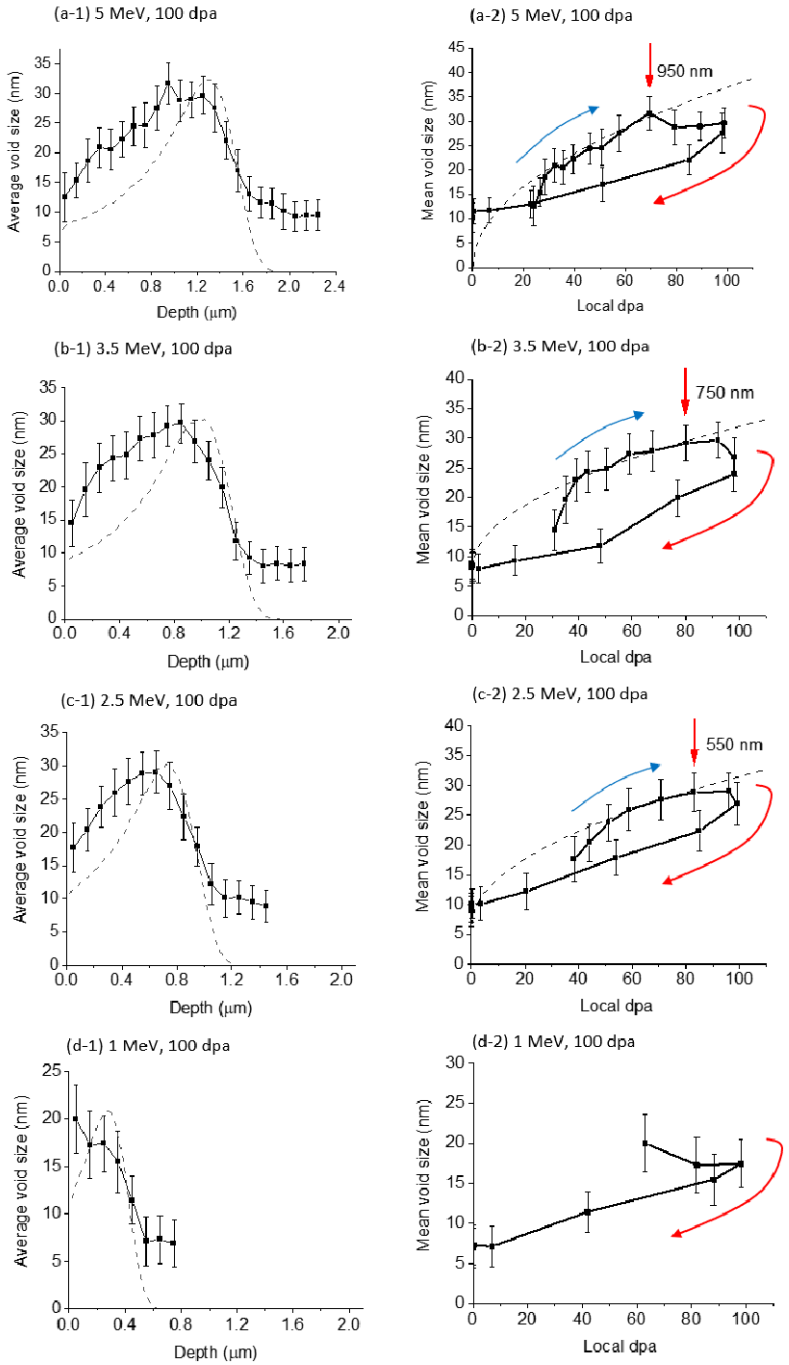

Figure 2.5: Void size as a function of depth for irradiation of (a-1) 5 MeV, (b-1) 3.5 MeV, (c-1) 2.5 MeV, and (d-1) 1 MeV Fe, and void size as a function of local dpa for irradiation of (a-2) 5 MeV, (b-2) 3.5 MeV, (c-2) 2.5 MeV, and (d-2) 1 MeV.

2.3.4. Mapping the safe analysis zone

Combining all above analyses, Figure 2.6 provides a map showing the region which is “safe” for swelling analysis, at least with respect to precluding strong effects of surface or injected interstitial effects. The empty circles show the boundary of void-denuded zones. The solid squares indicate the boundary of surface-affected zones. The red circles denote the boundary of injected-interstitial-affected zones. The tringles refer to the projected range of Fe implants. The shadowed blue region represents the safe zone which is not strongly affected by either the surface effect or the injected interstitial effect. Note there is no safe zone for 1 MeV irradiation determined in this experiment. Therefore, it is reasonable to assume that ion energies less than 1 MeV are also not safe for developing ion-neutron correlations, casting some caution on data produced in earlier studies using ions of energies $\leq$ 500 keV.

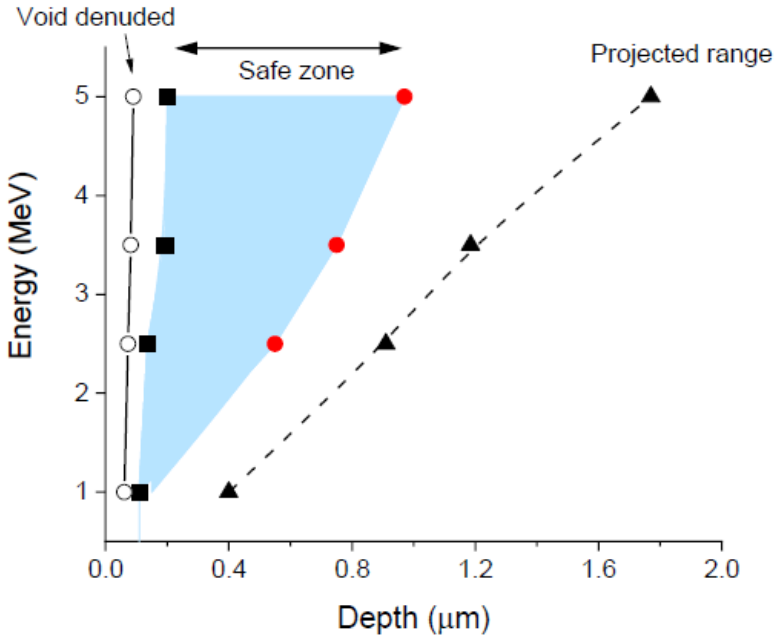

Figure 2.6: Safe zones determined in pure Fe irradiated by self-ions of different energies. The empty circles refer to the void-denuded zones. The solid squares indicate the boundary of the surface- affected zones. The solid circles denote the boundary of the injected interstitial effect, The triangles refer to the projected ion ranges. The shadowed region shows the safe zone.

The surface effect influences a wider region (solid square) beyond the void-denuded zone (hollow circle). The former is about twice the latter, as an approximation from our measurements. Remember that the measured boundaries of the surface-affected zones are 202 nm (for 5 MeV), 193 nm (for 3.5 MeV), 136 nm (for 2.5 MeV), and 110 nm (for 1 MeV). We explain such energy dependence due to the increasing near-surface dpa rates at lower ion energies, causing the reduction of both void-denuded zones and surface-affected zones. The near-surface K values, averaged from depth 0 to 600 nm, are 3.3×10^{-4} dpa/s for 5 MeV, 4.5×10^{-4} dpa/s for 3.5 MeV, 5.6×10^{-4} dpa/s for 2.5 MeV, and 1.1×10^{-3} dpa/s for 1 MeV. Using 1 MeV for the normalization, the

normalized $(D\ /K)^{1/4}$ values are 1.4, 1.3 and 1.2 for 5 MeV, 3.5 MeV, and 2.5 MeV, respectively. The normalized depth of surface-affected zones (after adding the additional depth removed by sputtering) is 1.6, 1.5, and 1.1 for 5 MeV, 3.5 MeV, and 2.5 MeV. These two sets of ratios are in good agreement.

The boundaries of the injected-interstitial-affected zones (red circles), based on the measurements from Figure 5, are 970 nm (for 5 MeV), 750 nm (for 3.5 MeV), and 550 nm (for 2.5 MeV). The projected ranges (triangles) from SRIM calculations are 1770 nm for 5 MeV, 1185 nm for 3.5 MeV, and 910 nm for 2.5 MeV. If using the projected range for normalization, the normalized depth of the injected-interstitial-affected zones is 0.5-0.6.

Towards understanding the effect of the injected interstitials, figures 2.7(a-d) compare the size dependence on swelling for 5 MeV, 3.5 MeV, 2.5 MeV, and 1 MeV irradiations, respectively. The arrows point in the direction of increasing depth, with solid blue arrows referring to depths less than the peak dpa location and red dotted arrows referring to depths greater than the peak dpa location. Considering the error bars, there is no sensitivity on whether depths are shallower or deeper than the dpa peak locations. Both depth regions follow the same swelling dependence. Curves of 5 MeV, 3.5 MeV, and 2.5 MeV irradiation are similar to each other. If all three high energy ion curves are plotted together, they are well represented by one single swelling dependence curve. Note that in these irradiation conditions, voids consistently have the largest sizes of 25-30 nm at highest swelling level and have the smallest size of 5-10 nm at the lowest

swelling level. The exception observed is for the 1 MeV irradiation because the injected interstitial effect influences the entire damaged region.

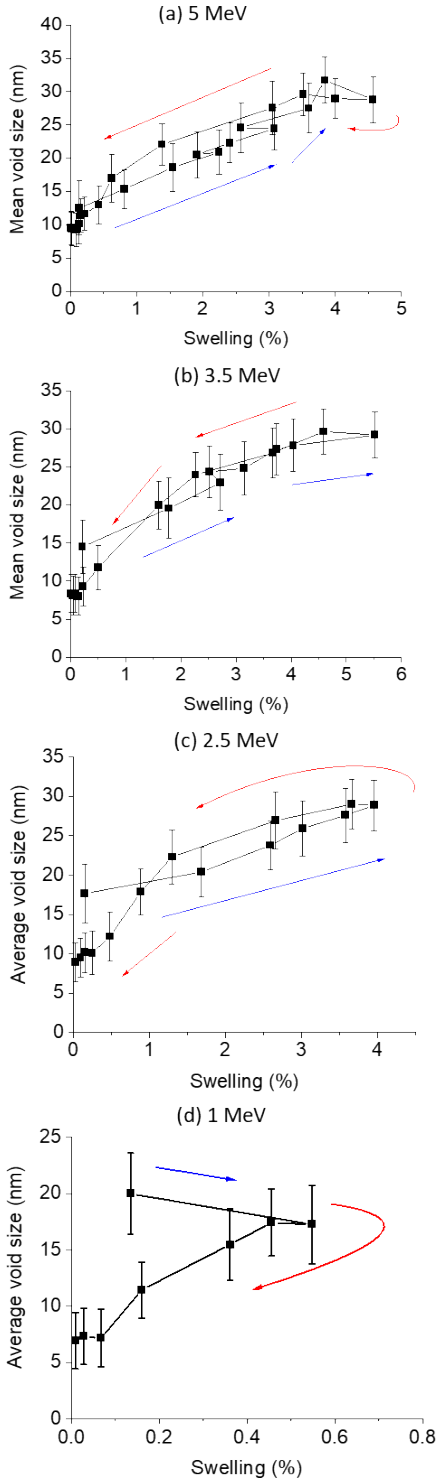

Figure 2.7: Void size as a function of local swelling for Fe irradiation of (a) 5 MeV, (b) 3.5 MeV, (c) 2.5 MeV, and (d) 1 MeV.

The above observation suggests that the primary effect of the injected interstitial is to reduce the local swelling. Since very small voids are observed (Figures 1 and 3) in the injected zone the most pronounced effect must be on void growth. Even in the region heavily influenced by the injected interstitial effects, both void size and void density follow the behavior expected from ripening theory.

Using Figure 2.6 as guidance to include points within the safe zone only, Figure 2.8 plots swelling as a function of local dpa for 2.5 MeV, 3.5 MeV, and 5 MeV. Note that the data for 1 MeV irradiation is not included since there is no safe zone for this ion energy. All data points within the "safe analysis zone" reasonably converge to the same curve. The average slope, corresponding to the swelling rate, is 0.07 % per dpa. The curve further extrapolates to zero dose, implying no incubation period. This derived slope and intercept combination are currently thought to be rather surprising since our earlier studies imply showed measurable incubation periods and post-transient (post-incubation) swelling rates on the order of 0.2% per dpa with incubation doses on the order of 20 dpa [1,16]. It appears that in this experimental series, especially for the dpa rate and temperature selected, that we have ventured into a different swelling regime. Ongoing studies are in progress at other dpa rates to explore this possibility.

The proposed method demonstrated in this paper can be used in arbitrary ion-target systems to determine the "safe" data extraction zone in swelling analyses. The method does not require complicated modeling to simulate either the surface effect or the injected interstitial effect. The capability to accurately identify the safe zone is critical for any attempt to use local dpa dependence to predict swelling as a function of damage

level, especially if the intent is to apply ion data to a neutron environment. If swelling data are badly influenced by the surface effect, the true growth rate will be underestimated since the lower dpa region has suppressed swelling. Also, as shown in the 1 MeV irradiation case, there is no safe zone even when voids appear.

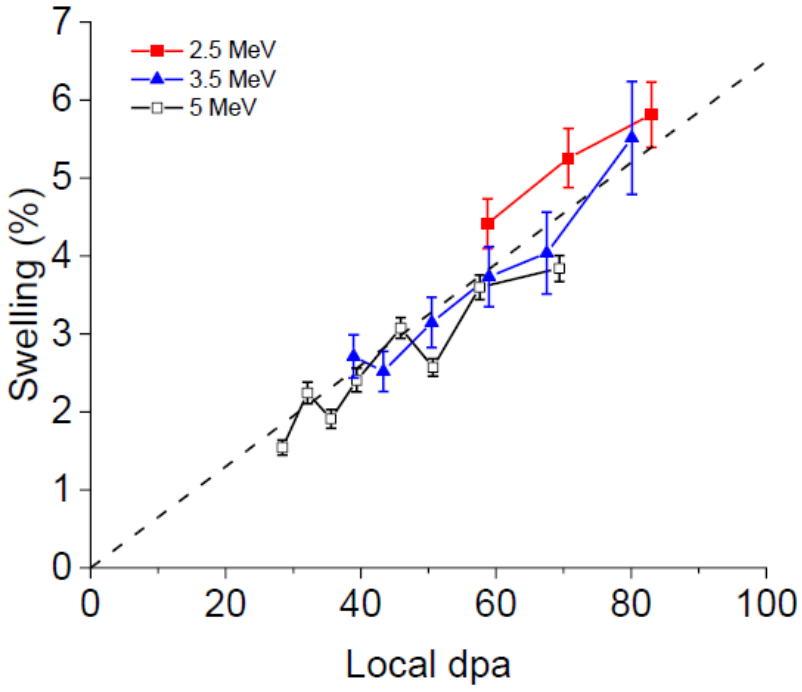

Figure 2.8: Void swelling as a function of local dpa in Fe irradiated by 2.5 MeV, 3.5 MeV, and 5 MeV ions up to 100 peak dpa. Only data points derived in the safe zones identified from Figure 6 are included. Note the excellent agreement over the 2.5-5 MeV range.

2.4. Conclusions

In summary, we have proposed a method to quantitatively determine the "safe" zone in ion- induced void swelling analysis based on expected non-conservative Ostwald

ripening behavior and the expected void size and density evolution as a function of damage level. The goal is to define a damage zone width and location where the effects of surface and injected interstitial are not influencing the swelling. We have demonstrated the efficacy of the method in a simple alloy system, pure iron, but expect that the method can be used for more complex metals. The following conclusions were found.

(1) Void density shows a trend turnover in the near-surface region, which can be used to identify the boundary where the surface effect ends. The measured boundary widths slightly increase with increasing Fe ion energy (from 1 MeV to 5 MeV) due to local dpa rate differences at the specimen surface.

(2) The above-measured boundary depths are deeper than the void-denuded zone width, suggesting whether voids appear or not cannot be used as a single criterion to judge the magnitude of the surface effect. Voids can be produced and remain stable even when located in a gradient of surface influence.

(3) The void size dependence as a function of local dpa level exhibits a hysteresis-like behavior in which voids at depths beyond the peak dpa location are systematically smaller than found at depths shallower than the peak dpa location. The trend reversal location of void size changes can be used to quantitatively determine the boundary depth where the injected interstitial effect begins to significantly influence swelling.

(4) The above boundary depths for the injected interstitial effect increase with increasing ion energy and are about 0.5-0.6 of the injected range of Fe ions, an observation which can be used as an approximation in studies on other alloys.

(5) The void size changes as a function of local swelling do not exhibit a sensitivity on whether corresponding depths are shallower or deeper than the dpa peak locations. The void sizes follow roughly the same dependence curve through the whole depth region, suggesting that the injected interstitial effect reduces swelling but does not directly affect void sizes. The void sizes are primarily tuned by the amount of swelling.

(6) Pure iron irradiated by 1 MeV Fe ions shows no safe zone in void analysis, although voids form. Self-ion irradiation testing at energies ≤1 MeV may yield valuable information concerning some facets of irradiation behavior, but the application of swelling data at these energies to confident predictions of neutron-induced swelling are very questionable.

(7) If the ion energy is sufficiently high enough, 2.5 MeV or greater, then the credibility of using ion simulation for predictions of neutron-induced swelling are enhanced using this experimental technique.

2.5. References

1. Lin Shao, C.-C. Wei, J. Gigax, A. Aitkaliyeva, D. Chen, B.H. Sencer, F.A. Garner, Effect of defect imbalance on void swelling distributions produced in pure iron irradiated with 3.5 MeV self-ions, J. Nucl. Mat. 453, 176-181 (2014).

2. L. K. Mansur, and M. H. Yoo, “Advances in the theory of swelling in irradiated metals and alloys”, J. Nucl. Mater. 85&86 (1979) 523-532.

3. F. A. Garner, "Impact of the Injected Interstitial on the Correlation of Charged Particle and Neutron-Induced Radiation Damage", J. Nucl. Mater., 117 (1983) 177-197.

4. M. P. Short, D. R. Gaston, M. Jin, L. Shao, F. A. Garner, "Modeling injected interstitial effects on void swelling in self-ion experiments', J. Nucl. Mater., 471 (2015) 200-207.

5. C. Sun, F. A. Garner, L. Shao, X. Zhang, S. A. Maloy, "Influence of injected interstitials on the void swelling in two structural variants of 304L stainless steel induced by self-ion irradiation at 500°C, Nucl. Instr. Meth. Res. B 409 (2017) 323-327.

6. E. Kuramoto, N. Yoshida, N. Tsukuda, K. Kitajima, N.H. Packan, M.B. Lewis, L.K. Mansur, Simulation irradiation studies on iron, J. Nucl. Mater., 103&104, 1091 (1981)

7. D.L. Plumton, W.G. Wolfer, Suppression of void nucleation by injected interstitials during heavy ion bombardment, J. Nucl. Mater., 120, 245-253 (1984)

8. E.H. Lee, L.K. Mansur, M.H. Yoo, Spatial variation in void volume during charged particle bombardment — the effects of injected interstitials, J. Nucl. Mater., 85&86, 577-581 (1979).

9. D.B. Bullen, G.L. Kulcinski, R.A. Dodd, Swelling suppression by injected self-interstitials, Nucl. Instr. Methods Phys. Res., B10/11, 561-564 (1985)

10. J.B. Whitley, G.L. Kulcinski, P. Wilkes, H.V. Smith Jr., The depth dependent damage profile in nickel irradiated with nickel or copper ions, J. Nucl. Mater. 79, 159-169 (1979)

11. J. G. Gigax, T. Chen, Hyosim Kim, J. Wang, L. M. Price, E. Aydogan, S. A. Maloy, D. K. Schreiber, M. B. Toloczko, F. A. Garner, Lin Shao, "Radiation response of alloy T91 at damage levels up to 1000 peak dpa", J. Nucl. Mater. 482 (2016) 257-265.

12. L. Shao, X. Lu, X. Wang, I. Rusakova, J. Liu, W.-K. Chu, Retardation of boron diffusion in silicon by defect engineering, Appl. Phys. Lett., 78, 2321-2323 (2001).

13. M. Giles, Transient phosphorus diffusion below the amorphization threshold, J. Electrochem. Soc. 138, 1160 (1991).

14. Lin Shao, Jiarui Liu, Quark Y. Chen, Wei-Kan Chu, Boron diffusion in silicon: the anomalies and control by point defect engineering, Materials Science and Engineering: R: Reports 42, 65-114 (2003).

15. Jing Wang, Mychailo B. Toloczko, Nathan Bailey, Frank A. Garner, Jonathan Gigax, Lin Shao, "Modification of SRIM-calculated dose and injected ion profiles due to sputtering, injected ion buildup and void swelling", Nuclear Instruments and Methods in Physics Research B 387 (2016) 20–28.

16. Jonathan Gigax, Eda Aydogan, Tianyi Chen, Di Chen, Lin Shao, Y. Wu, W.Y. Lo, Y. Yang, F.A. Garner, The influence of ion beam rastering on the swelling of self-ion irradiated pure iron at 450°C, J. Nucl. Mat. 465, 343-348 (2015).

17. Jonathan G. Gigax, Hyosim Kim, Eda Aydogan, Frank A. Garner, Stu Maloy, Lin Shao, Beam- contamination-induced compositional alteration and its neutron-atypical consequences in ion simulation of neutron-induced void swelling, Mat. Res. Lett. 5, 478-485 (2017).

18. J.F. Ziegler, M.D. Ziegler, J.P. Biersack. "SRIM–The stopping and range of ions in matter (2010). 268, 1818-1823 (2010).

19. Roger Stoller, Mychailo B. Toloczko, Gary S. Was, A.G. Certain, S. Dwaraknath, Frank A. Garner, On the use of SRIM for computing radiation damage exposure, Nucl. Instrum. Methods Phys. Res. B 310, 75-80 (2013).

20. A.Yu. Konobeyev, U. Fischer, Y.A. Korovin, S.P. Simakov, Evaluation of effective threshold displacement energies and other data required for the calculation of advanced atomic displacement cross-sections, Nuclear Energy and Technology 3, 169–175 (2017).

21. C.A. Schneider, W.S. Rasband, K.W. Eliceiri, "NIH Image to ImageJ: 25 years of image analysis". Nature Methods 9, 671-675, 2012.

22. Hyosim Kim, Jonathan G. Gigax, Jiangyuan Fan, Frank A. Garner, T.-L. Sham, Lin Shao, “Swelling resistance of advanced austenitic alloy A709 and its comparison with 316 stainless steel at high damage levels”, J. Nucl. Mater. 527 (2019) 151818.

23. N.Q. Lam, S.J. Rothman, R. Sizmann, Steady-state point-defect diffusion profiles in solids during irradiation, Radiat. Eff. 1974, 23, 53–59 (1974).

24. F. A. Garner, M. B. Toloczko and B. H. Sencer, “Comparison of Swelling and Irradiation Creep Behavior of fcc-Austenitic and bcc-Ferritic/Martensitic Alloys at High Neutron Exposure,” J. Nucl. Mater., 276 (2000) 123-142.

3. EFFECT OF FREE SURFACES ON NEAR-SURFACE VOID SWELLING IN SELF ION-IRRADIATED FE AT VARIOUS ION ENERGIES, PEAK DPA RATES, AND TEMPERATURES

3.1. Introduction

As referenced in the introduction, understanding the effects of free surfaces (particularly seen as the void surface effect) in void swelling is important for both ion irradiation testing of bulk materials (for which the surface effect needs to be avoided) and for materials engineering (for which internal boundaries/surfaces are intentionally introduced to maximize the defect removal) [1,2]. The knowledge obtained can extend to other defect sinks, such as grain boundaries, since a grain boundary is a neutral sink and can pin defect concentrations at boundary equilibrium values if boundary trapping sites are not saturated [3-5].

One characteristic feature of the surface effect is the formation of void denuded zones in ion-irradiated or neutron-irradiated metals [6-11]. Analytical solutions from rate theory of the near surface point defect concentrations during irradiation show that the concentrations reduces exponentially as the surface is approached within this region [12]. The characteristic width of the denuded zone region, Δx, is approximated to be proportional to $(D_V/K)^{1/4}$, where D_V is vacancy diffusivity and K is the defect generation rate. The K dependence of void denuded zones has been observed in reactor irradiation experiments under different neutron fluxes [13].

Discrepancies, however, exist from previous studies. One discrepancy is the activation energy that governs the temperature dependence of Δx, and a second is the surface effect on a narrow region immediately next to the void denuded zone. Previous studies noted that the activation energy ($E_{\Delta x^4}$) in the Arrhenius description of Δx^4 is largely different from the vacancy migration energy (E_V^m) in some experiments. From Ni + Ni dual ion beam irradiations of Fe and Fe-Cr alloys [14], the E_V^m estimated from $E_{\Delta x^4}$ is 1.22 eV is 1.22 eV for Fe-10Cr, 1.31 eV for Fe-14Cr, and 0.96 eV for Fe. In comparison, the theoretical values from density functional theory are 0.43 eV for Fe-10Cr, 0.51 eV for Fe-14Cr, and 0.91 eV for Fe [15]. The cause of the discrepancy was unclear.

For the regions immediately next to the surface void denuded zones, a few studies have shown that the swelling was enhanced in neutron irradiated metals such as aluminum and copper [16-18]. Similar observations were found in ion irradiated metals [19, 20]. The phenomenon was explained by one-dimensional glissile interstitial loop migration towards a boundary [21]. As we will further discuss in the next section, it was found, however, that the appearance of a surface swelling peak depends on temperature and dpa rates [22]. A surface swelling peak appears for relatively low temperature irradiations, and disappears for high temperature irradiations [22]. For a low temperature irradiation in which temperature is not adjustable to eliminiate this surface swelling peak, the dpa rate can be reduced which will cause the surface swelling peak to disappear [22]. The transition of the surface swelling peak to a deep swelling peak (the

swelling peak begins to follow the dpa profile) and its dependence on temperature and dpa rates were also observed from rate theory calculations [22].

The present section is motivated by two purposes: one is to evaluate the activation energy and temperature/dpa rate dependence of Δx^4, and the other is to evaluate the region beyond the void denuded zones in a similar manner but different approach to the previous section of this work. Both concern irradiation parameter optimization and data interpretation in ion irradiation testing. The study used pure iron as a model system since it is free of precipitation and the defect kinetics of iron have previously been well studied. The self-ion irradiation also avoids the complexity from ion doping and local composition changes.

3.2. Experimental procedure

The irradiation uses a large matrix with different doses, dpa rates, ion energies, and temperatures. For energy dependency studies, samples were irradiated by Fe^{2+} ions of 1 MeV, 2.5 MeV, 3.5 MeV, and 5 MeV, all at 475°C and all at a fixed peak dpa rate of 1.2×10^{-3} dpa/s. Note that 475℃ was selected as the maximum swelling temperature of Fe [30]. For temperature and dpa rate studies, samples were irradiated with a fixed beam energy of 5 MeV, at temperatures of 425°C, 475°C, and 525°C, and at peak dpa rate of 2×10^{-4} dpa/s, 1.2×10^{-3} dpa/s, and 6×10^{-3} dpa/s, respectively. The ion fluences were equivalent to 50 and 100 peak dpa, respectively, for each energy/temperature/dpa rate condition.

The experiment includes two sets of Fe samples as a combined study to evaluate the irradiation parameter sensitivity of a large testing matrix. For studying temperature dependence and dpa rate dependence, we used a polycrystalline iron sample of a purity of 99.8% (obtained from Goodfellow, Pittsburgh, Pennsylvania, USA). The sample contains 140 appm C. The grain sizes of poly-Fe range from about 5 μm to 50 μm. For studying ion beam energy dependence at the fixed temperature of 475°C, we used <111> oriented single-crystal Fe of purity 99.94+% (obtained from Accumet Materials Inc., Ossining, NY, USA). The single-crystal Fe contains 120 appm C. Both sets of samples were cut into small pieces of about 4 mm ×4 mm. The single-crystal samples were under 1 mm in thickness while the polycrystalline samples were less than 0.5 mm in thickness. These samples were prepared by first mechanically polishing them with a Grinder-Polisher on SiC papers from 400 grit down to 4000 grit with a rotation speed of 200 rpm, and then electropolishing in a 5% perchloric acid in methanol solutions using a Struers TENUPOL-5 twin-jet electropolisher. The polishing times were around 15 seconds.

A static beam was used to avoid the pulse beam effect [23]. The beam spot was about 5 mm in diameter after defocusing. Three beam deflectors were used along the beamline to filter out the carbon contaminant [24-26]. The vacuum was about 6×10^{-8} torr or better in the target chamber during irradiation. A liquid nitrogen trap was used in the chamber to improve the vacuum. The temperature was monitored by multiple thermocouples mounted on the hot stage. The overall temperature fluctuation during the irradiation was less than ± 5°C. The Stopping and Range of Ions in Matter (SRIM) code

was used to simulate radiation damage [27]. The Kinchin-Pease mode was used [28]. There has been a debate over the accuracy of full damage cascades vs. Kinchin-Pease options [29]. The selection of the Kinchin Pease option was based on consistency with a series of previous studies. The Fe displacement energy was 40 eV [30].

The focused ion beam (FIB) technique was used to prepare the TEM lamellas by using a Tescan Lyra-3. At first, a 30 keV Ga ion beam was used to lift out and thin the TEM lamella to less than 200 nm in thickness. Then the Ga ion beam was decreased to 5 keV to do the final thinning of the lamella to less than 100 nm. The Electron energy loss spectroscopy (EELS) technique was used to measure the lamella thickness at different locations. Transmission electron microscopy (TEM) was used to characterize microstructures using an FEI Tecnai G2 F20 ST. The operation voltage was 200 kV. The area, size, and position of each void were characterized by using ImageJ, an open-source image analysis tool [31].

3.3. Results

3.3.1. The effect of incident ion energy, dpa rate, and temperature on the void zone denuded width

Figure 3.1 compares TEM micrographs of the near-surface regions of single-crystal Fe irradiated to 50 and 100 peak dpa at 475°C by 1 MeV, 2.5 MeV, 3.5 MeV, and 5 MeV ions. There are void denuded zones observed in all images. First, the widths of the void denuded zones increase with increasing ion energies. For the 50 dpa irradiations, widths are 71 nm for 1 MeV (figure3.1 a-1), 80 nm for 2.5 MeV (figure 3.1

b-1), 98 nm for 3.5 MeV (figure 3.1 c-1) and 109 nm (figure 3.1 d-1). Second, for each energy, the widths of void denuded zones decrease with increasing dpa. For 1 MeV, the widths reduce from 71 nm (50 dpa) to 61 nm (100 dpa, figure 3.1 a-2). For 2.5 MeV, the width reduces from 80 nm (50 dpa) to 73 nm (100 dpa, figure 3.1 b-2). For 3.5 MeV, the widths reduce from 98 nm (50 dpa) to 82 nm (100 dpa, figure 3.1 c-2). For 5 MeV, the widths reduce from 109 nm (50 dpa) to 90 nm (100 dpa, figure 3.1 d-2).

For voids in the near-surface region, the size increases with increasing peak dpa. The void growth can be directly visualized in Figure 3.1. Quantitative analysis show that the averaged sizes (at about a depth oft 250 nm) increase from 9.6 nm (50 peak dpa) to 17.5 nm (100 peak dpa) for 1 MeV, from 20.5 nm (50 peak dpa) to 22.0 nm (100 peak dpa) for 2.5 MeV, from 13.0 nm (50 peak dpa) to 20.3 nm (100 peak dpa) for 3.5 MeV, and from 10.4 nm (50 peak dpa) to 16.9 nm (100 peak dpa) for 5 MeV.

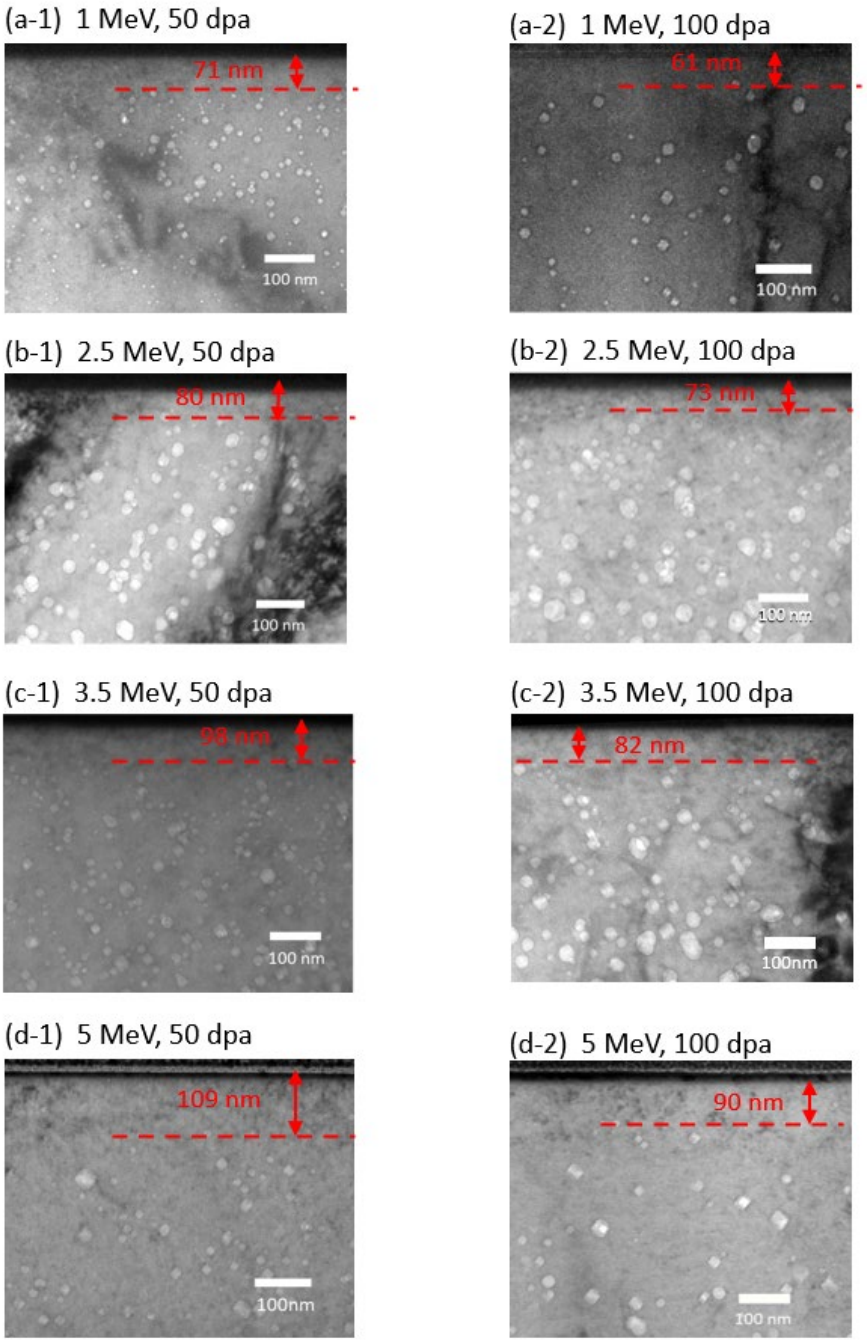

Figure 3.1: Cross-sectional TEM micrographs of single-crystal Fe irradiated at 475 °C by Fe ions of (a-1) 1 MeV at 50 peak dpa, (a-2) 1 MeV at 100 peak dpa, (b-1) 2.5 MeV at 50 peak dpa, (b-2) 2.5 MeV at 100 peak dpa, (c-1) 3.5 MeV at 50 peak dpa, (c-2) 3.5 MeV at 100 peak dpa, (d-1) 5 MeV at 50 peak dpa, and (d-2) 5 MeV at 100 peak dpa. The red dash lines refer to the boundary of the void denuded zones.

Surface sputtering cannot be ignored in determining the final thickness of void denuded zones. The sputtering is a function of local nuclear stopping power [32], which is linked to the surface dpa rate $K_{surface}$. With decreasing beam energies, the nuclear stopping power peaks shift towards the surface. Hence, lower beam energies lead to higher $K_{surface}$ and higher sputtering yields. Using the SRIM code and selecting the simulation option of "Monolayer Collision Steps/Surface Sputtering," the sputtering yields are calculated to be 2.11 atoms per bombarding ion (for 1 MeV), 1.35 (for 2.5 MeV), 1.16 (for 3.5 MeV), and 0.95 (for 5 MeV). For 50 peak dpa, the sputtering thicknesses are 12.4 nm (for 1 MeV), 8.0 nm (for 2.5 MeV), 6.8 nm (for 3.5 MeV), and 5.6 nm (for 5 MeV). For 100 peak dpa, all values are doubled based on proportionality of sputtering to total ion fluences. Figure 3.2 (a) plots the sputtering thickness for ion energies of 1 to 5 MeV, for a fixed 100 peak dpa. The sputtering loss decreases with increasing beam energy.

Opposite to the sputtering trend, the width of vacancy depleted zones increases with increasing beam energy, since the width is proportional to $(\frac{D_v}{K})^{1/4}$ [12]. Under a fixed peak dpa rate, the near surface local dpa rate decreases as the beam energy increases. It is obvious that, a locally averaged K value should be used in calculating $(\frac{D_v}{K})^{1/4}$. However, it is unclear what the appropriate depth region is for obtaining the averaged K, particularly for relatively low energy irradiations such as the 1 MeV irradiation which has a shallow dpa profile peak at about 270 nm. A shallow dpa peak means a high nonuniformity of K along the ion path. To further elucidate the effect, Figure 3.2 (b)

compares $(\frac{D_v}{K})^{1/4}$ curves using K_{avg} values obtained over different depth regions. A comparison was made by using depth regions of 0 to 200 nm, 0 to 400 nm, and 0 to 600 nm. A wider depth window will shift the curve downwards but does not change the curve slopes in any significant manner. The off-trend point for the 1 MeV energy with a depth window selection of 0 to 600 nm is due to the fact that the dpa peak is shallower than 600 nm. Since changing the depth window is almost equivalent to changing another fitting parameter and all show the same general trend in proportionality of $(\frac{D_v}{K})^{1/4}$ to the width of the void denuded zone Δx, this cannot determine the best depth window for K_{avg} calculation. For the rest of the discussion, we use the window from 0 to 200 nm.

Figure 3.2 (c) plots the experimentally measured void denuded zone widths Δx and the line of best fit. The fitting considers the sputtering loss, using the data from both figure 3.2 (a) and 3.2 (b). The fitting adjusts only one parameter, which is the proportionality of $(\frac{1}{K})^{1/4}$ to Δx. The depth region of 0 to 200 nm is used for averaging the near surface dpa rate $K_{avg.}$ The best fitting gives $\Delta x\ (nm) = 17.24\ (\frac{1}{K})^{1/4}$. Note the fitting is for 475 °C. The temperature dependent fitting will be further discussed.

Figures 3.1 and 3.2 are for experiments using a fixed peak dpa rate but different Fe ion energies. In a parallel study, we irradiated polycrystalline Fe using a beam energy of 5 MeV, but at different peak dpa rates. Figures 3.3 (a) and (b) compare the cross-sectional TEM images of polycrystalline Fe irradiated at peak dpa rates of 2.0×10^{-4} and 6.0×10^{-3} dpa/s, respectively. Both irradiations were performed at 475 °C to a peak dose

of 50 dpa. The void denuded zone widths are 177 nm for 2.0×10^{-4} and 59 nm for 6.0×10^{-3} dpa/s.

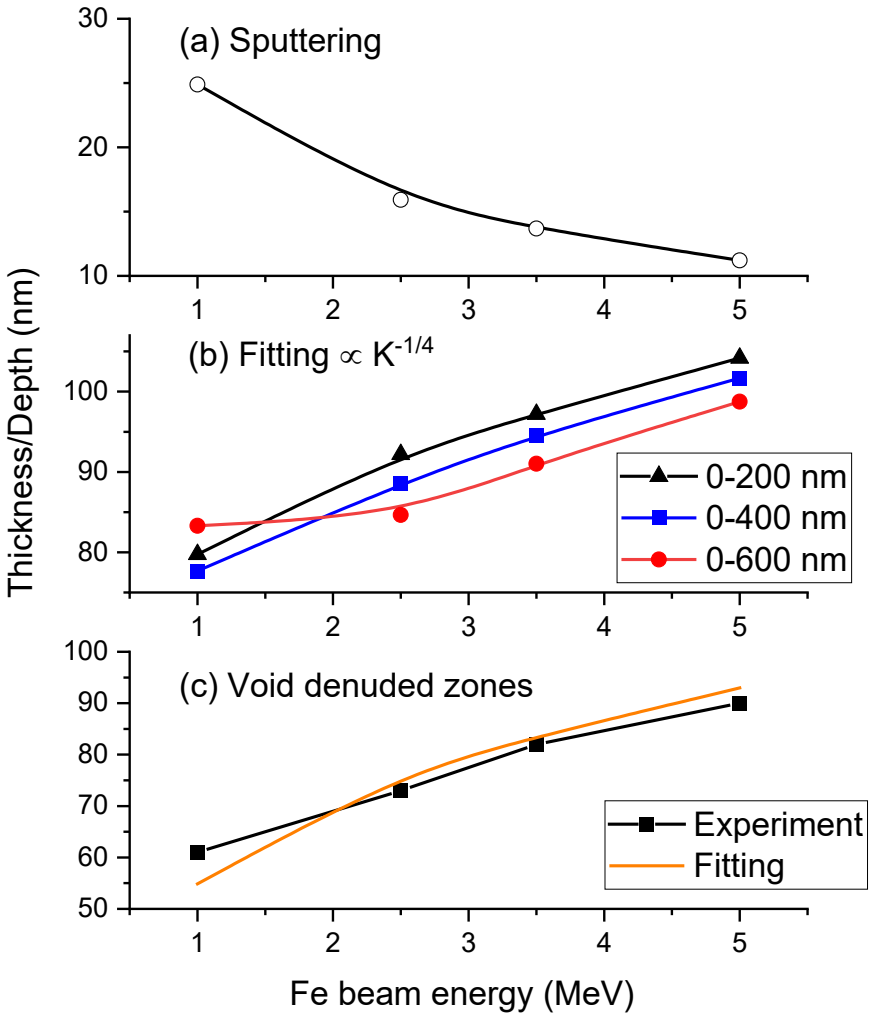

Figure 3.2: (a) SRIM calculated sputtering loss, (b) the void denuded zone width obtained through fitting by assuming Δx is proportional to $(1/K)^{1/4}$, where K is obtained through averaging over different depth regions, and (c) a comparison of experimental data and the best fitting. The fitting in (c) considers the sputtering loss.

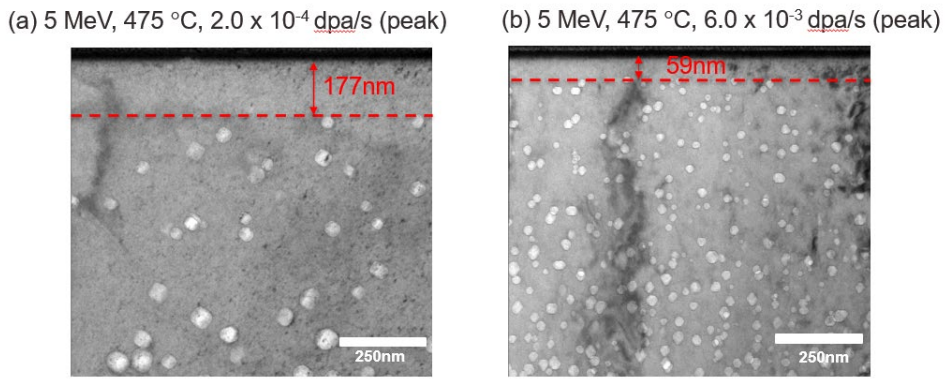

Figure 3.3: Cross-sectional TEM images of polycrystalline Fe irradiated at the peak dpa rate of (a) 2.0×10^{-4} and (b) 6.0×10^{-3} dpa/s, respectively. Both were irradiated at 475°C to a peak dose of 50 dpa.

To study the temperature dependence of Δx, irradiations at various temperatures were also performed. Figures 3.4 (a)–(c) compare the cross-sectional TEM images of samples irradiated at 425 °C, 475 °C, and 525 °C, respectively, under the same peak dpa rates of 6×10^{-3} dpa/s to 50 dpa. The Δx increases from 36 nm at 425 °C, to 59 nm at 475 °C, and to 92 nm at 525 °C.

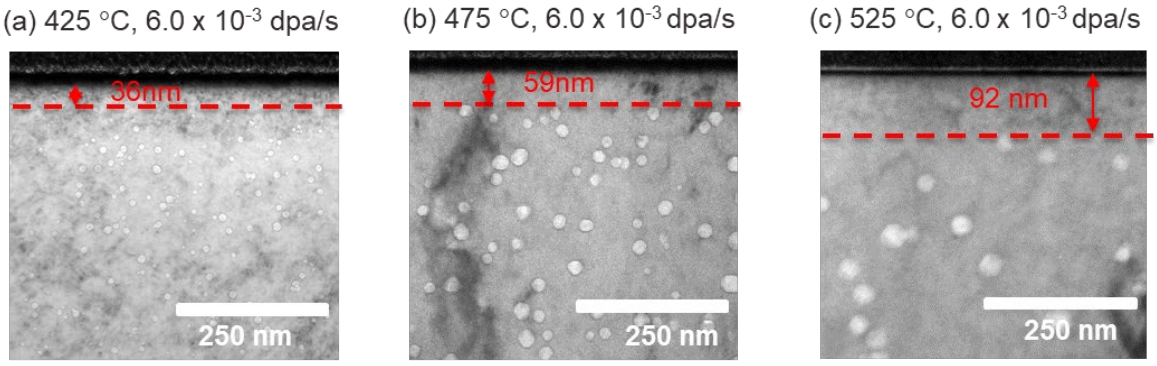

Figure 3.4: Cross-sectional TEM images of polycrystalline Fe irradiated by 5 MeV Fe ions at (a) 425 °C, (b) 475 °C, and (c) 525 °C. The peak dpa rates for all irradiations are 6.0×10^{-3} dpa/s with a peak dose of 50 dpa.

To obtain a general expression of Δx, Figure 3.5 summarizes all experimental data obtained under various energies (1, 2.5, 3.5, 5 MeV), various peak dpa rates (2.0×10^{-4}, 1.2×10^{-3}, 6.0×10^{-3} dpa/s), and various temperatures 425°C, 475°C, and 525°C. Note that all data points have sputtering loss added to the experimental Δx values. The sputtering yields are assumed to be dpa rate independent since the ion flux is not high enough to have simultaneous arrival of two ions at the same spot. The best fitting obtains the following:

$$\Delta x\ (nm) = 1.037 \times 10^4 \left(\frac{\exp\left(-1.65eV/kT\right)}{K}\right)^{1/4} \qquad \text{(Eq. 3.1)}$$

where k is the Boltzmann constant and T is temperature. The obtained activation energy is significantly higher than the theoretical vacancy migration energy, which will be further discussed.

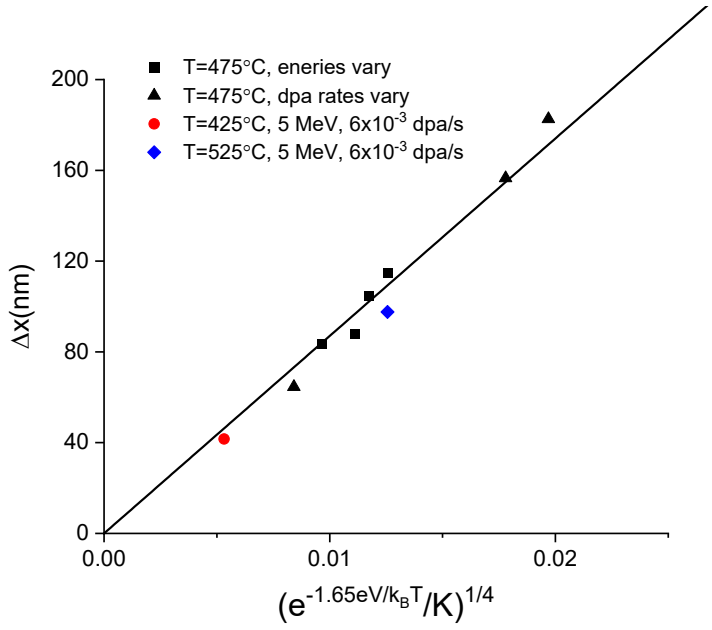

Figure 3.5: The width of void denuded zone Δx as a function of $(e^{-1.65eV/kT}/K)^{1/4}$ The activation energy of 1.65eV is obtained from the line of best fit.

3.3.2. MOOSE simulations

The analytical solutions of one-dimensional defect distribution in the near-surface region of a bulk containing defect trapping sites were given in previous studies [12]. The solutions consider various conditions, from the defect trapping dominated case to the defect recombination dominated case. The change from one extreme case to the other does not change the profile shape in a significant way [12]. The normalized point defect profile is approximated by $\alpha(1 - \exp(-\beta x))$, where x is a function of depth, β is a function of dpa rate and vacancy mobility and α is a fitting parameter. The analytical solution is a special case having a constant dpa rate, and does not consider the effects from the dpa profile or the injected interstitials in an ion irradiation. In an effort to improve accuracy, we modeled the defect interactions and defect-surface interactions using rate theory implemented in MOOSE, the Multi-Physics Object-Oriented Simulation Environment [33]. The defect reaction equations, including defect annihilation, trapping, and diffusion, are given by: [34].

$$\frac{\partial C_v}{\partial t} = f_{survive} K_0 - K_{\perp,v} \rho_\perp C_v - K_{iv} C_v C_i + \nabla D_v \nabla C_v \qquad \text{(Eq. 3.2)}$$

$$\frac{\partial C_i}{\partial t} = [f_{survive}(1 - f_{i-cluster}) K_0 + K_{II}] - K_{\perp,i} \rho_\perp C_i - K_{iv} C_i C_v + \nabla D_i \nabla C_i \qquad \text{(Eq. 3.3)}$$

C_v and C_i are concentrations of vacancies and interstitials, $f_{survive}$ is the survival fraction of defects after the damage cascade creation, and $f_{i-cluster}$ is the fraction of interstitials which immediately form small defect clusters, allowing one-dimensional diffusion and a rapid removal preventing loss to other mechanisms such as defect recombination and absorption by defect sinks [35]. K_0 is the defect creation rate, $K_{||}$ is

the Fe introduction rates as the injected interstitial source, $K_{\perp}$ is the dislocation sink strength, K_{iv} is the point defect recombination rate, and D_v and D_i are diffusivities of vacancies and interstitials respectively. For the defect creation rate K_0 as a function of depth, SRIM calculated dpa profiles were used as inputs. The major parameters used in the simulation are listed in Table 3.1.

The same approach has been previously used to understand injected interstitial effects and details of void profiles in self-ion-irradiated Fe [34]. The modeling has no intention to predict void growth or full-scale defect clustering involving not only void growth but also dislocation evolution. Rather, the modeling is used to provide some insights into the surface effect, using a simplified approach. The simplifications assumed are (1) dislocations, as the major biased defect sink for interstitials, are fixed without time evolution, and (2) voids, as neutral defect sinks for both interstitials and vacancies, are ignored.

Table 3.1: Parameters used in the present simulations

Property	Value	Unit	Source
T	From 698 to 898	K	Present experiments
$Peak\ DPA\ Rate$	From 6×10^{-3} to 2×10^{-4}	dpa/s	Present experiments
D_{0_v}	5.0×10^{17}	nm^2/s	Present experiments
E_{m_v}	1.86	eV	Present study based on [36]
D_{0_I}	2.09×10^{11}	nm^2/s	[37]
E_{m_i}	0.17	eV	[37]
$r_{\perp_v}$	1.2	nm	[38]
$r_{\perp_i}$	3.6	nm	[38]
$\rho_{\perp}$	10^{-5}	$\#/nm^2$	[39]
∂_{Fe}	0.286	nm	Present study
$f_{survive}$	25	%	[40]
$f_{i-cluster}$	30	%	[34,35]

The vacancy migration energy in Table 3.1 is selected to be 1.86 eV, instead of the 0.67 eV typically used [36]. The selection considers the effect of carbon, which is well known to reduce vacancy mobility through the formation of vacancy-carbon complexes. The complex formation immobilizes vacancies and later are dissociated with the dissociation probability determined by temperature and vacancy-carbon binding energies. Such trapping and de-trapping processes and their effects on changing vacancy effective mobilities have been modeled in previous first principle calculations [36]. Figure 3.6 plots the effective vacancy diffusivities in Fe containing various carbon background concentrations. For carbon-free Fe, the vacancy migration energy is 0.67 eV. With the presence of carbon, vacancy mobilities are reduced with the effective

migration energy increasing from 0.67 eV to 1.86 eV. The transition temperature shifts lower with increasing carbon concentration as can be seen from the points on the graph where the slope changes at smaller 1/T values. The level of carbon shifts vacancy diffusivity at temperatures lower than the transition temperature. The curve for 140 appm carbon is obtained from extrapolation, and this is the expected effective carbon diffusivities in the polycrystalline Fe used in the present study.

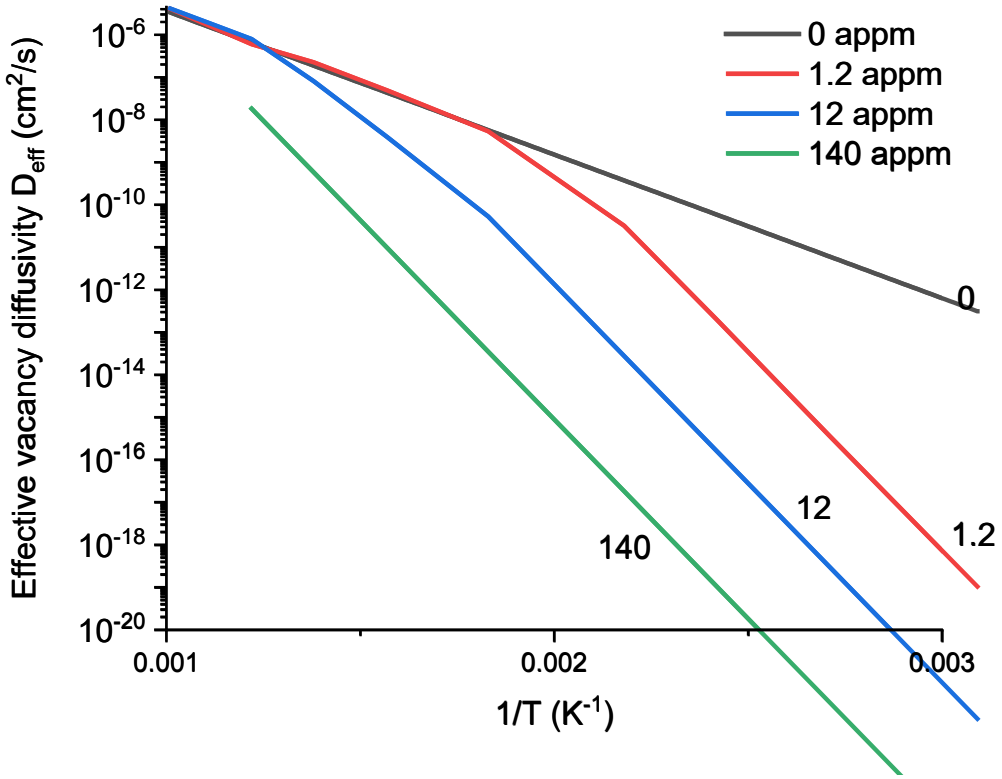

Figure 3.6: Effective vacancy diffusivity as a function of temperatures and C concentrations in Fe (α-iron).

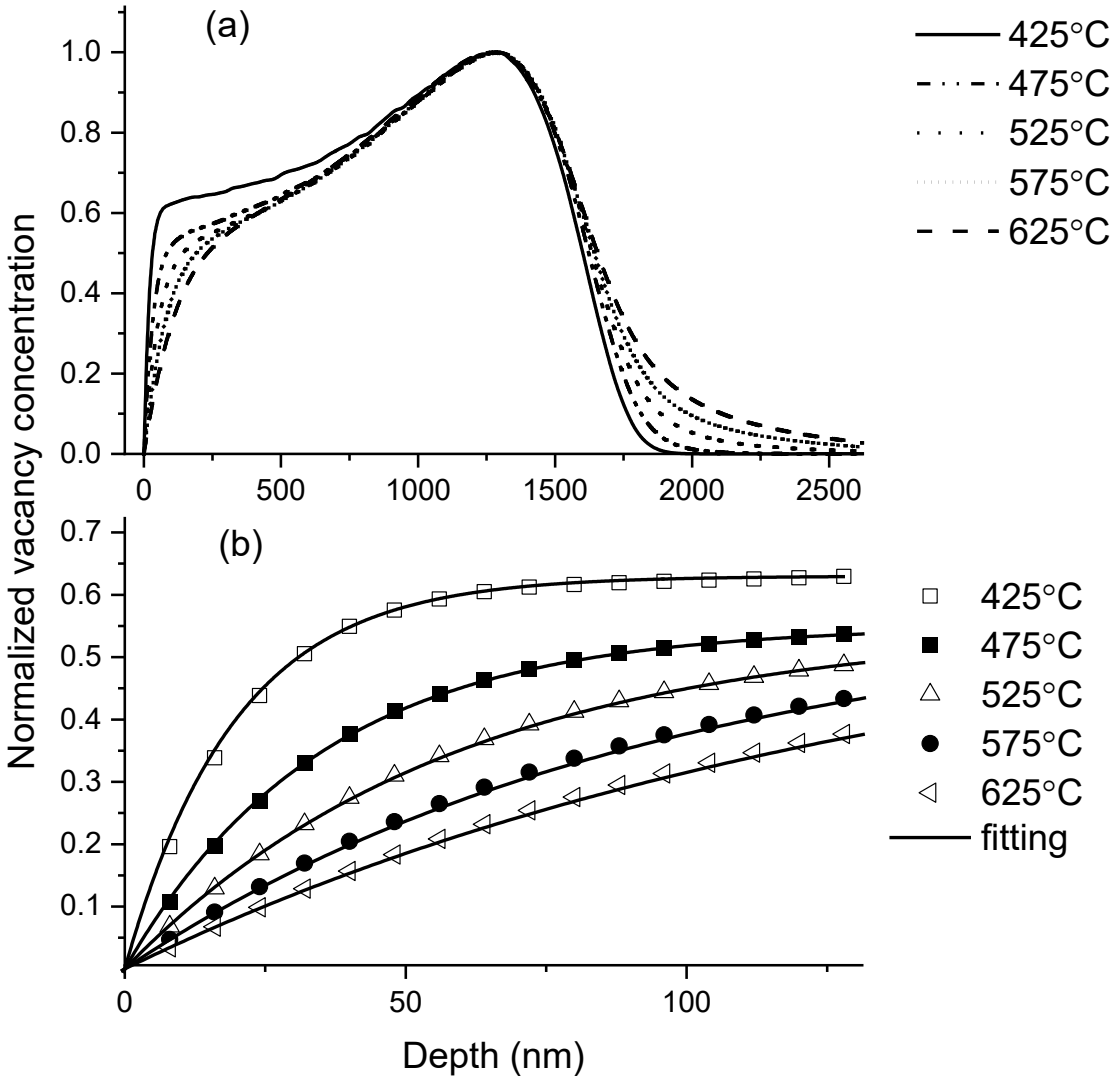

Figure 3.7: (a) Depth profiles of normalized void nucleation rates in polycrystalline Fe irradiated by 5 MeV Fe ions at the peak dpa rate of 6 x10-3 dpa/s, (b) the enlarged vacancy profiles for each temperature and the solids lines are from the best fitting.

Figure 3.7 (a) shows the normalized vacancy profiles in polycrystalline Fe irradiated by 5 MeV Fe ions at the peak dpa rate of 6×10^{-3} dpa/s. The dpa profile and implanted Fe profile from SRIM calculations are used as inputs for the simulations. The vacancy profiles are normalized by the peak height around the dpa peak location. The profile

largely follows the dpa profile. Note that the dpa peaks at 1.3 μm. At the depths beyond the dpa peak, higher temperatures lead to further spreading/diffusion. In the near surface region, a higher temperature causes increased vacancy removal from the surface, leading to a deeper/wider region of vacancy reduction near the surface. For each vacancy profile, the near surface region is fitted with $\alpha(1-\exp(-\beta x))$, where x is the depth, and α and β are both fitting parameters. Figure 3.7 (b) shows the enlarged vacancy profiles for each temperature and the solids lines are from the best fitting. The modeling obtained values, $1/\beta$, are 20 nm for 425°C, 35 nm for 475°C, and 59 nm for 525°C. According to Figure 4, the experimentally measure void denuded zone widths are 36 nm for 425°C, 59 nm for 475°C, and 92 nm for 525°C, which differ from $\frac{1}{\beta}$ by a factor ~2.

Figure 3.8 shows the Δx^4 changes as a function of temperature, with $\Delta x = 1/\beta$ obtained from fitting the modeling obtained vacancy profiles (Fig.3.7), for peak dpa rates of 2×10^{-4} dpa/s and 6×10^{-3} dpa/s. Δx^4 values follow an Arrhenius temperature dependence and the curves are parallel under different dpa rates. The extracted activation energy is 2.06 ± 0.07 eV for 2×10^{-4} dpa/s, and 2.15 ± 0.02 eV for 6×10^{-3} dpa/s, which is slightly higher than the effective vacancy migration energy of 1.86 eV as the input (Table 3.1). A small difference is expected since the rate theory simulations consider additional complexities such as the difference between interstitial and vacancy trapping by dislocation loops, and the injected interstitial effects. At a lower temperature, both interstitial and vacancy concentrations will be higher under a steady state when defect creation and removal reach a balance. However, since interstitial diffusivity is much higher than vacancy diffusivity, interstitial loss through the surface locally decreases

point defect recombination and increases near surface vacancy concentrations. This modifies the vacancy profile and slightly narrows the width of the vacancy reduction region. The effect is more obvious at low temperatures, adding a small contribution to $E_{\Delta x^4}$.

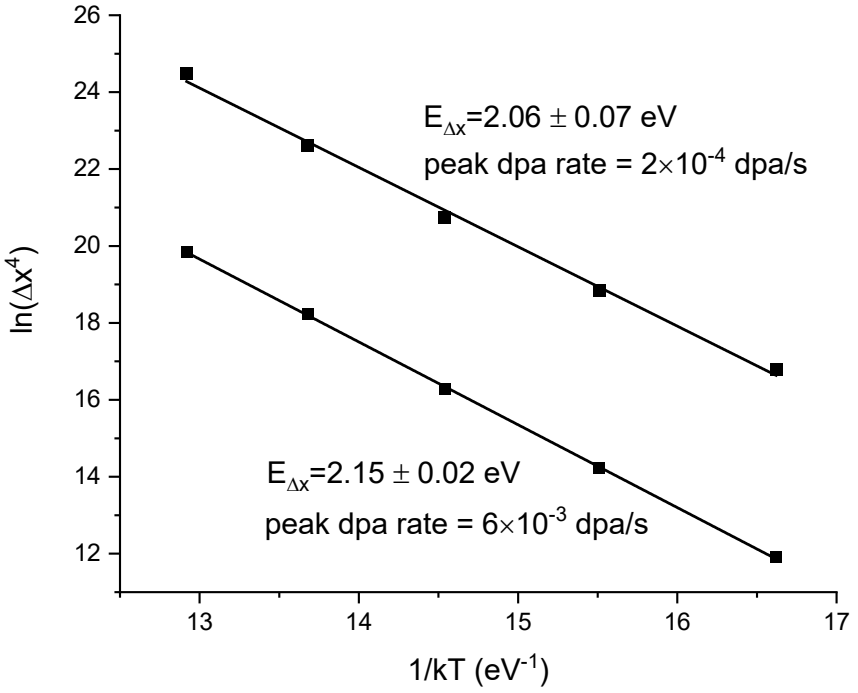

Figure 3.8: The characteristic depths of vacancy profiles as a function of temperature, for 5 MeV Fe irradiated polycrystalline Fe at a peak dpa rate of 6×10^{-3} dpa/s obtained from MOOSE simulations.

3.3.3. Surface effect beyond the void denuded zone

As mentioned in the introduction, there has been a contradictory observation on the role of the surface effect in void swelling next to the void denuded zones. Some studies reported locally enhanced swelling but others did not. In our recent study, it was reported that the appearance of a surface swelling peak is sensitive to dpa rates. Surface swelling peaks occur if the irradiation temperature is below a threshold temperature. This threshold temperature shifts lower if the dpa rate is lower. Therefore, surface swelling peaks can be avoided under the appropriate selection of irradiation parameters. Obviously, surface swelling peaks should be avoided in ion irradiation testing since it is an artifact caused by the surface. First, it does not represent the true swelling resistance of bulk materials (unless the testing is specifically for understanding near surface behaviors). Second, a reliable testing method for swelling needs to establish the correct correlation to local damage levels. At the depth beyond the surface swelling peak, the swelling drops even as the local dpa is increasing. Even when both swelling and local dpa are averaged over these combined regions (the swelling peak and the drop beyond it), the swelling data is questionable.

For the present study, we are most interested in the irradiation conditions which do not create a surface swelling peak. One question is, under optimized irradiation conditions without introducing a surface swelling peak, what is the region being disturbed by the surface effect. The answers provide boundaries to exclude swelling data from these affected regions. It is possible that voids can still nucleate and grow in the region next to the void denuded zones, but the swelling level could be reduced due to

the surface effect. This question is not trivial since many early studies used relatively shallow self-ion irradiation such as 1 MeV Ni ions for swelling testing, and surface effects may thus significantly affect the whole swelling region.

Figures 3.9 (a)–(d) plot the void swelling as a function of depth for 1 MeV, 2.5 MeV, 3.5 MeV, and 5 MeV, respectively. For each energy, there are two ion fluences: 50 peak dpa and 100 peak dpa. Sold lines are SRIM calculated dpa profiles. The projected ranges are 0.4 μm (for 1 MeV), 0.9 μm (for 2.5 MeV), 1.2 μm (for 3.5 MeV), and 1.5 μm (for 5 MeV). The dpa curves peak at 0.3 μm (for 1 MeV), 0.7 μm (for 2.5 MeV), 1.0 μm (for 3.5 MeV), and 1.3 μm (for 5 MeV). As shown in Figure 3.9, swelling increases with increasing depths and reaches the maximum at depths shallower than the depths of the peak dpa from the dpa profiles. The suppression of void swelling at the dpa peak location has been well known due to injected interstitial effects. Figure 3.9(d) shows that for 5MeV ion irradiations, the swelling of the 100 dpa (peak) irradiation is significantly higher than that of 50 dpa (peak) irradiation. Figures 3.9 (b) and (c) show the swelling increment becomes less for 2.5 MeV and 3.5 MeV irradiations respectively as the dose moves from 50 to 100 peak dpa. For the 1 MeV irradiations, as shown in Figure 3.9 (a), swelling seems saturated and both curves of 50 dpa and 100 dpa are close to each other. The swelling saturation is due to the combined effects from both the surface effect and injected interstitial effect, which affects the whole swelling depth region for 1 MeV. For 2.5 MeV and 3.5 MeV, the width of zones which are not altered by both effects are narrower than that of 5 MeV. If data analysis is limited to a “safe zone”, the three energies of 2.5 MeV, 3.5 MeV, and 5 MeV can give consistent swelling

dependence on local dpa. The determination of the safe analysis zone under each energy was reported in section 2 of this work.

Here, we propose a method to evaluate the surface effect on void swelling, by plotting swelling as a function of local dpa. The principle of the method is based on (1) reliable swelling data should show a universal and consistent dependence on local dpa, (2) the swelling-dpa relationship should be the same in one single sample at different depths (therefore, different local dpa) and in different samples with differing doses at the same depth, and (3) inconsistency occurs when the surface or the damage rate plays a role to either enhance or reduce swelling.

Figures 3.10 (a)-(d) plot swelling as a function of local dpa values for 5 MeV, 3.5 MeV, 2.5 MeV, and 1 MeV, respectively. All irradiations were performed at 475 °C with a fixed peak dpa rate of 1.2×10^{-3} dpa/s. For each beam energy, there is a parallel shifting of the front of the swelling curves between 50 peak dpa and 100 peak dpa. For each swelling curve, swelling quickly rises up with a high slope in the first stage (e.g., 0.35% per dpa in Figure 3.10 (a), and then approaches the second stage with a lower slope (e.g., 0.06% per dpa in Figure 3.10 (a)). As to be discussed, the high slope in the first stage does not represent the true swelling rate. Rather, it is an artifact due to the surface effect.

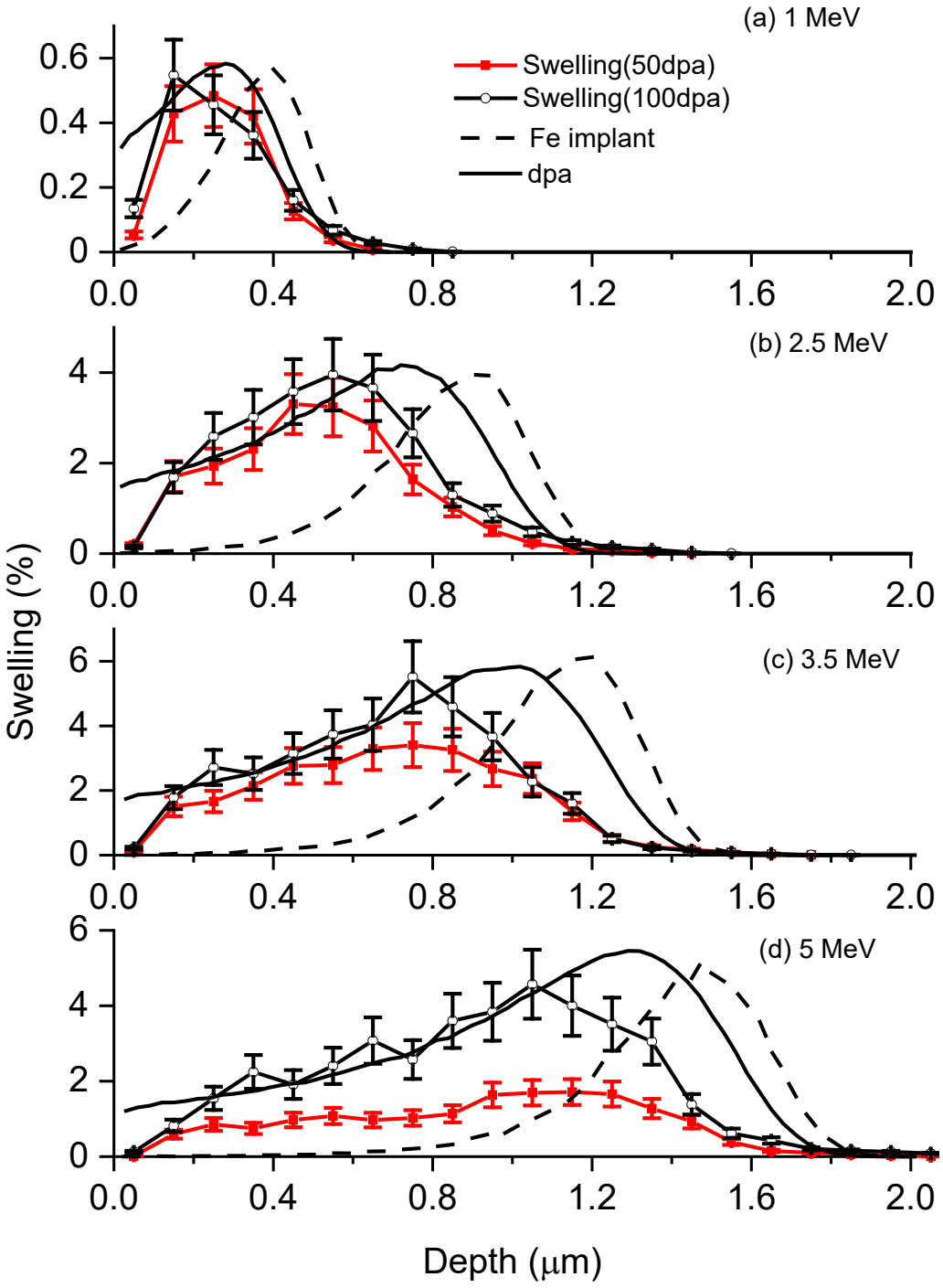

Figure 3.9: Void swelling profiles in Fe irradiated by Fe ions of (a) 1 MeV, (b) 2.5 MeV, (c) 3.5 MeV, and (d) 5 MeV, to both 50 dpa and 100 dpa at 475 °C. All irradiations were performed using the same peak dpa rate of 1.2×10^{-3} dpa/s. Sold lines and dash lines are SRIM calculated profiles of dpa and implanted Fe, respectively.

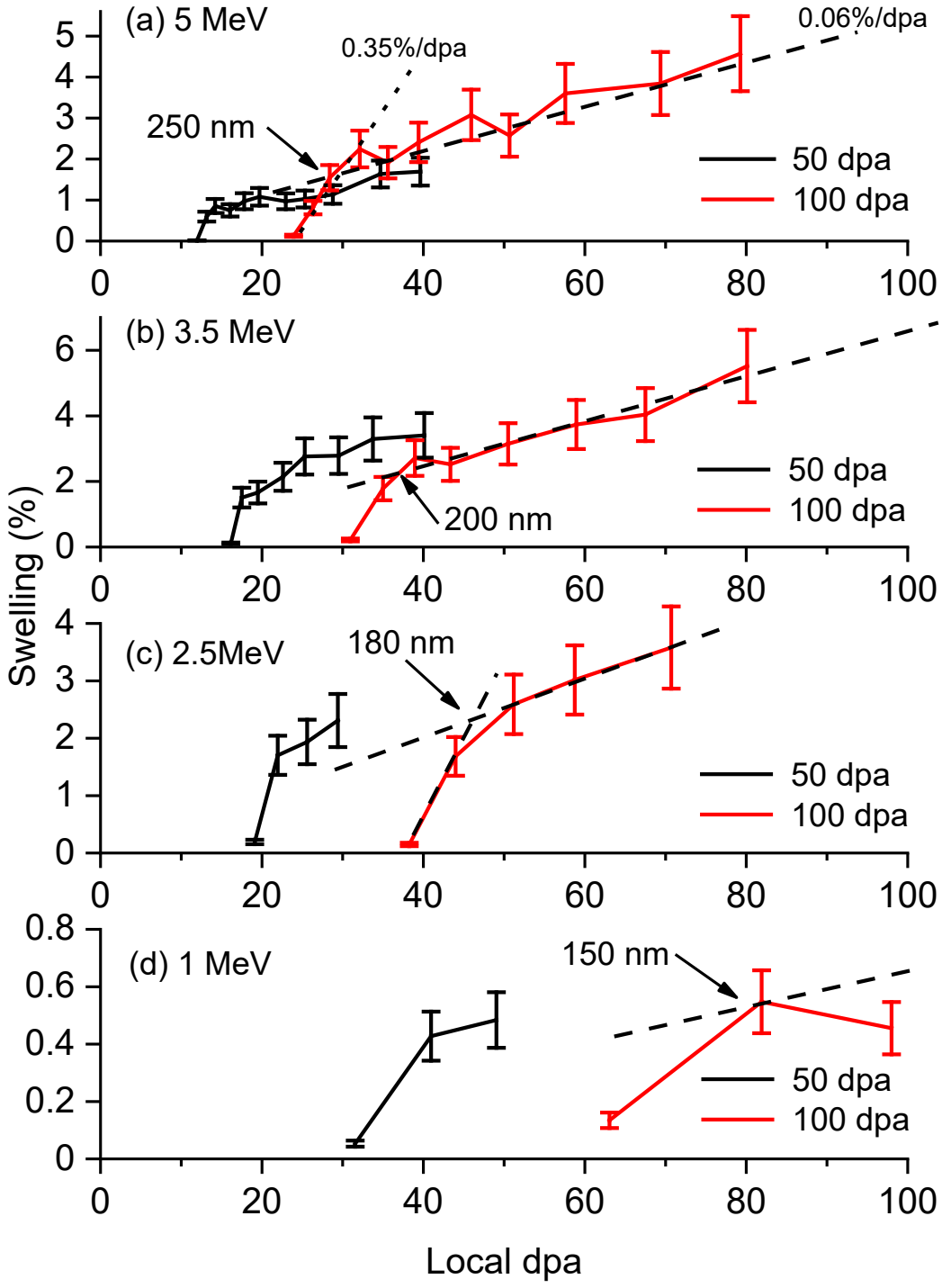

Figure 3.10: Void swelling versus local dpa values in Fe irradiated by Fe ions of (a) 5 MeV, (b) 3.5 MeV, (c) 2.5 MeV, and (d) 1 MeV. For each energy, 50 dpa and 100 dpa data are included. All irradiations were at 475 °C, and use the same peak dpa rate of 1.2×10^{-3} dpa/s.

If the swelling curve of 50 dpa represents a true dpa dependence, the curve of the 100 dpa irradiation should follow the same curve and the parallel shifting of the swelling front should not happen. The cause of such shifting is the surface effect. Figure 3.11 (a) schematically shows the expectation in the absence of a surface effect. Two lines represent two depth points. The arrow refers to the swelling growth at each depth point when local dpa increases. If each depth point follows the same swelling-dpa relationship, all data points will follow essentially the same curve thus another parallel line for each depth region. However, if the surface suppresses void swelling, the swelling-dpa dependence curves are depth sensitive. As shown in Figure 3.11 (b), under a surface effect, the shallow point may follow a low swelling per dpa rate while the second depth point will follow a slightly increased swelling per dpa rate. Due to the rate difference, the plots of swelling vs. local dpa, referred as dash lines in Figure 3.11 (b), will show horizontal, parallel shifting.

Swelling vs. local dpa curves can be used to determine the region where the surface effect diminishes or becomes ignorable. The boundary corresponds to the depth where curves transition to a new slope. As explained in Figure 3.11, the transition corresponds to the changes from the stage that each depth points follow a different swelling to dpa rate to the stage that all points follow the same swelling to dpa rates. The depths of the transition point, as shown by the arrows in Figure 10, are 250 nm (for 5 MeV), 200 nm (for 3.5 MeV), 180 nm (for 2.5 MeV), and 150 nm (1 MeV). The depths are the boundaries of the surface-affected zones. All these depth points are deeper than the width of the void denuded zones determined from Figure 3.1.

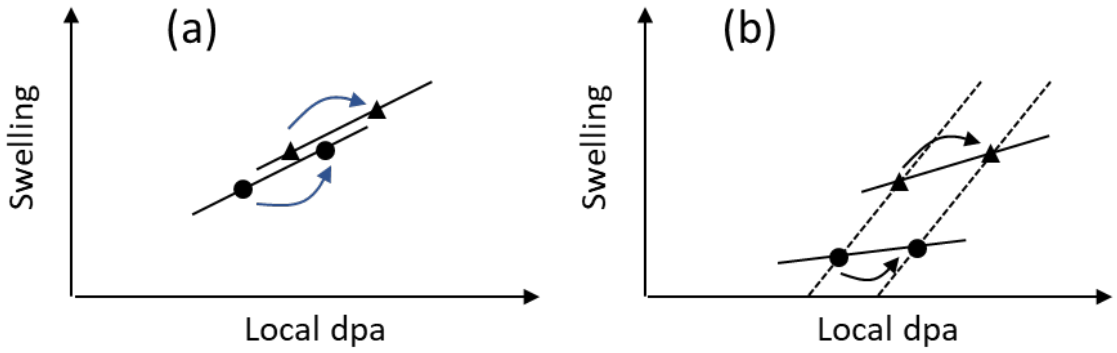

Figure 3.11: Schematics of swelling versus local dpa values for two depth locations for (a) both depth points follow the same swelling to dpa dependency and (b) shallower depth point have decreased swelling to dpa dependency in comparison to the deeper points leading to a less steep slope for the solid lines. The arrows refer to swelling changes from low to high dpa at the same depth of different samples. The dash line refers to swelling versus local dpa of the same sample but at different depths.

3.4. Discussion

Attempts were made in the present study to use void nucleation rates, instead of vacancy profiles to evaluate the surface effect. However, the void nucleation profiles show complexity and disagreement with the experimental data. Figure 3.12 (a) plots the normalized void nucleation rate profile for 5 MeV self-ion irradiated Fe at a peak dpa rate of 2×10^{-4} dpa/s. Figure 3.12 (b) contains the enlarged plots near the surface. The void nucleation rates are normalized by their values at a depth of 250 nm. Following reference [50], the vacancy supersaturation rate $S_v$is calculated by:

$$S_v = \frac{D_v C_v - D_i C_i}{D_v C_v^*} \quad \text{(Eq. 3.4)}$$

The S_v values are converted to void nucleation rates by also following reference [50].

$$\log(J_V) = 5.41547 \log(S_v) - 14.6586 \quad \text{(Eq. 3.5)}$$

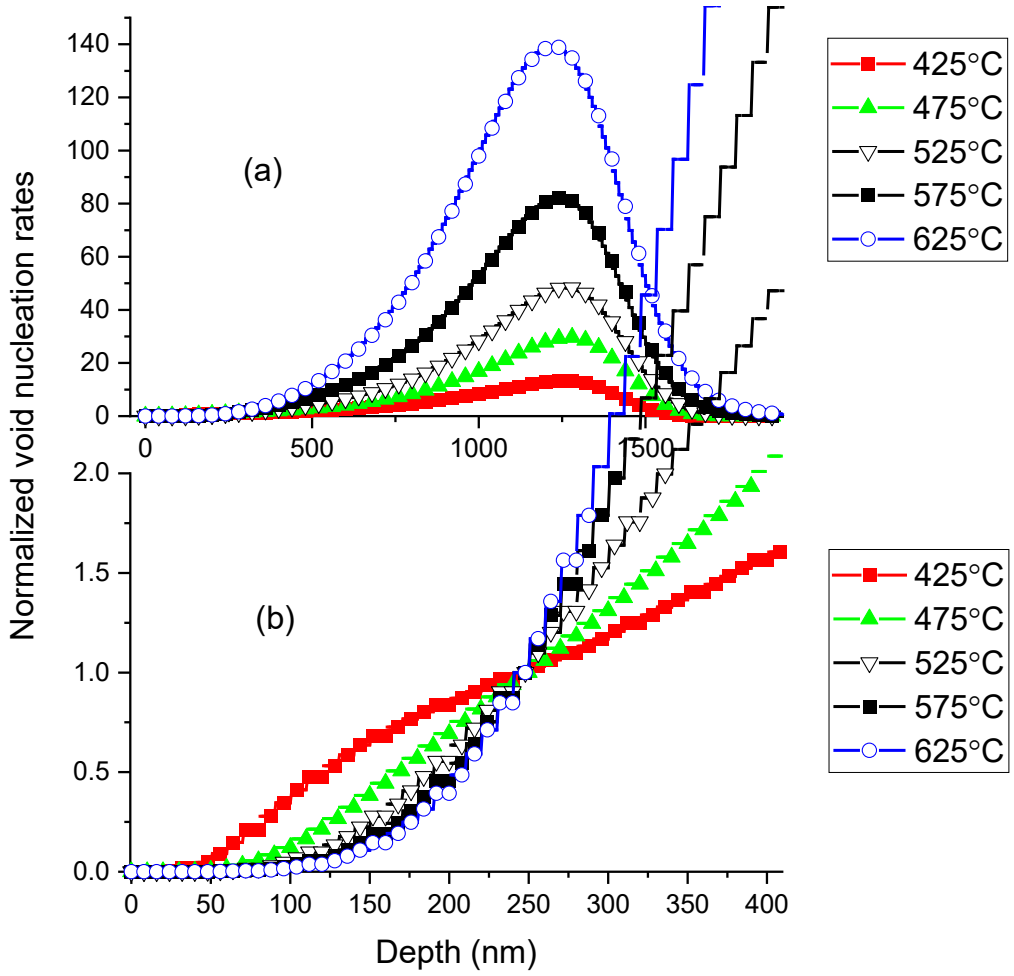

Figure 3.12: (a) Void nucleation rates in 5 MeV Fe irradiated polycrystalline Fe at a peak dpa rate of 2×10^{-4} dpa/s, and (b) enlarged plots near the surface.

Void nucleation rate profiles show a similar temperature dependence as vacancy profiles. The profile propagates closer to the surface at a lower temperature. However, there are noticeable profile shape differences. For vacancy profiles shown in figure 3.7 (b), they can be well fitted using $\alpha(1-\exp(-\beta x))$. The void nucleation rate profiles, however, cannot be fitted with a single mathematic formula. At the lowest temperature of 425°C, the curve is more like an exponential growth function, while at higher

temperatures, the curve follows logarithmic growth. One consequence is that the activation energy is more sensitive to the selection of the critical rate for determining the width. If a low rate is selected, the activation is higher. Furthermore, the curve for 425°C is very different from the rest of the curves. The width becomes significantly narrower, leading to a much higher energy around 425°C. The profile shape at low temperature (425°C) is largely due to the surface effect through fast diffusion of interstitials. Void nucleation rate profiles are more sensitive to interstitials in comparison with vacancy profiles, since the rate is not determined by the vacancy flux alone, but rather by the difference between the vacancy flux and the interstitial flux.

The temperature dependent activation energy was not observed from experiments. Only a single activation energy is observed, according to Figure 5. This suggests that the vacancy profile, instead of the void nucleation rate profile, largely determines surface void swelling. The void nucleation rates are zero-time approximations. The subsequent growth is not modeled here and needs to consider the details of vacancy-void interactions. We leave the activation energy difference extracted from vacancy profiles vs. void nucleation profiles as an open question to be further studied. The difference suggests that void growth plays a more significant role than void nucleation in determining the near surface swelling behaviors.

The observed surface-affected zones at the depth beyond the void denuded zones are important for ion irradiation testing. The finding shows that whether voids appear or not cannot be used as a criterion to judge whether the region is in a safe analysis zone for void analysis. The present study obtained the following depths as the boundary of the

surface-affected regions: 250 nm for 5 MeV, 200 nm for 3.5 MeV, 180 nm for 2.5 MeV, and 150 nm for 1 MeV. The study obtained the following depths as the width of void denuded zones: 109 nm for 5 MeV, 98 nm for 3.5 MeV, 80 nm for 2.5 MeV, and 71 nm for 1 MeV. The ratio of these two depths are 2.3 for 5 MeV, 2.0 for 3.5 MeV, 2.3 for 2.5 MeV, and 2.1 for 1 MeV. Therefore, a factor of two can be used as a good approximation. Once the void denuded zones are determined from TEM, an additional region of about equal distance needs to be excluded from the swelling analysis.

The parallel shifting of swelling-local dpa curves under different peak dpa irradiations (as shown in Figure 3.10) can be used as a method to quantitively determine the boundary of the surface-affected zone. There is another method that can be used to achieve the same goal by comparing the void density as a function of local dpa which was discussed in section two of this work. The second method does not require multiple irradiations but instead requires statistical analysis of void density as a function of depth. The method is based on the observation that, when swelling is affected by a free surface, void densities exhibit a sudden drop.

In the previous section of this work, a method of identifying safe analysis zones has been proposed [41]. The boundaries of the surface affected zone were defined by the depths where void density vs. local dpa exhibits a sudden trend change in comparison with the curve at deeper regions [41]. The boundary depths are 250 nm for 5 MeV Fe irradiation, and 150 nm for 3.5 MeV, 2 MeV, and 1 MeV Fe irradiation [41], which are consistent with results from this present method of determining the safe analysis zone.

If the surface-affected zones are not excluded, the swelling analysis may be artificially biased by an artifact of ion only irradiations. Using Figure 3.10 (a) as an example, the 50 dpa curve may appear to have 10 dpa as the incubation period, while the 100 dpa curve may appear to have 25 dpa as the incubation period. The changes of such periods among different peak dpa irradiations and different irradiation energies (in comparison with other figures in Figure 3.10) clearly show that the "observed" periods are artifacts instead.

3.5. Conclusion

A comprehensive study on the effect of free surfaces on void denuded zones and void swelling at depths just beyond the void denuded zones was performed. The testing matrix includes various beam energies (1 MeV to 5 MeV), various temperatures (425°C to 525°C), and various dpa irradiation rates (2×10^{-4} dpa/s to 6×10^{-3} dpa/s). The TEM measured void denuded zones are linearly proportional to $\left(\frac{exp\,(-\frac{E}{kT})}{K}\right)^{1/4}$. The fitting obtained an activation energy (E=1.65 eV) which is higher than theoretical vacancy migration energy. We explained the discrepancy due to carbon which reduces the effective vacancy mobilities. The extrapolation of carbon modified vacancy diffusivities from earlier studies suggests a migration energy of 1.86 eV. The curves of swelling vs. local dpa from 50 and 100 peak dpa irradiations show a parallel shifting in the low dpa (shallow depth) regions, which is explained due to the effect of the free surface. Such

shifting is proposed as a method to quantitatively determine the boundary of the surface-affected zone. The boundaries are about twice the width of the void denuded zones.

3.6. References

1. Xinghang Zhang, Khalid Hattar, Youxing Chen, Lin Shao, Jin Li, Cheng Sun, Kaiyuan Yu, Nan Li, Mitra L Taheri, Haiyan Wang, Jian Wang, Michael Nastasi, Radiation damage in nanostructured materials, Progress in Materials Science 96, 217-321 (2018).

2. Tianyao Wang, Hyosim Kim, Frank A Garner, Kenneth L Peddicord, Lin Shao, The Effect of Internal Free Surfaces on Void Swelling of Irradiated Pure Iron Containing Subsurface Trenches, Crystals 9, 252 (2019).

3. W.Z. Han, M.J.Demkowicz, E.G.Fu, Y.Q.Wang, A.Misra, Effect of grain boundary character on sink efficiency, Acta Materialia 60, 6341-6351 (2012).

4. C Sun, S Zheng, CC Wei, Y Wu, L Shao, Y Yang, KT Hartwig, SA Maloy, SJ Zinkle, TR Allen, H Wang, X Zhang, Superior radiation-resistant nanoengineered austenitic 304L stainless steel for applications in extreme radiation environments, Sci. Rep. 5, 1-7 (2015).

5. Di Chen, Jing Wang, Tianyi Chen, Lin Shao, Defect annihilation at grain boundaries in alpha-Fe, Sci. Rep. 3, 1450 (2013).

6. F. A. Garner and L. E. Thomas, "Production of Voids in Stainless Steel by High Voltage Electrons," Effects of Radiation on Substructure and Mechanical Properties of Metals and Alloys, ASTM STP 529, American Society for Testing and Materials, 1973, pp. 303-325.

7. Yoshihiro Sekio, Shinichiro Yamashita, Norihito Sakaguchi, Heishichiro Takahashi, " Void denuded zone formation for Fe–15Cr–15Ni steel and PNC316 stainless steel under neutron and electron irradiations, J. Nucl. Mater. 458 (2015)355-360.

8. Garner, F. A.. Laidler, J. J., Mastel, B.. and Thomas, L. E., "Influence of High Voltage Electron Microscope Irradiation on Neutron-Produced Microstructures in Stainless Steel," Properties of Reactor Structural Alloys After Neutron or Particle Irradiation, AST

9. Konobeev, Y. V., Pechenkin, V. A., and Garner, F. A., "On the Role of Internal Stresses in Void Denuded Zone Formation Under HVEM-lrradiation of Metals and Alloys Preconditioned by Reactor Exposure," Effects of Radiation on Materials: 19th International Symposium, ASTM STP 1366, M. L. Hamilton, A. S. Kumar, S. T. Rosinski, and M. L. Grossbeck, Eds., American Society for Testing and Materials, West Conshohocken, PA, 2000.

10. A. Hishinuma, Y. Katano, K. Shiraishi, Surface effect on void swelling behavior of stainless steel, J. Nucl. Sci. Tech. 14, 664-672 (1977).

11. R.L. Sindelar, G.L. Kulcinski, R.A. Dodd, Depth dependent microstructure in ion-irradiated 316 type steels, Journal of Nuclear Materials 122&123, 246-251 (1984).

12. NQ. Lam, S.J. Rothman, R. Sizmann, Steady-state point-defect diffusion profiles in solids during irradiation, Radiat. Eff. 1974, 23, 53–59 (1974).

13. Y. Sekio, I. Yamagata, N. Akasaka, N. Sakaguchi, Evaluation of irradiation-induced point defect migration energy during neutron irradiation in modified 316 stainless steel, Proceedings of International Conference on Fast Reactors and Related Fuel Cycles; Next Generation Nuclear Systems for Sustainable Development (FR-17)

14. Y-R Lin, A. Bhattacharya, D. Chen, J-J Kai, J. Henry, S.J. Zinkle, Temperature-dependent cavity swelling in dual-ion irradiated Fe and Fe-Cr ferritic alloys, Acta Materialia 207, 116660 (2021)

15. D. Costa, G. Adjanor, C.S. Becquart, P. Olsson, C. Domain, Vacancy migration energy dependence on local chemical environment in Fe–Cr alloys: a density functional theory study, J. Nucl. Mater., 452, 425-433 (2014).

16. B.N. Singh, S.J. Zinkle, Influence of irradiation parameters on damage accumulation in metals and alloys, J. Nucl. Mat. 217, 161-171 (1994).

17. R.B. Adamson, W.L. Bell, P.C. Kelly, Neutron irradiation effects on copper at 327°C, J. Nucl. Mater. 92, 149-154 (1980).

18. S.J. Zinkle, K. Farrell, Void swelling and defect cluster formation in reactor-irradiated copper, J. Nucl. Mat. 168, 262-267 (1989).

19. A. Bhattacharya, E. Meslin, J. Henry, B. Décamps, A. Barbu, Dramatic reduction of void swelling by helium in ion-irradiated high purity a-iron, Mater. Res. Lett. 6, 372–377 (2018).

20. Y-R Lin, A. Bhattacharya, D. Chen, J-J Kai, J. Henry, S.J. Zinkle, Temperature-dependent cavity swelling in dual-ion irradiated Fe and Fe-Cr ferritic alloys, Acta Materialia 207, 116660 (2021).

21. H. Trinkaus, B.N. Singh, A.J.E. Foreman, Impact of glissile interstitial loop production in cascades on defect accumulation in the transient, J. Nucl. Mat. 206, 200-211 (1993).

22. Aaron French, Zhihan Hu, Yongchang Li, Frank A. Garner, Lin Shao, Identification of experimental parameters that determine the depth dependence of void swelling of

pure iron under 5 MeV self-ion irradiation, focusing on avoidance of a sub-surface artifact, unpublished.

23. J.G. Gigax, Eda Aydogan, Tianyi Chen, Di Chen, Lin Shao, Y. Wu, W. Y. lo, Y. Yang, F. A. Garner, The influence of ion beam rastering on the swelling of self-ion irradiated pure iron at 450 °C, Journal of Nuclear Materials 465, 343-348 (2015).

24. L. Shao, Jonathan Gigax, Di Chen, Hyosim Kim, Frank A. Garner, Jing Wang, Mychailo B. Toloczko, Standardization of accelerator irradiation procedures for simulation of neutron induced damage in reactor structural materials, Journal of Nuclear Materials 409, 251-254 (2017).

25. J G Gigax, H Kim, E Aydogan, FA Garner, S Maloy, L Shao, Beam-contamination-induced compositional alteration and its neutron-atypical consequences in ion simulation of neutron-induced void swelling, Materials Research Letters 5, 478-485 (2017).

26. Jonathan G Gigax, Hyosim Kim, Eda Aydogan, Lloyd M Price, Xuemei Wang, Stuart Andrew Maloy, Frank A Garner, Lin Shao, Impact of composition modification induced by ion beam Coulomb-drag effects on the nanoindentation hardness of HT9, Nucl. Instruments Phys. Res. B 444, 68-73 (2019).

27. J.F. Ziegler, M.D. Ziegler, J.P. Biersack, SRIM–The stopping and range of ions in matter (2010), Nucl. Instruments Phys. Res. B 268, 1818-1823 (2010).

28. Roger Stoller, Mychailo B. Toloczko, Gary S. Was, A.G. Certain, S. Dwaraknath, Frank A. Garner, On the use of SRIM for computing radiation damage exposure, Nucl. Instrum. Methods Phys. Res. B 310, 75-80 (2013).

29. S. Agarwal, Y. Lin, C. Li, R.E. Stoller, S.J. Zinkle, On the use of SRIM for calculating vacancy production: Quick calculation and full-cascade options, Nucl. Instrum. Methods Phys. Res. B 503, 11-29 (2021).

30. A.Yu. Konobeyev, U. Fischer, Y.A. Korovin, S.P. Simakov, Evaluation of effective threshold displacement energies and other data required for the calculation of advanced atomic displacement cross-sections, Nuclear Energy and Technology 3, 169–175 (2017).

31. Schneider, C.A., Rasband, W.S., Eliceiri, K.W. "NIH Image to ImageJ: 25 years of image analysis". Nature Methods 9, 671-675, 2012.

32. Peter Sigmund, Theory of sputtering. I. Sputtering yield of amorphous and polycrystalline targets, Phys. Res. B. 184, 383-416 (1969).

33. D. Gaston, Nucl. Eng. Des. 239, 1768-1778 (2009).

34. M.R. Short, D.R. Gaston, M. Jin, L. Shao, F.A. Garner, Modeling injected interstitial effects on void swelling in self-ion-irradiation experiments, J. Nucl. Mat. 471, 200-207 (2016).

35. S.I. Golubov, A.V. Barashev, R.E. Stoller, Comprehensive Nuclear Materials, Chapter 1.13-Radiation Damage Theory, Elsevier, 2012, pp. 358-389.

36. Chu-Chun Fu, E. Meslin, Alain Barbu, Francois Willaime, Vincent Oison, Effect of C on Vacancy Migration in α-Iron. Solid State Phenomena 139, 157-164 (2008).

37. N. Soneda, T. Diaz de La Rubia, Migration kinetics of the self-interstitial atom and its clusters in bcc Fe, Philosophical Magazine A 81, 331-343 (2001), DOI: 10.1080/01418610108214307

38. V. Shastry, T. Diaz de la Rubia. The interaction between point defects and edge dislocation in BCC Iron, ASME. J. Eng. Mater. Technol.121, 126-128 (1999).

39. H. Bhadeshia, R. Honeycombe, Steels: microstructure and properties, Butterworth-Heinemann, 2011, p. 23.

40. L. Malerba, Molecular dynamics simulation of displacement cascades in -fe: a critical review, J. Nucl. Mater. 351, 28-38 (2006).

41. Yongchang Li, Aaron French, Zhihan Hu, Adam Gabriel, Laura R. Hawkins, Frank A. Garner, Lin Shao, A quantitative method to determine the region not influenced by injected interstitial and surface effects during void swelling in ion-irradiated metals, J. Nucl. Mat., submitted.

4. IDENTIFICATION OF EXPERIMENTAL PARAMETERS THAT DETERMINE THE DEPTH DEPENDENCE OF VOID SWELLING OF PURE IRON UNDER 5 MEV SELF-ION IRRADIATION, FOCUSING ON AVOIDANCE OF A SUB-SURFACE ARTIFACT

4.1. Introduction

As has previously been discussed the two most important of the neutron-atypical effects are the injected interstitial effect and the influence of the ion-incident surface in trying to design and analyze ion irradiations to better understand alloy behavior in neutron reactor environments.. The influence of the former is most important over the deepest half of the ion range [1-8] and the influence of the latter over the near-surface region [1-14]. In void swelling studies the surface effect is manifested as a void-denuded zone although the influence of the void surface on point defect distributions extends to a depth approximately twice the denuded width. The surface influence increases with increasing temperature but decreases with increasing displacement rate. The effect of the injected interstitial is opposite, decreasing with increasing temperature, however, but increasing with increasing displacement rate. More importantly, the injected interstitial distribution decreases when approaching the surface. Both the separate and combined influence of these two effects is therefore a complex function of dpa rate, temperature and depth from the ion-incident surface. Additionally, the ion identity and especially its energy determine the ion range and therefore the impact of the injected interstitial. While swelling data at all depths are of scientific value, it is desirable to extract data from the region that has the least combined influence of the two

atypical variables, especially if the data are to be used to predict neutron-induced behavior. Thus, there is an emphasis on defining the "safe analysis" zone along the ion-traversed path as a function of ion energy, temperature and displacement rate. In general, the safe zone width increases with increasing ion energy but also is thought to be dependent on temperature and displacement rate. At relatively low ion energies the two atypical effects overlap and there is no safe zone, especially since a third atypical variable, sputtering, becomes of increasing importance with decreasing energy.

There are various proposed methods to estimate the limits of a "safe analysis zone" which primarily focus on the effect of the implanted ions (injected interstitials). In one approach, diffusional-like spreading of the injected interstitial effect is proposed primarily with modeling [11]. In the approach discussed in section one of this work, however, it is argued that there is no spreading effect at higher temperature or higher dpa, and the back-boundary of significant injected interstitial effects starts at about half the projected range of implants as a good approximation [12]. This approach is based on experimental data over 1 to 5 MeV ion energy, a range of temperature and range of dpa rates [12]. One conclusion of this study is that there is no safe zone for ion energies ≤ 1.0 MeV and some useful safe zone ≥2.5 MeV. Additionally, modeling has been used in an earlier study to understand the depth distribution of void swelling in pure iron and, in particular, how the swelling distribution might not follow the shape anticipated by the displacement damage curve [3].

It is important, however, to note that sputtering, surface effects and injected interstitial effects are physical in nature and not chemical. If more than one element

comprises the metal, then microchemical differences can arise via radiation-induced segregation and precipitation, both of which are also sensitive to temperature and displacement rate but probably not with the same rate constants of the physical processes. Additionally, if the irradiating ion is not a self-ion there will be additional chemical effects that vary with depth. Therefore, our studies have concentrated on relatively pure iron irradiated with iron ions at energies of 3.5 and more recently on 5.0 MeV. Earlier studies have focused on the effects of beam rastering [15], contamination [16], ion energy [12], internal free surfaces [13], single vs. multi-crystal [12], dpa rate and temperature [12,16].

One chemical exception in these studies is difficult to avoid and must be recognized, however. When irradiations proceed to high displacement doses there is a slow progressive drift and accumulation of vacuum contaminants, primarily C, N, O, moving by Coulomb drag to the specimen surface, with carbon identified as the most easily diffusing into the specimen and having the largest impact on void swelling [16,17]. Carbon is also a minor contaminant in most commercially available "pure" iron material. Therefore, both our modeling and experimental efforts now include carbon as an active participant, measuring the starting C level and minimizing the beam-induced contamination.

The particular focus of this paper is the departure of the depth distribution of swelling from that anticipated by the shape of the dpa profile. Earlier, we focused on modeling the development of a double-peak or M-shaped distribution sometime occurring at peak swelling temperatures, showing that dpa rate, temperature and carbon

level accounted for this distribution [3]. This modeling work also predicted that swelling under some combination of these variables might "push" the swelling toward the ion-incident surface, even at a high-enough ion energy, precluding formation of any safe zone. Such sub-surface peaks in swelling were located next to a smaller denuded-zone and usually resulted in a significant reduction in local swelling, arising primarily at combinations of temperature and dose rate that magnified the impact of the injected interstitial. The current study focuses especially on such sub-surface peaks in swelling.

In Ni ion irradiations of Fe and Fe-Ni alloys by Lin et al, surface swelling peaks were observed [11]. In contrast, in Fe ion irradiations of pure Fe by Li et al., there is no observation of a surface swelling peak [12]. It appears that minor differences in carbon, displacement rate and temperature can produce sub-surface peaks or preclude their development. Such sub-surface peaks have often been seen in neutron irradiations when similar locally enhanced swelling was also observed in both pure metal and alloys in regions where a grain boundary was present [18,19]. In multicomponent alloys microchemical segregation at grain boundaries may have contributed to formation of such peaks. Early studies have proposed that the cause was one-dimensional quick diffusion of interstitial loops and their removal at a boundary [20], but surface swelling was also predicted under certain irradiation conditions in early rate theory without needing to introduce this additional interstitial diffusion mechanism [1]. At a depth beyond the surface swelling peak, local swelling decreases with increasing local dpa, which is the opposite of the expected dpa dependence of local swelling.

The motivation of the present study is to understand the physical mechanisms producing a sub-surface swelling peak using pure iron with some influence of carbon, employing both ion irradiation and modeling.

4.2. Experimental Procedure

Annealed polycrystalline iron foils of 99.8% purity were purchased from Goodfellow (Pittsburgh, Pennsylvania), with specification of <200 appm C, <800 appm Mn, <200 appm P, and <150 appm S. Due to the previously identified importance of carbon on void nucleation in earlier studies secondary ion mass spectrometry (SIMS) analysis was conducted and determined a concentration of ~140 appm C. The as-received thickness of the foils was 0.5mm and these were cut into pieces approximately 5mm×5mm, followed by mechanical polishing using a Grinder-Polisher to a 4000 grit. The specimens were then electropolished to remove mechanical-polishing-induced surface deformation using a Struers Tenupol-5 twin-jet electro-polisher with a 5% perchloric acid in methanol solution.

The specimens were irradiated in two groups. The major group was irradiated with 5 MeV Fe^{2+} ions to three damage levels: 50, 100, and 150 peak dpa at a peak dpa rate of 6×10^{-3}dpa/s. A two-step irradiation procedure was conducted at temperatures of 425°C, 475°C, and 525°C, a range selected since the maximum swelling temperature of Fe observed in our earlier studies is ~475°C. Two irradiation campaigns were employed at each temperature and peak dpa rate, irradiating two foils to 100 dpa, removing one foil and replacing it with an unirradiated foil, followed by irradiating to 50 dpa to produce 50

and 150 peak dpa levels. Based on the results of the 425°C specimens yielding unanticipated anomalous subsurface swelling behavior, two additional irradiations were conducted to 50 dpa at 425°C at peak rates of 1×10^{-3}dpa/s and 2×10^{-4} dpa/s to explore the effect of dpa rate on swelling at lower temperature.

The defocused beam spot size was ~6 mm. A static beam, instead of a rastered beam, was used in order to avoid the well-known suppression of void nucleation and growth due to the pulsed beam effect associated with rastering [15,21,22]. The irradiation used the Texas A&M multiple-beam-deflection procedure to filter out beam-driven contaminants, a procedure deemed to be especially important for carbon [17]. The vacuum of the target chamber was maintained at 6×10^{-8} torr or better during the irradiation. A liquid nitrogen trap located in the last ion-flight segment of the beam deflection apparatus was also used to improve vacuum and further reduce contamination. Temperature was monitored during each campaign using thermocouples mounted on the hot stage with fluctuation less than ± 5°C.

The Stopping and Range of Ions in Matter (SRIM) code was used to calculate the displacement damage in dpa and Fe implant profiles in the Kinchin-Pease mode [23] with displacement energy chosen to be 40 eV [24]. While there has been a debate in the radiation damage community over the use of Full Damage Cascade vs. Kinchin-Pease options of SRIM [25], the Kinchin-Pease mode was selected based on consistency with our series of previous studies and in recognition that dpa levels for all reported neutron irradiations also use the Kinchin-Pease model.

Specimens were characterized by TEM on an FEI Tecnai G2 F20 ST with an operating voltage of 200 kV. TEM specimens were prepared by using a Tescan Lyra-3 FIB following the typical FIB procedure for preparing TEM lamellas. A 30 keV Ga ion beam was used to cut, lift out and thin the TEM lamella and then a 5 keV Ga ion beam was used for final fine polishing of the lamella surfaces. Examination of the ion-incident surface confirmed the absence of polishing-induced deformation. The magnification chosen for each micrograph allowed a full cross-section extending beyond the SRIM-calculated range.

The FIB specimen thickness was measured using the electron energy loss spectroscopy (EELS) technique. The micrograph was divided into 100 nm bins moving away from the ion-incident surface and the void sizes and densities recorded for each bin which was also assigned an average SRIM-predicted dpa value. Swelling (S%) was calculated as $S\% = (100)\Delta V/(1 - \Delta V)$, where ΔV is the volume fraction of voids, calculated by counting the cumulative volume of each individual void rather than using the average void size. Since not all the voids were perfectly spherical, the voids volumes were calculated by assuming ellipsoidal volumes and measuring the longest diameter and shortest diameter. The third diameter of the ellipsoidal calculation was found by averaging the other two. Void sizes and densities were analyzed using Image J software [26].

4.3. Results

4.3.1. The effect of damage level and temperature on the depth distribution of void swelling at a peak dpa rate of 6×10^{-3} dpa/s

Figure 4.1 shows a typical SEM image of the surface of the as-irradiated specimens. The grain boundaries are clearly visible with grain sizes ranging from ~5 μm to ~50 μm. The surface smoothness confirms the good quality of electro-polishing. There are no surface-intersecting precipitates as is expected when using relatively pure iron.

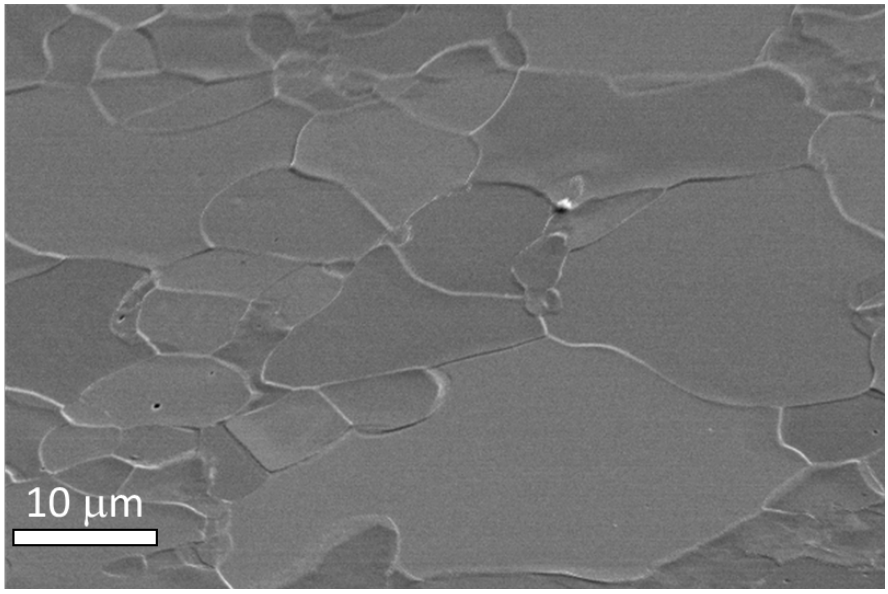

Figure 4.1: SEM image of Fe irradiated to 50 dpa at 475°C and a peak dpa rate of 6×10^{-3} dpa/s.

Figure 4.2 compares typical cross-sectional TEM images of Fe irradiated to 50 dpa, 100 dpa, and 150 dpa at 425°C, 475°C, and 525°C, respectively, performed with a fixed peak dpa rate of 6×10^{-3} dpa/s. Facetted near-spherical voids developed in all nine specimens, but their size and depth distributions are very different. At the lowest

temperature of 425°C, voids develop only in the sub-surface regions (Fig.4.2 a-1 for 50 peak dpa, Fig.4.2 a-2 for 100 peak dpa, and Fig. 4.2 a-3 for 150 peak dpa). As shown by Fig. 4.2 a-4, the enlarged image for the sub-surface region of 425°C/150 dpa specimen (marked by the white dashed line in Fig. 2 a-3), voids appear only in the region located a few 100s of nm from the specimen surface.

In a comparison, near-spherical voids develop over much wider regions at higher temperatures of 475°C (Fig. 4.2 b-1 for 50 peak dpa, Fig. 4.2 b-2 for 100 peak dpa, and Fig. 4.2 b-3 for 150 peak dpa), and 525°C (Fig. 4.2 c-1 for 50 peak dpa, Fig. 4.2 c-2 for 100 peak dpa, and Fig. 4.2 c-3 for 150 peak dpa). Superimposed next to Fig. 4.2 b-3 and Fig. 4.2 c-3 are corresponding normalized SRIM dpa profiles (dark solid line) and Fe implant profiles (dark dashed line). The void distributions at these two temperatures have shapes similar to the dpa profile. The dpa peak is located at about 1.3 μm from the surface and the Fe implant peak is at about 1.5 μm. In addition to the differences in void distributions, the void sizes are sensitive to both irradiation temperatures and dpa level, as would be expected. Voids become larger with increasing temperature or increasing dpa.

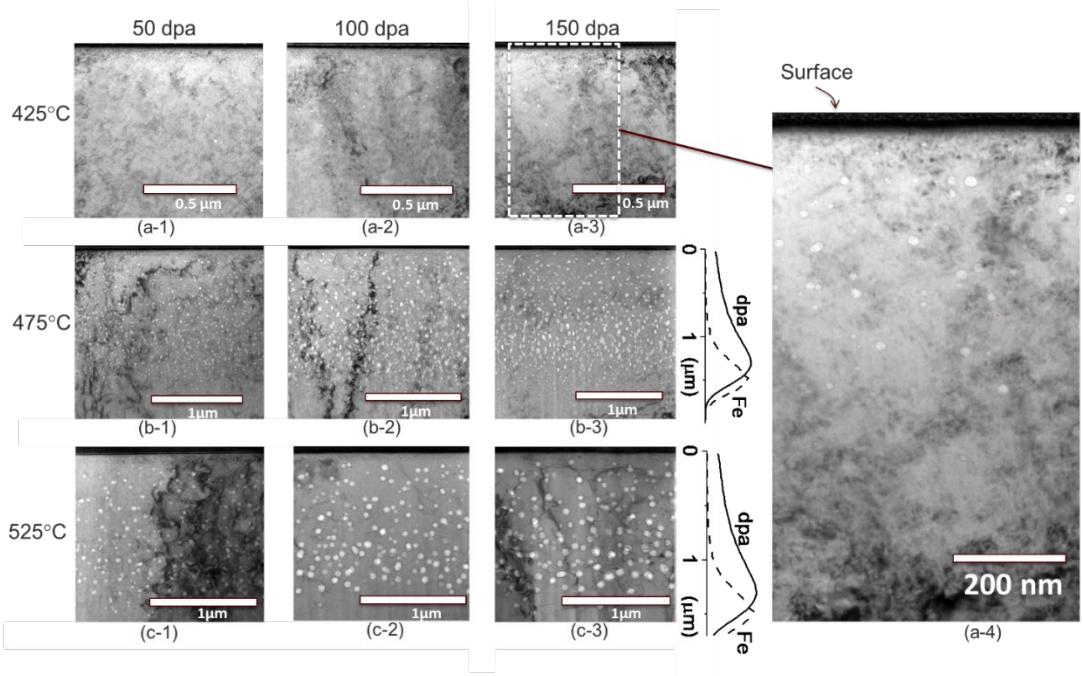

Figure 4.2: Cross-sectional bright field TEM images of irradiated Fe at various conditions: (a-1) 50 dpa at 425°C; (a-2) 100 dpa at 425°C; (a-3) 150 dpa at 425°C; (a-4) 150 dpa at 425°C; (b-1) 50 dpa at 475°C; (b-2) 50 dpa at 475°C; (b-3) 50 dpa at 475°C; (c-1) 50 dpa at 525°C; (c-2) 100 dpa at 525°C; and (c-3) 150 dpa at 525°C. All irradiations were performed using a peak dpa rate of 6×10^{-3} dpa/s.

Figure 4.3 presents results of a typical void analysis using the 475°C/50 dpa specimen. The TEM image of Figure 4.3 (a) is divided into 100 nm bins going progressively deeper into the specimen. Within each bin, all the voids are individually counted and measured. Figure 4.3 (b) shows the SRIM dpa profile and Fe implant profile providing a depth comparison for Figures 4.3 (a and c) to the damage and injected interstitial levels. Figure 4.3 (c) shows the statistical analysis of void distribution for each depth interval. For better visualization and reduction of data scatter 200 nm depth bins are used instead of 100 nm in Figure 4.3 (c), with each curve positioned at the center of the individual bin. These curves present the void density vs.

size at different depths. Note that Figure 4.3 (a) is only one of many TEM images used for the analysis. The total number of voids counted for each specimen is larger than 1000. At each depth, void size distributions are approximately Gaussian in shape and mean void sizes can be extracted as a statistically meaningful parameter.

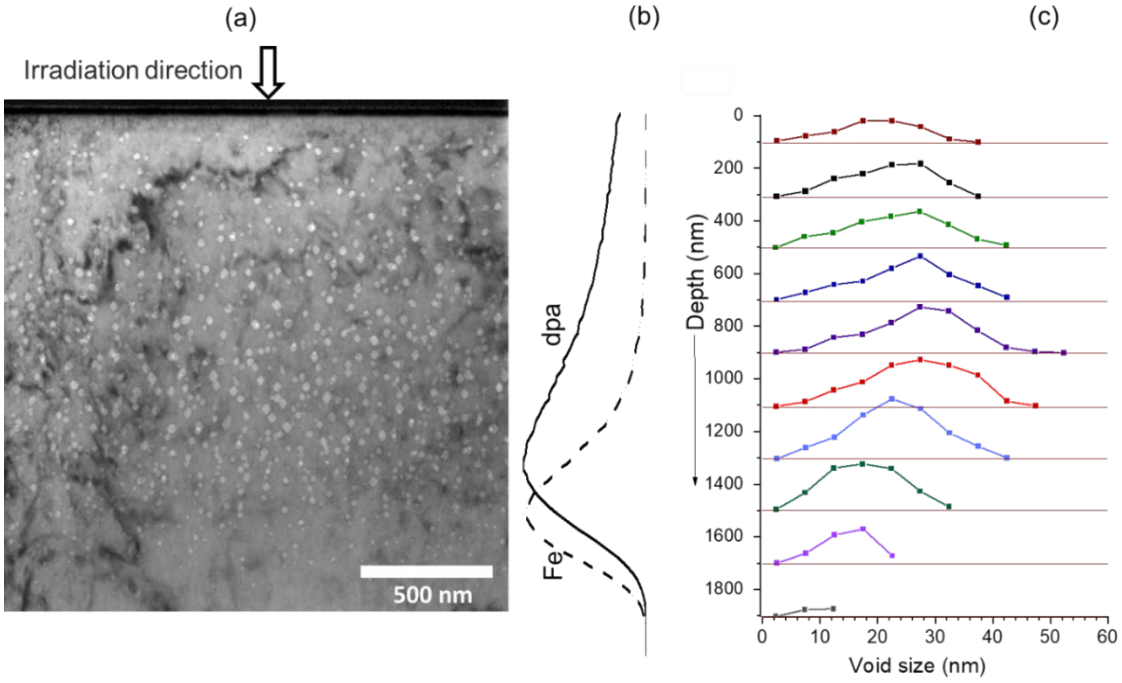

Figure 4.3*:* (a) Cross-sectional bright field TEM image of 475°C/50 dpa/6×10^{-3}dpa/s specimen, (b) normalized SRIM-calculated dpa profile and Fe implant profile, and (c) statistical analysis of void number vs. void size at each depth for a bin size of 200 nm.

Figures 4.4 (a-c) show the void swelling profiles for irradiation temperatures of 425°C, 475°C, and 525°C for a fixed peak dpa rate of 6×10^{-3}dpa/s. At each temperature there are three damage levels of 50 peak dpa (red), 100 peak dpa (black), and 150 peak dpa (green). The solid lines are dpa profiles. As shown in Figure 4 (a), the lowest irradiation temperature of 425°C creates sub-surface swelling peaks rising after moving

in from the denuded zone. The highest swelling is observed in the depth region of 200 to 400 nm. At depths deeper than 800 nm, there are no voids observed.

For a higher irradiation temperature at 475°C, the swelling profiles shift to a much deeper region with the peaks slightly shallower yet close to the dpa profile peak. As shown in Figure 4 (b), swelling peaks at about 1.1 μm to 1.2 μm. Note that the dpa profile peak is at 1.3 μm. At the highest irradiation temperature of 525°C, swelling profiles largely follow the dpa profiles with swelling peaks observed at 1 μm to 1.2 μm. Maximum swelling is sensitive to temperature as well. The maximum swelling at 425°C is less than 1%, while swelling peaks at 475°C and 525°C are close to 15% at 150 dpa. Judged by the observed swelling at all three damage levels, irradiation at 475°C leads to the highest swelling. As expected, swelling near the end of range is depressed at 475°C and 525°C due to the well-known effect of injected interstitials on void nucleation.

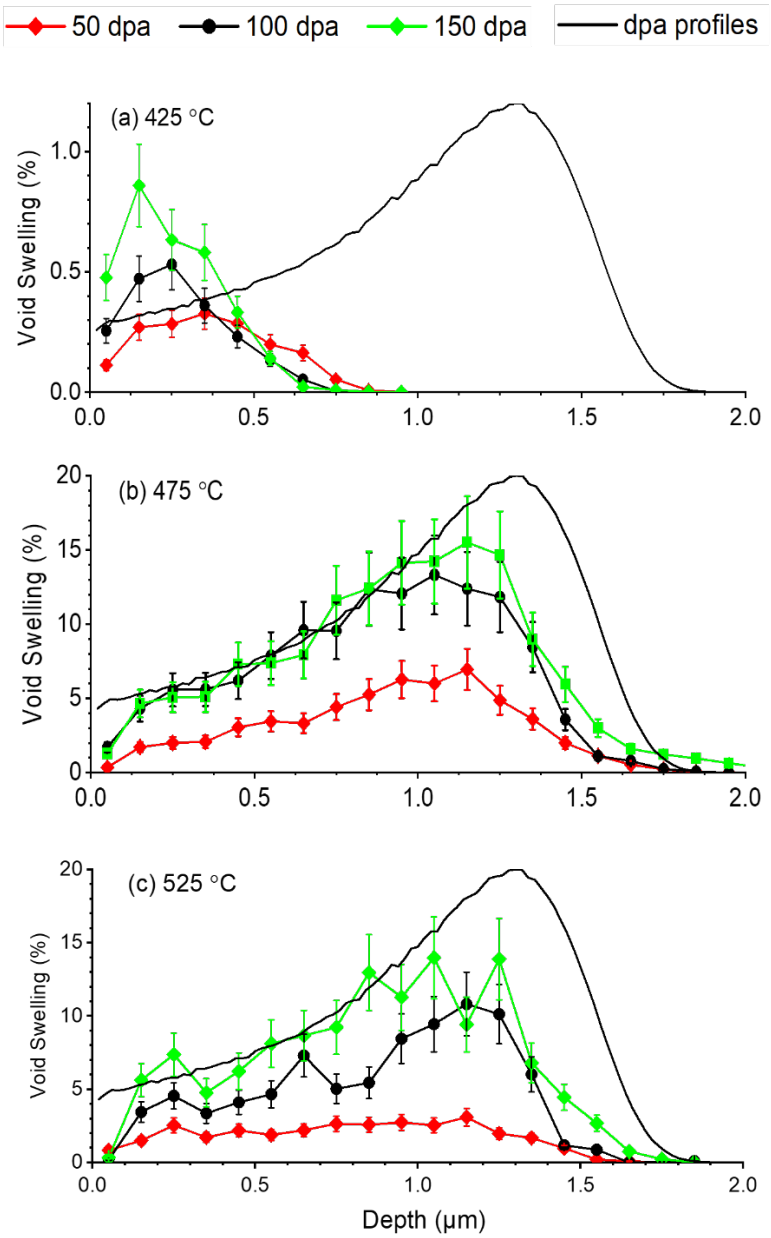

Figure 4.4: Depth distributions of void swelling in Fe irradiated at (a) 425°C, (b) 475°C, and (c) 525°C to peak values of 50, 100, and 150 dpa. All irradiations were performed using the same peak dpa rate of 6×10^{-3}dpa/s. Red denotes the distribution for 50 peak dpa, black denotes 100 peak dpa, and green denotes 150 peak dpa.

Figures .4.5 (a-c) compares the void density as a function of depth at 425°C, 475°C, and 525°, respectively. The density profiles, both their depths and shapes, are similar to that of void swelling. The lowest irradiation temperature of 425°C, as shown in Figure 4.5 (a), shows that the void density peaks in the sub-surface region, at depths about 200 to 400 nm. The other two temperatures, 475°C and 525°C, as shown in Figures. 4.5 (b and c), show voids distributed over the entire irradiated region. For 475°C, the density slightly increases with increasing depth and local dpa values, and the profiles roughly resemble dpa profiles. For 525°C, void density profiles are insensitive to depth and local dpa with the profiles being relatively flat within the irradiated regions, ignoring some fluctuations. One general observation from Figure 4.5 is that the void density decreases with increasing dpa values, most likely due to coalescence of closely adjacent voids as they increase in size.

Figures 4.6 (a-c) compare depth distributions of mean void diameters at irradiation temperatures of 425°C, 475°C, and 525°C, respectively. At 425°C, mean void diameters within the sub-surface swelling peaks are roughly the same, at about 6-8 nm for 50 peak dpa, 9 to 11 nm for 100 and 150 peak dpa, but decreasing somewhat with depth at 150 dpa. At 475°C, void diameters increase with increasing local dpa values, with the maximum sizes reached at a depth 950 nm for all three damage levels. The size increases from 18 nm at the surface to 28 nm at a depth of 950 nm for 50 peak dpa, from 26 nm to 38 nm for 100 peak dpa, and from 31 nm to 45 nm for 150 peak dpa. At 525°C, the void sizes have a weak dependence on local dpa. The mean void sizes range from 32 nm to 38 nm for 50 peak dpa, from 31 nm to 64 nm for 100 peak dpa, and from 41 nm to

74 nm for 150 peak dpa. One general observation from Figure 4.6 is that void size increases with increasing peak dpa values.

Based on Figures 4.4-4.6, the following general observations can be made: (1) void swelling profiles are largely correlated with the void density profiles; (2) void sizes have a weak dependence on local dpa but their spatial differences are less significant than that of void densities; (3) at each temperature, swelling increases with increasing peak dpa; (4) at each temperature void densities decrease with increasing peak dpa; (5) at each temperature the void sizes increase with increasing peak dpa; (6) for the same peak dpa, void densities decrease with increasing temperature; and (7) for the same peak dpa, void sizes increase with increasing temperature.

As will be discussed later and supported by rate theory calculations, observation (1) is sensitive primarily to irradiation parameter selections, especially temperature and dpa rate. Observations (3-7) can be understood assuming local nonconservative Ostwald ripening [15].

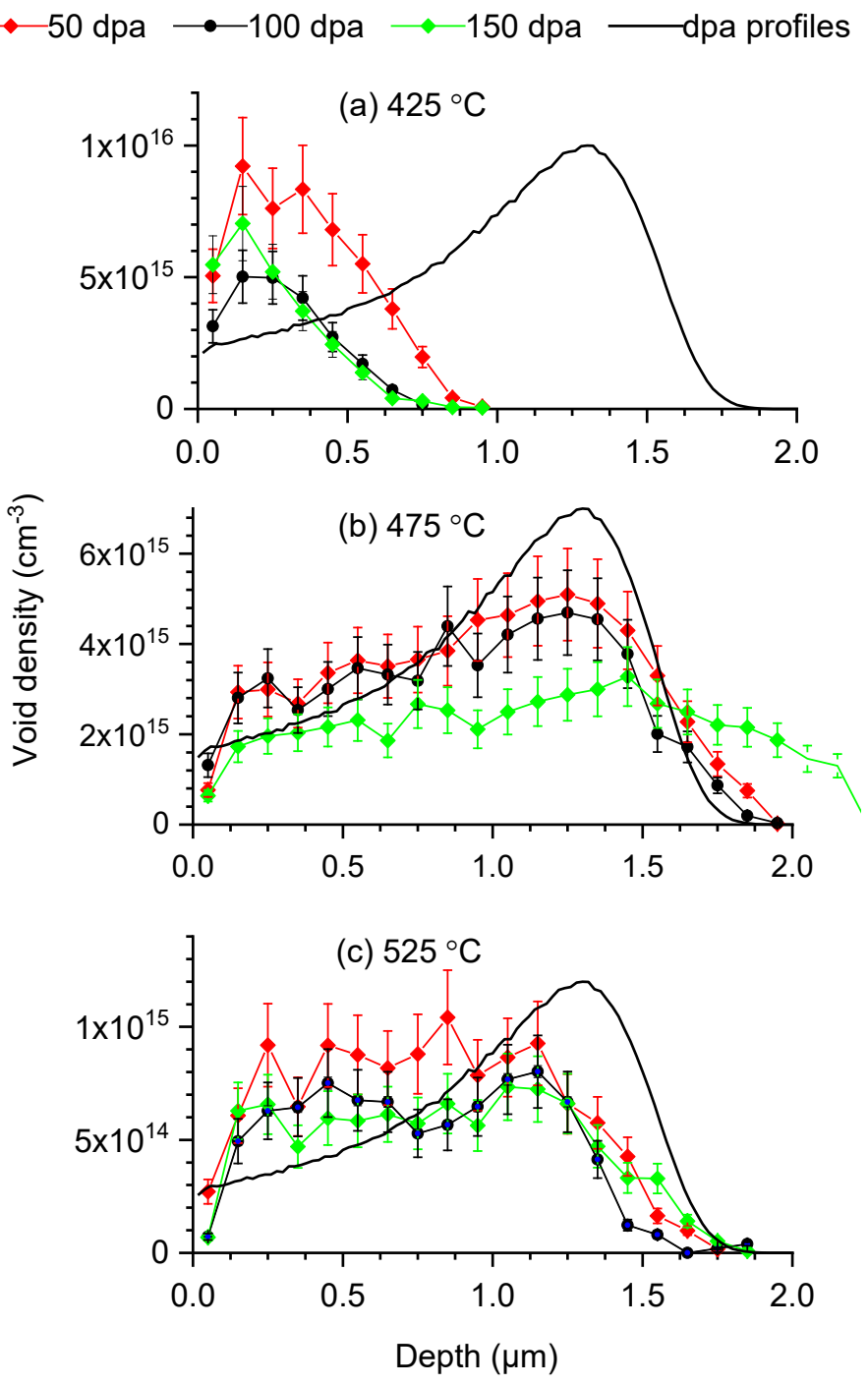

Figure 4.5: Depth distributions of void densities in Fe irradiated at (a) 425°C, (b) 475°C, and (c) 525°C, to peak values of 50, 100, and 150 dpa, performed at a peak dpa rate of 6×10^{-3}dpa/s. Red denotes the distribution at 50 peak dpa, black denotes100 peak dpa, and green denotes 150 peak dpa.

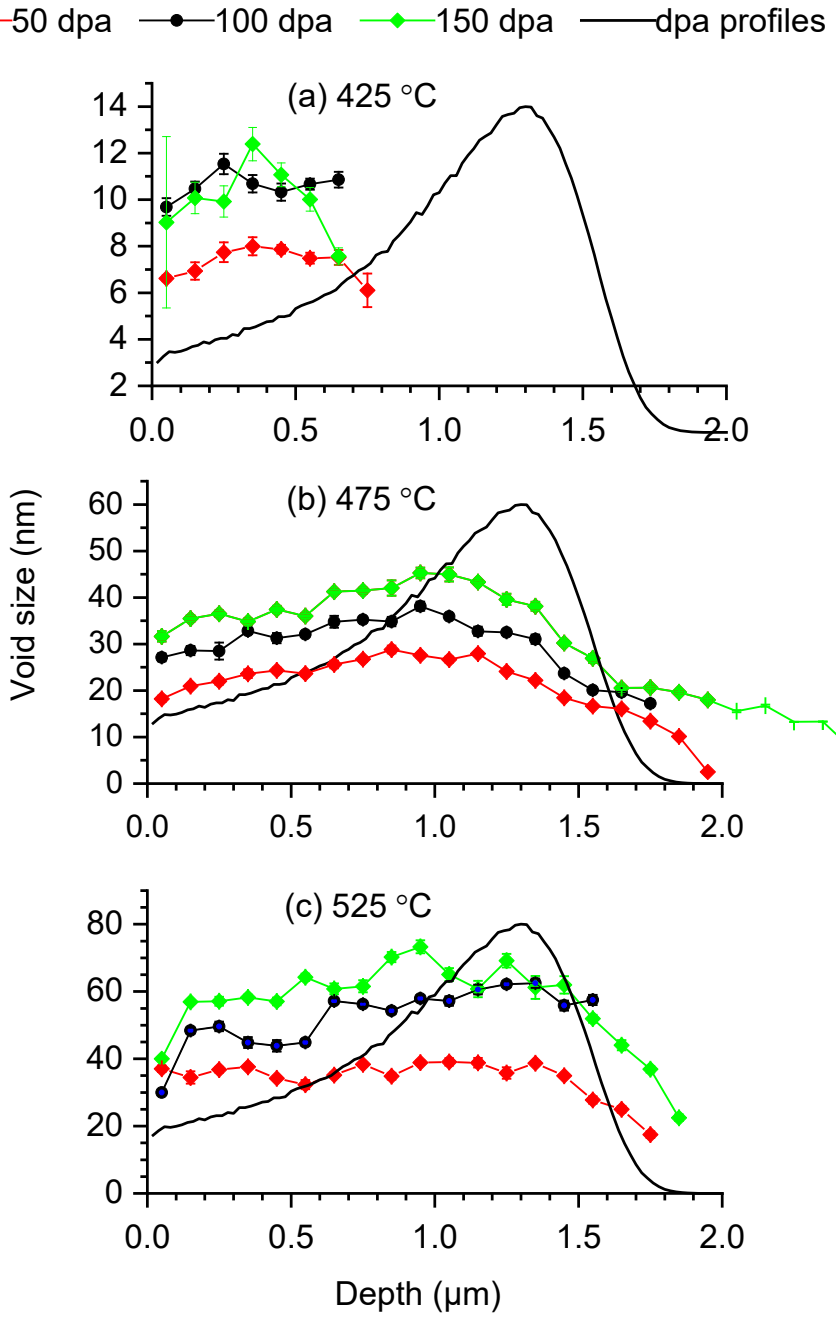

Figure 4.6: Depth distributions of void sizes in Fe irradiated at (a) 425°C, (b) 475°C, and (c) 525°C, up to peak dpa values of 50, 100, and 150 dpa at a peak dpa rate of 6×10^{-3}dpa/s. Red denotes 50 peak dpa, black denotes 100 peak dpa, and green denotes 150 peak dpa.

4.3.2. The effect of dpa rate on void swelling at 425°C

This study has so far has been limited to a rather high peak dpa rate of 6×10^{-3}dpa. One important observation is that irradiation at 425°C at this rate creates a sub-surface swelling peak that does not disappear with increasing dpa level. The sub-surface swelling peak at 425°C and the absence of swelling at deeper regions at higher dose and dose rate appears to be anomalous and is thought to be an artifact of synergistic neutron-atypical aspects of ion irradiation. It is well known that void swelling is strongly sensitive to both dose rate and temperature but in opposite directions such that increasing temperature and decreasing dpa rate induce a similar response, so it was decided to repeat the 50 dpa, 425°C irradiation at two additional lower dpa rates to see if the sub-surface anomaly was indeed sensitive to dpa rate. A single dose level of 50 dpa was chosen because the anomaly at the high dpa rate did not disappear at 100 and 150 dpa. In addition to the highest dpa rate of 6×10^{-3} dpa/s used earlier, a medium dpa rate of 1.2×10^{-3} dpa/s and a lowest dpa rate of 2×10^{-4} dpa/s were used. All other irradiation parameters and procedures employed were identical to that of the highest dpa rate series.

Figures 4.7 (a-c) compare TEM micrographs for 50 peak dpa irradiation at 425°C at the three dpa rates. Figure 4.7 (a-1) shows the cross-sectional TEM image from the highest dpa rate. Figures 4.7 (a-2 and a-3) are enlarged images obtained from the sub-surface region of 0 to 400 nm, and from the deep region of 600 to 1000 nm. High densities of small voids are observed from Figure 4.7 (a-2). Deeper into the specimen, only a few voids are observed from Fig. 4.7 (a-3), consistent with swelling profiles shown in Fig. 4.7 (a). No voids are observed at depths greater than 1000 nm.

Reducing the peak dpa rate from 6×10^{-3} dpa/s changes the void distribution. Fig. 4.7 (b-1) shows the cross-sectional TEM image obtained using the medium dpa rate of 1.2×10^{-3} dpa/s. Both the near surface region (Figure. 4.7 b-2) and deep region (Figure 4.7 b-3) develop voids. For the depth region of 600 nm to 1000 nm, the medium dpa rate significantly increases both void density and void size. The swelling deeper into the specimen is further promoted by decreasing the dpa rate to the lowest value of 2×10^{-4} dpa/s. Figure 4.7 (c-1) shows the TEM image obtained using the lowest dpa rate. Void distributions begin to more closely follow the dpa profile. Much larger voids are observed in both the sub-surface region (Figure 4.7 c-2) and the deep region (Figure 4.7 c-3). Fig. 4.7 shows that reducing dpa rates not only shifts the swelling peak deeper but also promotes swelling over the whole irradiated region. Most importantly, the sub-surface anomaly progressively disappears with decreasing dpa rate.

Figure 4.8 compares the depth distributions of void swelling at different peak dpa rates at 425°C and a peak dose of 50dpa. For the highest dpa rate of 6×10^{-3}dpa/s, swelling peaks at 300-400 nm and no swelling is observed at depths greater than 800 nm. The highest swelling is less than 0.4%.

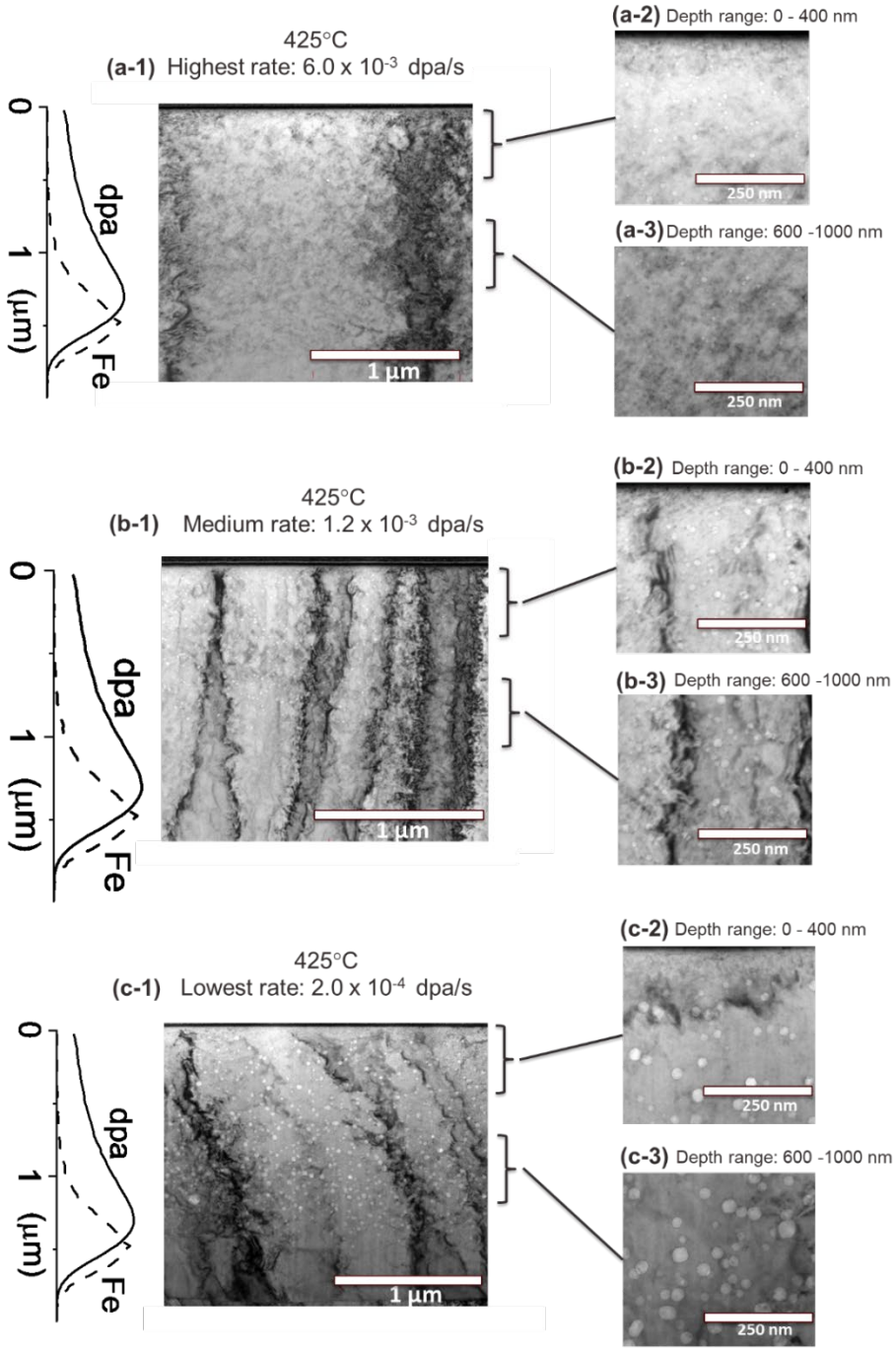

Figure 4.7: (a-1, a-2, a-3) Cross-sectional bright field TEM images obtained at 425°C using the highest dpa rate of 6×10^{-3}dpa/s, (b-1, b-2, b-3) the medium dpa rate of 1.2×10^{-3}dpa/s, and (c-1, c-2, c-3) the lowest dpa rate of 2×10^{-4}dpa/s. TEM images in the sub-surface region of 0 nm to 400 nm (a-2, b-2, c-2) and depth region of 600 nm to 1000 nm (a-3, b-3, c-3).

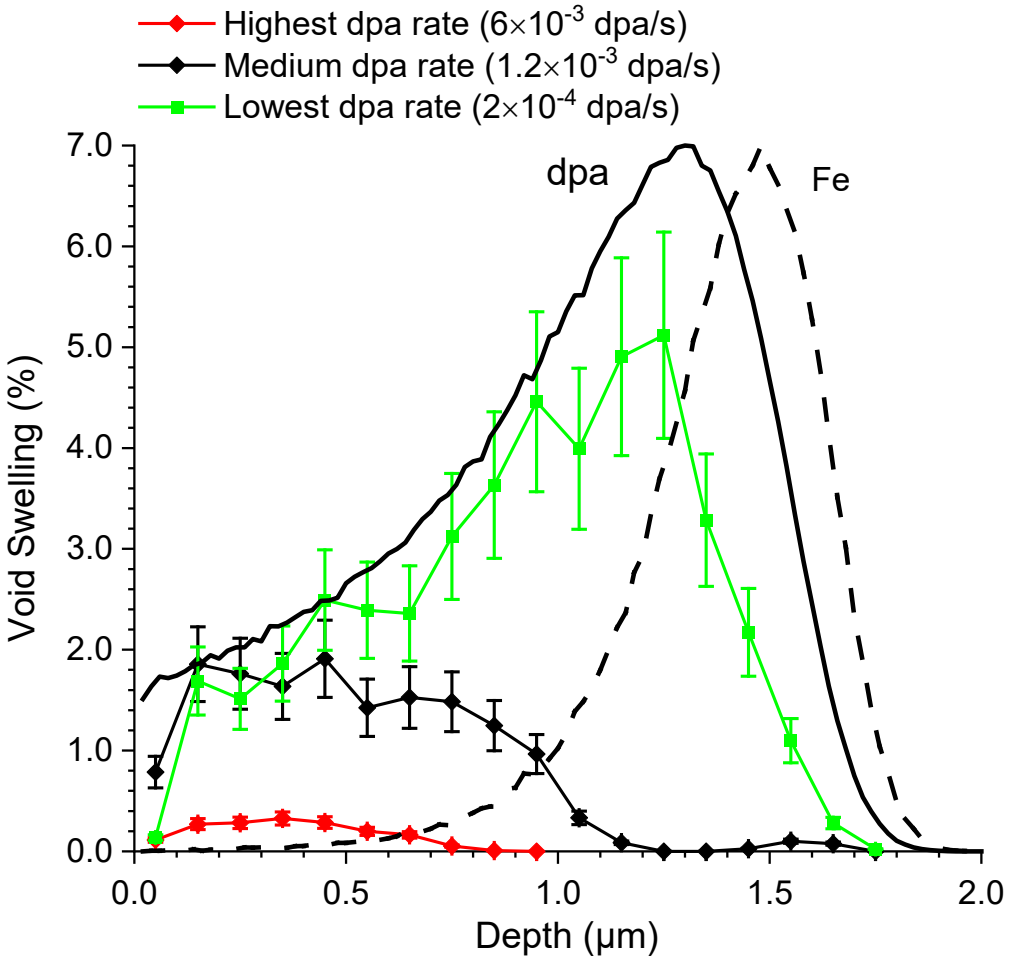

Figure 4.8: Depth distributions of void swelling obtained at 425°C using peak dpa rates of 6×10^{-3}dpa/s (red), 1.2×10^{-3}dpa/s (black), and 2×10^{-4}dpa/s (green). SRIM-calculated dpa profiles and Fe implant profiles are superimposed.

For the medium dpa rate of 1.2×10^{-3}dpa/s, swelling is higher and void distributions penetrate deeply into the specimen, nearly to the end of the dpa profile. Swelling is relatively flat over the depth region of 200 nm to 900 nm, at a level about 1.3% to 1.9%. Swelling quickly drops to almost zero beyond 1000nm, although small voids are still observed at greater depths with a small amount of swelling reappearing at a depth about 1.6μm. At a rate of 2×10^{-4}dpa/s, swelling is significantly promoted. The swelling profile

largely follows the dpa profile, with the maximum swelling of about 5% developed at a depth of about 1.2 μm.

In summary, the sub-surface anomaly is promoted at higher dpa rates and lower temperatures. These factors tend to induce an increasing suppression of void nucleation with increasing depth, resulting in a residual but lesser swelling peak that moves closer to the surface. The following section explores the mechanisms that produce this behavior.

4.3.3. MOOSE simulation of void nucleation rates

In order to identify the fundamentals of the swelling behavior with depth, dpa rate and temperature, the Multiphysics Object-Oriented Simulation Environment (MOOSE) code was used to simulate the void nucleation rates for 5 MeV Fe ion irradiations at different irradiation temperatures and peak dpa rates. Due to the complexity of dealing with the kinetics of defect cluster growth and challenges in both length scales and time scales, the analysis is limited to a zero-time estimation of void nucleation rates. A similar rate theory approach was used earlier to examine the double-peak spatial depth distribution of void swelling of pure iron observed in our earlier study at 475°C using 3.5 MeV Fe ions [3]. The current study at 5 MeV follows the same modeling path employed in the earlier study.

The earlier study used the vacancy migration energy as an adjustable parameter to fit the experimental results, while alluding to the sensitivity of the migration energy to carbon impurity as a possible determinant of the migration energy. The present

simulation, however, employs defect kinetics obtained from first-principle calculations that explicitly consider the effect of carbon on vacancy migration [25]. The effect of carbon has a significant influence on void size and distribution. Our modeling included three steps: (1) the carbon concentration was obtained from SIMS analysis; (2) the influence of carbon on vacancy diffusion kinetics was obtained by extrapolating the previous first-principle calculation results; and (3) the extrapolated vacancy migration energy was used as an input for the rate theory calculations.

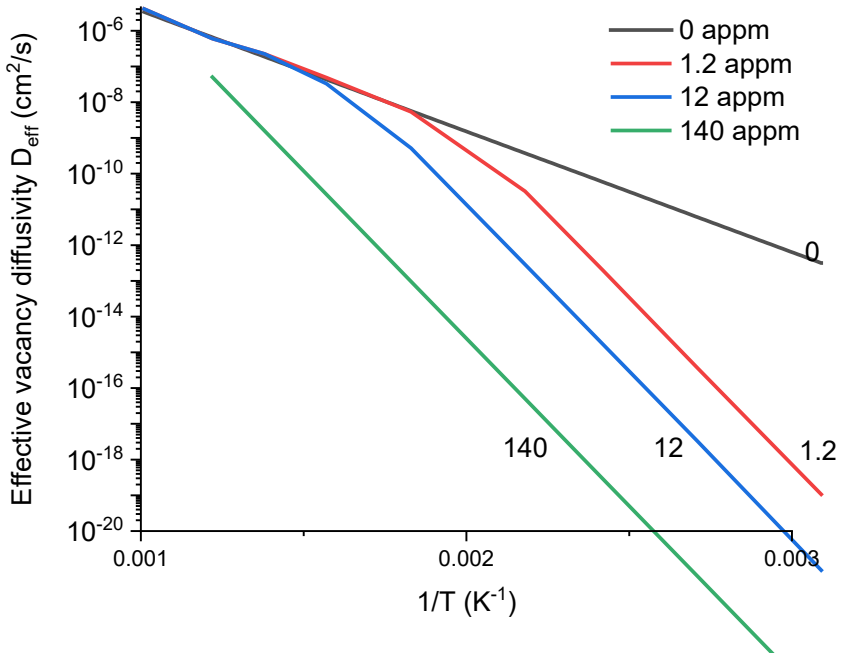

Figure 4.9: Effective vacancy diffusivity as a function of temperatures and C concentrations in Fe (α-iron)

Figure 4.9 shows the vacancy diffusivity (effective values) considering the trapping effect from carbon. The black solid line (0 appm) refers to carbon-free vacancy

diffusion, which has an activation energy of 0.67 eV [27]. With the presence of carbon atoms, vacancy-carbon complexes can form that immobilize vacancies. The complexes can dissociate under some conditions and the vacancies will become mobile. The trapping and dissociation processes are determined by the amount of carbon and the temperature. With increasing carbon concentrations, the reduction in diffusivity becomes larger, leading to reduced vacancy mobility. The transition between carbon-unaffected diffusion to carbon-affected diffusion depends on both temperature and carbon concentration. Thus, carbon concentrations change the pre-factor of the diffusivity equation. Once the system is in the carbon-affected region, diffusivity is governed by a higher activation energy. The proportionality of diffusion pre-factors to carbon concentration and monoenergetic diffusion in the carbon-affected regime make it possible to extrapolate data for an arbitrary carbon concentration. The carbon modified vacancy migration energy is used as input for the following point defect reaction equations [3].

$$\frac{\partial C_v}{\partial t} = f_{survive}K_0 - K_{\perp,v}\rho_\perp C_v - K_{iv}C_vC_i + \nabla D_v \nabla C_v \quad \text{(Eq. 4.1)}$$

$$\frac{\partial C_i}{\partial t} = [f_{survive}(1 - f_{i-cluster})K_0 + K_{II}] - K_{\perp,i}\rho_\perp C_i - K_{iv}C_iC_v + \nabla D_i \nabla C_i \quad \text{(Eq. 4.2)}$$

C_v and C_i are concentrations of vacancies and interstitials respectively. $f_{survive}$ is the survival fraction of defects after damage cascade creation. K_0 is the defect creation rate while K_{II} is the Fe introduction rates as the injected interstitial source, and $K_\perp$ is the dislocation sink strength. K_{iv} is the point defect recombination rate, and D_v and D_i are diffusivities of vacancies and interstitials. Table 4.1 lists the key parameters used in the these simulations, based on either the present experimental conditions or literature data

[3, 27-32]. Under a steady state diffusion when defect concentration profiles are time insensitive, vacancy supersaturation rate, S_v, is calculated using the following equation [3].

$$S_v = \frac{D_v C_v - D_i C_i}{D_v C_v^*} \quad \text{(Eq. 4.3)}$$

The S_v values are converted to void nucleation rates, following reference [3].

$$\log(J_V) = 5.41547 \log(S_v) - 14.6586 \quad \text{(Eq. 4.4)}$$

Table 4.1: Parameters used in the void nucleation simulations

Property	Value	Unit	Source
T	From 698 to 798	K	Present study
$Peak\ DPA\ Rate$	From $6 \cdot 10^{-3}$ to $2 \cdot 10^{-4}$	DPA/s	Present study
D_{0_v}	$5.0 \cdot 10^{17}$	nm^2/s	Present study
E_{m_v}	1.86	eV	[27]
D_{0_I}	$2.09 \cdot 10^{11}$	nm^2/s	[28]
E_{m_i}	0.17	eV	[28]
$r_{\perp_v}$	1.2	nm	[29]
$r_{\perp_i}$	3.6	nm	[29]
$\rho_{\perp}$	10^{-5}	$\#/nm^2$	[30]
∂_{Fe}	0.286	nm	Present study
$f_{survive}$	25	%	[31]
$f_{i-cluster}$	30	%	[32]

Figure 4.10 shows the calculated depth profiles of void nucleation rates at 425°C, 475°C, and 525°C. The peak dpa rate is fixed at 6×10^{-3} dpa/s. At 425°C, void nucleation peaks close to the surface. At 475°C, the void nucleation peak shifts to deeper depth

slightly shallower but close to the dpa peak. At 525°C, the nucleation peak shifts slightly deeper and closer to the dpa peak location. The overall trend for the void nucleation peak depth as a function of temperature agrees with the experimental observations shown in Figures 4.4 and 4.5.

Fig. 4.11 shows the void nucleation rates at 425°C for different peak dpa rates. By reducing the rate from 6×10^{-3} dpa/s to 1.2×10^{-3} dpa/s, the nucleation rate profile evolves from a sub-surface peak to a much broader distribution with a hint of weak peaks at both ends. Further reducing the dpa rate to 2×10^{-4} dpa/s leads to a deeper nucleation rate profile with its peak at a depth very close to the dpa peak. Overall trends agree well with the experimental observations shown in Fig. 8.

To comment on absolute values of void nucleation rates, Figure 4.12 uses the data in Figure 4.11 but without normalization. The peak nucleation rate of 6×10^{-3} dpa/s is about $4\times10^{17}/cm^3$. The rate reduces to about $1\times10^{16}/cm^3$ at 1.2×10^{-3} dpa/s. The rate further reduces to about $1\times10^{14}/cm^3$ at 2×10^{-4} dpa/s. Not only does the profile evolution agree with the experimental result, the overall trend changes of swelling levels also agree with behavior seen in Figure 4.8. For the (425°C/6×10^{-3} dpa/s/50 dpa irradiation), Figure 4.5 shows the peak void density is about $1\times10^{16}/cm^3$, which is reasonably close to the peak value of about $4\times10^{17}/cm^3$ seen in Figure 4.12. Note that the zero-time estimation from the rate theory calculation does not consider coarsening/ripening, which will reduce the void density at long irradiation times and higher damage levels.

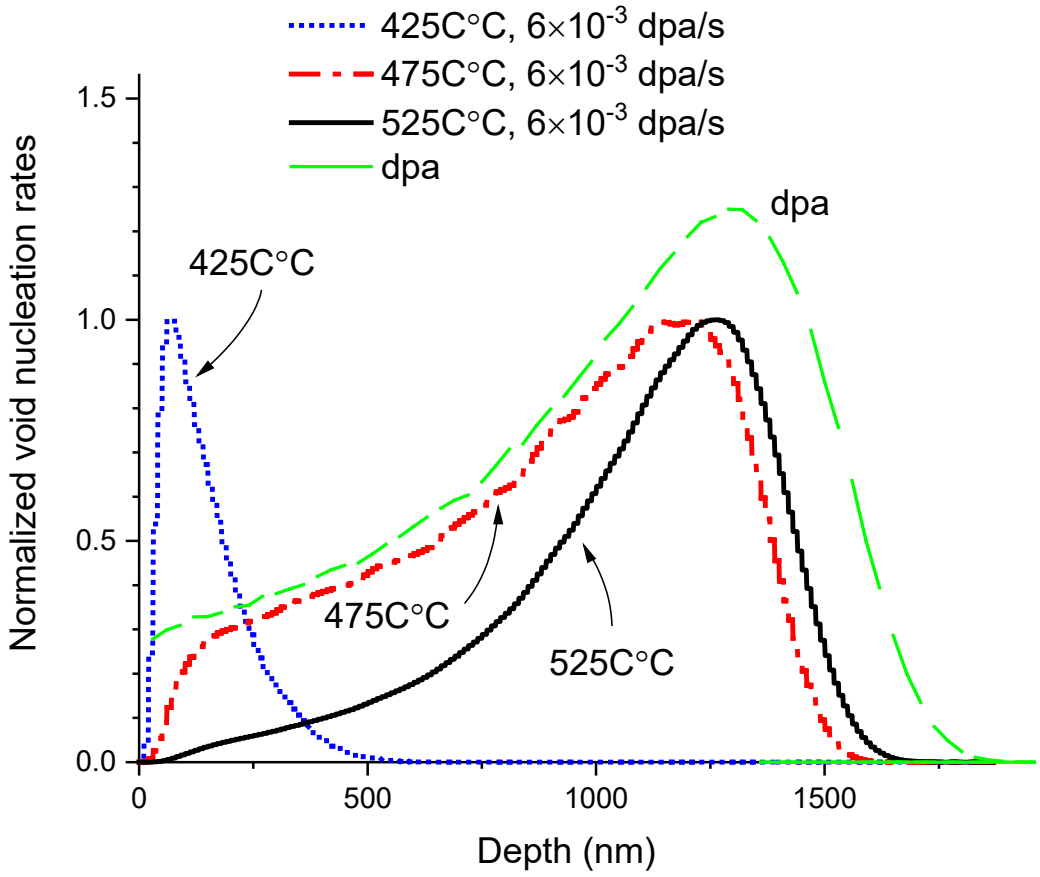

Figure 4.10: Normalized void nucleation rates as a function of depth for 5 MeV Fe ion irradiations of Fe at different temperatures. The peak dpa rate is fixed at 6×10^{-3} dpa/s.

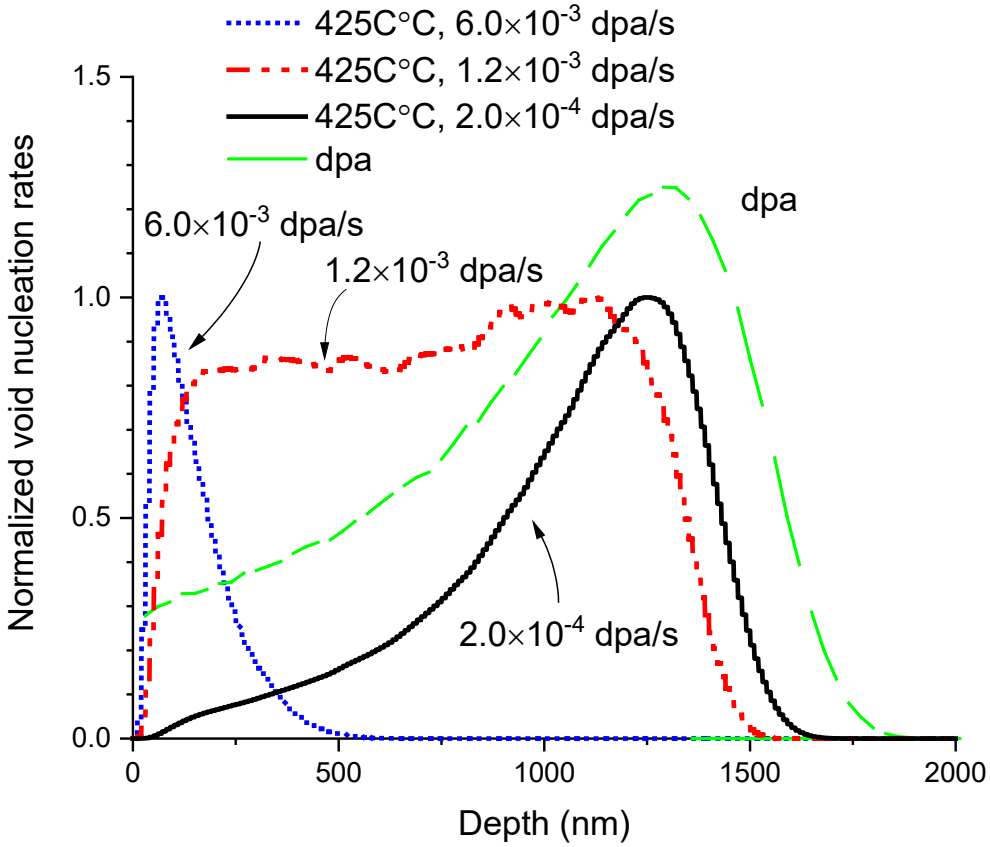

Figure 4.11: Normalized void nucleation rates as a function of depth for 5 MeV Fe ion irradiations of Fe at different peak dpa rates. The irradiation temperature is 425°C

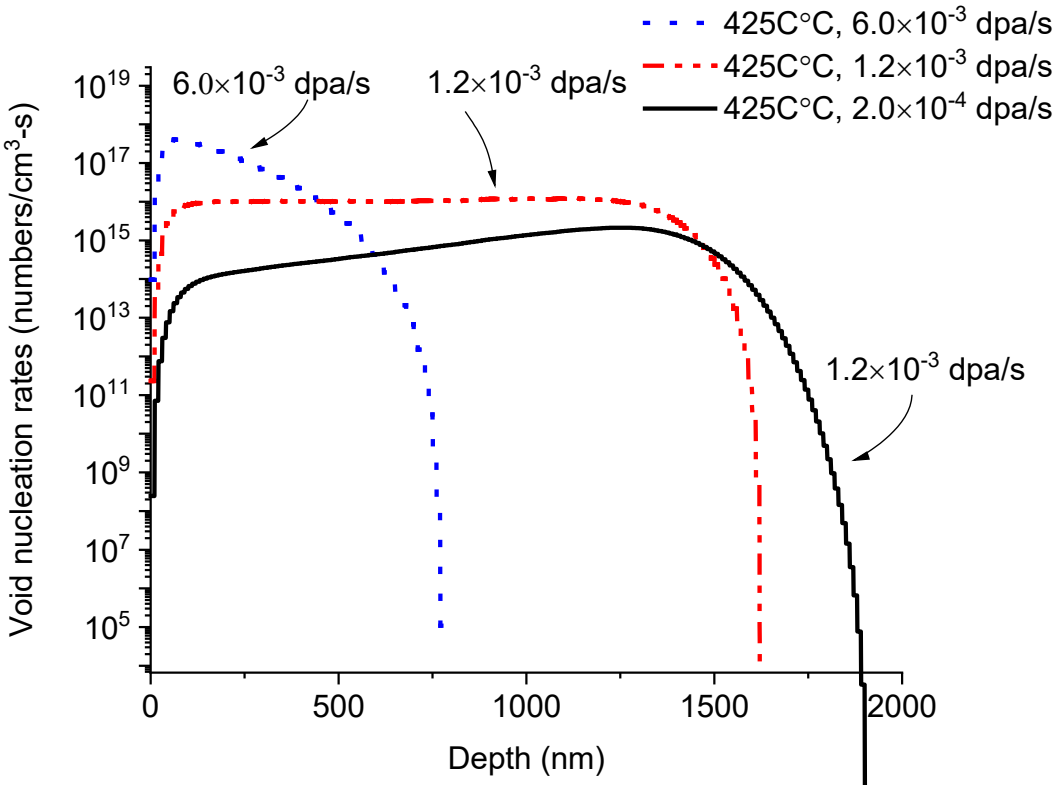

Figure 4.12: Void nucleation rates as a function of depth for 5 MeV Fe ion irradiation of Fe at different peak dpa rates. The irradiation temperature is fixed at 425°C.

4.4. Discussion

Surface swelling peaks or boundary swelling peaks have been observed previously [18,34-35]. It often appears next to the void denuded zones associated with a free surface or a grain boundary [18,34-35]. Such locally enhanced swelling, however, have not been universally observed. Even for pure Fe, several previous studies on self-ion irradiation did not observe sub-surface swelling peaks [6,12], but the most recent study on Ni and He dual ion irradiation of Fe and Fe-Cr did observe sub-surface swelling peaks [11]. The present study shows the complexity of the phenomenon, arising primarily from the sensitivity to ion irradiation temperature and dpa rate.

In most studies the dpa rate is not used as an adjustable parameter, especially to high dpa levels of 50-150 dpa such as used in this study. Accelerator ion irradiation is used due to its high rate of testing and the selection of low dpa rates reduces the time benefit. The present study, however, shows that using a low dpa rate is beneficial for exploring a wider testing parameter range.

Modeling shows thar reducing dpa rates also reduces the sensitivity to carbon levels. Due to differences in specimen manufacturing and thermal-mechanical treatment, the purity plays an important role. The purity control is also largely affected by the details of the ion irradiation, including target chamber vacuum and contamination control methodologies applied. Our recent modeling study has suggested that additional carbon background concentrations can shift swelling peaks towards the surface. The role of adding carbon trapping is similar to lowering the temperature. In both cases, reducing

the dpa rate will mitigate the effect by reducing the influence of the injected interstitial. Hence, a low dpa rate is always preferred in order to avoid sub-surface swelling peaks.

It is correct to say that optimization of irradiation conditions can avoid the appearance of sub-surface swelling peaks. It is inaccurate to say, however, that such optimization can avoid surface-enhanced swelling, since the phenomena may also be due to surface defect sink properties. Early studies have suggested the phenomenon is due to migration of 1-D glissile interstitial loops [20]. This effect may contribute significantly to locally enhanced vacancy supersaturation near the surface, but it is not the sole cause. Since interstitial diffusivity is generally higher than that of vacancies, the near surface point defect profiles or defect flux profiles are different. There is always a small bump-like feature in either the vacancy profile or the vacancy flux profile [6], which will contribute to, at least as a joint participant, the promotion of surface-enhanced swelling.

Whether a surface swelling peak appears or not is largely determined by the injected interstitial effect over the whole irradiated region. To further explain the effect, Figure 4.13 compares the simulation with and without the injected interstitial effects. The injected interstitial effect is excluded by not including extra Fe atoms implanted. Without the injected interstitials, the void nucleation profile begins to follow the dpa profile.

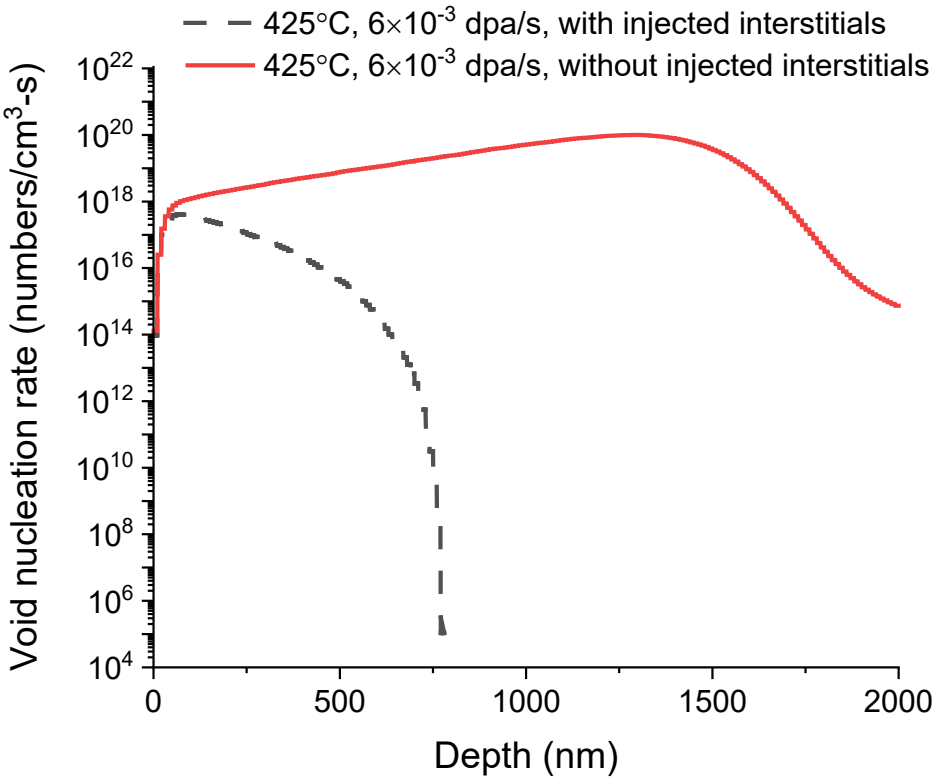

Figure 4.13: Calculated void nucleation rates for 5 MeV Fe-irradiated Fe at 425°C, and at a peak dpa rate of 6×10^{-3}dpa/s, without or without the injected interstitials included.

The sensitivity of the injected interstitial effects on void nucleation was comprehensively studied by Plumton and Wolfer [1]. The authors introduce a nucleation rate equation based on a nonequilibrium counterpart of Gibbs free energy, which is further determined by various defect interactions with a void. The nucleation rates were found to be most sensitive to temperature, dpa rates, the ratio of injected interstitials to dpa rate, and vacancy migration energies [1]. There is an existence of a threshold temperature below which void nucleation is never allowed. This threshold temperature shifts to a higher temperature if (1) the dpa rate is higher, or (2) the ratio of injected

interstitials to dpa rate is higher, or (3) the vacancy migration energy is higher. If the irradiation temperature is slightly higher than this transition temperature, void nucleation still occurs but in a suppressed manner. If the irradiation temperature is much larger than the threshold temperature, void nucleation is much less affected, and the void nucleation profile largely follows the dpa profile. With decreasing temperature, void nucleation become difficult in the peak dpa region, leading to a M-shaped nucleation profile. With further reduction in temperature, the peak dpa region is free of void nucleation, leading to a sub-surface nucleation peak.

Note in Figure 4.10 that the temperatures chosen for the experiment and the modeling at the highest dpa rate do not capture the shift between a deep peak and a sub-surface peak; perhaps 450°C would show the flatter M-shaped profile. Fig. 11 at varying dpa rates, however, captures the shift occurring with such an intermediate profile.

The experimental observations from the present study agree well with the early modeling prediction. The appearance of surface swelling peaks for 425°C/6×10^{-3} dpa/s irradiations can be explained by a threshold temperature which is higher than 425°C. The swelling peak shifting towards the dpa peak can be explained by the reduced threshold temperature when the dpa rate is reduced to 2×10^{-4} dpa/s.

The present study provides experimental observations which validate early nucleation rate theory in heavy ion irradiation testing. The study shows that the sub-surface swelling peak is not a universal feature and can be avoided with parametric optimization. For irradiation tests resulting in a sub-surface swelling peak, the data

should be treated as an artifact. The injected interstitial effect is most significant at low temperature and the problem can be mitigated by reducing the dpa rate. A low dpa rate test also mitigates somewhat the issue caused by carbon contamination, which increases the vacancy migration energy and promotes surface swelling peak formation.

4.5. Conclusions

We have systematically studied the depth distribution of void swelling in 5 MeV self-ion-irradiated iron for a wide range of temperatures, dpa rates and peak dpa values. We also identified the role of carbon contamination at relatively low levels as a contributor to void nucleation. Sub-surface swelling peaks of low magnitude were observed for lower temperature irradiation. The swelling profile shifts deeper, broadens and tends to follow the dpa profile for higher temperature irradiations. For tests requiring low temperatures, reducing dpa rates can avoid surface swelling peaks. MOOSE-based rate theory calculations produce similar swelling peak shifting as a consequence of the combined effect of vacancy imbalance near the surface and especially the injected interstitial suppression of nucleation being enhanced at lower temperature and higher dpa rate. The study identified the key parameters for the optimization of heavy ion irradiation conditions to better emulate neutron damage in metals.

4.6. References

1. D.L. Plumton, W.G. Wolfer, Suppression of void nucleation by injected interstitials during heavy ion bombardment, J. Nucl. Mater., 120, 245-253 (1984).

2. F. A. Garner, Impact of the injected interstitial on the correlation of charged particle and neutron-induced radiation damage, J. Nucl. Mater. 117, 177-197 (1983).

3. M. P. Short, D. R. Gaston, M. Jin, L. Shao, F. A. Garner, Modeling injected interstitial effects on void swelling in self-ion experiments, J. Nucl. Mater. 471, 200-207 (2015).

4. C. Sun, F. A. Garner, L. Shao, X. Zhang, S. A. Maloy, Influence of injected interstitials on the void swelling in two structural variants of 304L stainless steel induced by self-ion irradiation at 500°C, Nucl. Instr. Meth. Res. B 409, 323-327 (2017).

5. E. Kuramoto, N. Yoshida, N. Tsukuda, K. Kitajima, N.H. Packan, M.B. Lewis, L.K. Mansur, Simulation irradiation studies on iron, J. Nucl. Mater., 103&104, 1091 (1981).

6. Lin Shao, C.-C. Wei, J. Gigax, A. Aitkaliyeva, D. Chen, B.H. Sencer, F.A. Garner, Effect of defect imbalance on void swelling distributions produced in pure iron irradiated with 3.5 MeV self-ions, J. Nucl. Mat. 453, 176-181 (2014).

7. E.H. Lee, L.K. Mansur, M.H. Yoo, Spatial variation in void volume during charged particle bombardment — the effects of injected interstitials, J. Nucl. Mater., 85&86, 577-581 (1979).

8. D.B. Bullen, G.L. Kulcinski, R.A. Dodd, Swelling suppression by injected self-interstitials, Nucl. Instr. Methods Phys. Res. B10/11, 561-564 (1985).

9. V.V. Bryk, O.V. Borodin, A.S. Kalchenko, V.N. Voyevodin, V. Ageev, A. Nikitina, V. Novikov, V. Inozemtsev, A. Zeman, F.A. Garner, Ion issues on irradiation behavior of structural materials at high doses and gas concentrations, 11th International Topical Meeting on Nuclear Applications of Accelerators, Bruges, Belgium, 2013.

10. F. A. Garner, L. Shao, M. B. Toloczko, S. A. Maloy, V. N. Voyevodin, Use of self-ion bombardment to study void swelling in advanced radiation-resistant alloys, Proc. 17th International Conference on Environmental Degradation of Materials in Nuclear Power Systems – Water Reactors August 9–12, 2015, Ottawa, Ontario, Canada.

11. Y-R Lin, A. Bhattacharya, D. Chen, J-J Kai, J. Henry, S.J. Zinkle, Temperature-dependent cavity swelling in dual-ion irradiated Fe and Fe-Cr ferritic alloys, Acta Materialia 207, 116660 (2021).

12. Yongchang Li, Aaron French, Zhihan Hu, Adam Gabriel, Laura R. Hawkins, Frank A. Garner, Lin Shao, A quantitative method to determine the region not influenced by injected interstitial and surface effects during void swelling in ion-irradiated metals, J. Nucl. Mat., submitted.

13. Tianyao Wang, Hyosim Kim, Frank A. Garner, Kenneth L. Peddicord, Lin Shao, The effect of internal free surfaces on void swelling of irradiated pure iron containing subsurface trenches, Crystals 9, 252 (2019).

14. N.Q. Lam, S.J. Rothman, R. Sizmann, Steady-state point-defect diffusion profiles in solids during irradiation, Radiat. Eff. 1974, 23, 53–59 (1974).

15. Jonathan Gigax, Eda Aydogan, Tianyi Chen, Di Chen, Lin Shao, Y. Wu, W.Y. Lo, Y. Yang, F.A. Garner, The influence of ion beam rastering on the swelling of self-ion irradiated pure iron at 450°C, J. Nucl. Mater. 465, 343-348 (2015).

16. L. Shao, Jonathan Gigax, Di Chen, Hyosim Kim, Frank A. Garner, Jing Wang, Mychailo B. Toloczko, Standardization of accelerator irradiation procedures for simulation of neutron-induced damage in reactor structural materials, J. Nucl. Mater. 409, 251-254 (2017).

17. Jonathan G. Gigax, Hyosim Kim, Eda Aydogan, Frank A. Garner, Stu Maloy, Lin Shao, Beam-contamination-induced compositional alteration and its neutron-atypical consequences in ion simulation of neutron-induced void swelling, Mat. Res. Lett. 5, 478-485 (2017).

18. A. Bhattacharya, S.J. Zinkle, Cavity swelling in irradiated materials. In: Rudy J.M. Konings, R.E. Stoller (eds.) Comprehensive Nuclear Materials 2nd edition, vol. 1, pp. 406–455. Oxford: Elsevier, 2020.

19. Frank A. Garner (2020). Radiation-Induced Damage in Austenitic Structural Steels Used in Nuclear Reactors. In: Konings, Rudy JM and Stoller Roger E (eds.) Comprehensive Nuclear Materials 2nd edition, vol. 3, pp. 57–168. Oxford: Elsevier.

20. H. Trinkaus, B.N. Singh, A.J.E. Foreman, Impact of glissile interstitial loop production in cascades on defect accumulation in the transient, J. Nucl. Mat. 206, 200-211 (1993).

21. M.T. Myers, S. Charnvanichborikarn, L. Shao, S.O. Kucheyev, Pulsed ion beam measurement of the time constant of dynamic annealing in Si, Phys. Rev. Lett. 109, 095502 (2012).

22. E. Getto, Z. Jiao, A.M. Monterrosa, K. Sun, G.S. Was, Effect of irradiation mode on the microstructure of self-ion irradiated ferritic-martensitic alloys, J. Nucl. Mater. 465, 116-126 (2015).

23. J.F. Ziegler, M.D. Ziegler, J.P. Biersack. SRIM–The stopping and range of ions in matter (2010), Nuclear Instruments and Methods in Phys. Res. B 268, 1818-1823 (2010).

24. A.Yu. Konobeyev, U. Fischer, Y.A. Korovin, S.P. Simakov, Evaluation of effective threshold displacement energies and other data required for the calculation of advanced atomic displacement cross-sections, Nuclear Energy and Technology 3, 169–175 (2017).

25. S. Agarwal, Y. Lin, C. Li, R.E. Stoller, S.J. Zinkle, On the use of SRIM for calculating vacancy production: Quick calculation and full-cascade options, Nucl. Instrum. Methods Phys. Res. B 503, 11-29 (2021).

26. C.A. Schneider, W.S. Rasband, K.W. Eliceiri, NIH Image to ImageJ: 25 years of image analysis, Nature Methods 9, 671-675, 2012.

27. Chu-Chun Fu, E. Meslin, Alain Barbu, Francois Willaime, Vincent Oison, Effect of C on Vacancy Migration in α-Iron. Solid State Phenomena 139, 157-164 (2008).

28. N. Soneda, T. Diaz de La Rubia, Migration kinetics of the self-interstitial atom and its clusters in bcc Fe, Philosophical Magazine A 81, 331-343 (2001), DOI: 10.1080/01418610108214307

29. V. Shastry, T. Diaz de la Rubia. The interaction between point defects and edge dislocation in BCC Iron, ASME. J. Eng. Mater. Technol.121, 126-128 (1999).

30. H. Bhadeshia, R. Honeycombe, Steels: microstructure and properties, Butterworth-Heinemann, 2011, p. 23.

31. L. Malerba, Molecular dynamics simulation of displacement cascades in -Fe: a critical review, J. Nucl. Mater. 351, 28-38 (2006).

32. S.I. Golubov, A.V. Barashev, R.E. Stoller, Comprehensive Nuclear Materials, Chapter 1.13-Radiation Damage Theory, Elsevier, 2012, pp. 358-389.

33. B.N. Singh, S.J. Zinkle, Influence of irradiation parameters on damage accumulation in metals and alloys, J. Nucl. Mater. 217, 161-171 (1994).

34. A. Bhattacharya, E. Meslin, J. Henry, B. Décamps, A. Barbu, Dramatic reduction of void swelling by helium in ion-irradiated high purity α-iron, Mater. Res. Lett. 6, 372–377 (2018).

5. ION IRRADIATION OF NEUTRON PRECONDITIONED STEELS FOR FAST IRRADIATION TESTING

5.1. Introduction

As mentioned in the introduction, reactors subject materials to a very harsh environment with combined effects from radiation, stress and high temperature and, particularly for Generation IV reactors, the environment can be even harsher with vessel materials needing to withstand higher neutron damage levels and higher temperatures. This leads to many issues, but especially swelling that arises from cavity growth when there is an incomplete recombination of the points defects generated along the damage path.

In order to achieve high burn-up of fast reactor fuel it is necessary to contain the fuel in cladding and ducts that resists void swelling and irradiation creep more effectively than is achieved using austenitic steels. Whereas current maximum fuel burn-ups of only 10-11% can be attained in fast reactors for doses of ~100-150 displacements-per atom (dpa) using swelling-prone austenitic steels, optimum higher burn-ups approaching 30% require 250-300 dpa, while some other reactor concepts such as "traveling wave" or actinide "burners" envision neutron doses of 400-600 dpa.

Since currently available fast reactors cannot accumulate more than 20 dpa per year in iron-base structural alloys, and only then in Russia, the international radiation materials community has turned its attention back to charged particle simulation techniques at vastly accelerated dpa rates as neutron surrogates for evaluation of new

alloy concepts and candidates, especially with respect to void swelling and irradiation creep. This is built on a strong historical background discussed in more detail in the introduction of this work. This background, particularly, the US Liquid Metal Reactor (LMR) Program and its "intercorrelation" experiments [1], have shown that electron, ion and neutron irradiations create approximately equivalent radiation hardening if their doses are normalized using dpa units. However, other irradiation phenomena such as swelling and boundary segregation seem not to be dependent only on dpa, but require the consideration of additional factors, especially the dpa rate [2].

Three of the major issues that ion irradiation emulation of neutron damage faces are the lack of neutron typical phase changes in ion irradiation, the dpa rate effect due to an extremely large damage deposition in a short time period, and the injected interstitial effect due to extra atoms being implanted during the ion irradiation testing.

Different phase changes are the consequence of rapid microstructural changes in fast testing using accelerators vs. slower microstructural evolution that occurs in prolonged irradiations using reactors. One important insight gained from the early LMR program is that a major weakness of accelerated ion irradiation was the inability of such experiments to develop the exact phase evolution characteristic of long-term neutron irradiation that usually preceded the onset of void swelling and irradiation creep. This is especially true in swelling-resistant alloys, and was sometimes instrumental in determining the resulting mechanical properties of the material.

The second issue of the dpa rate effect is also the consequence of super fast testing. The large difference in a reactor (dpa rate of 1×10^{-6} to 1×10^{-8} dpa/s) and in an ion

accelerator (dpa rate of 1×10^{-3} dpa/s) gives rise to a phenomenon known as the "temperature shift" [3]. This latter "shift "issue is unrelated to the irradiation technique and is expected to occur no matter what the bombarding species. Various models were developed to predict the amount of temperature adjustment needed for compensating the difference brought by the dpa rate effect. However, these models are limited to the void growth stage, instead of void nucleation state. The effects of dpa rate difference on incubation periods of void swelling are not yet fully understood and modeled.

The third issue of the injected interstitial effect is a unique problem in ion irradiation due to extra atoms being implanted. These extra atoms act as excessive interstitials and suppress both void nucleation and void growth. The effect is most significant in the region around the projected range of implants, and spreads out to significantly reduce the region which can be used to extract reliable swelling data. Prediction of a “safe analysis zone” is still a subject of debate, though early parts of this work have talked extensively about it.

The injected interstitial effect has been discussed along with the surface effect in early parts of this work. However, this work was all done on the simple chemical system of pure iron. Here, we show that all three major issues can be resolved through the approach of “neutron-preconditioned ion irradiation”. Ion irradiation proceeded on AISI 304 stainless steels previous irradiated in the EBR-II fast reactor. 304 stainless steel is a commercial alloy used to construct the EBR-II rector and has been widely used in both boiling water reactors (BWR) and pressurized water reactors (PWR). The neutron irradiation already induces void nucleation typical of a reactor environment.

The second stage of ion irradiation was performed using different temperatures to test the theory of temperature shifting. As will be shown, we can extract a reliable dpa-dependent swelling curve from a single neutron-preconditioned sample after appropriate selection of an ion irradiation temperature and a safe analysis region. The neutron-preconditioning can significantly reduce testing cost and speed up nuclear materials development.

5.2. Experimental Procedure

5.2.1. Neutron irradiation

AISI 304 stainless steels were irradiated in EBR-II at 450°C to 28 dpa. The dpa rate is about 3.2×10-7dpa/sec, which is a damage introduction rate typical of pressurized water reactors (PWR) [4,5]. The samples were cut from a large hexagonal cross-section block (Figure 5.1). The block was the center block of a five-block series stacked in Row 8 of EBR-II (Figure 5.2). The blocks were about 52 mm flat face-to-flat face and have various lengths averaging at about 240 mm. Specimens of about 0.4 mm thickness were sectioned from the neutron-irradiated block using a diamond wafer saw. Mechanical polishing and electropolishing in a concentrated 30% sulfuric acid, 40% phosphoric acid 30% glycerol solution were applied to prepare disks of 3 mm in diameter and of ~200 μm in thickness. Microstructural details of neutron-irradiated samples were previously reported elsewhere [4,5]. A high density of interstitial Frank loops, voids and carbides were observed. Samples used in the present study correspond to 3E1B and 3E1C in the

cutting diagram (Figure. 2). Void size, density, and swelling were previously measured to be ~22.5 nm, $2.61\times10^{21}/m^3$, and ~2%, respectively [4].

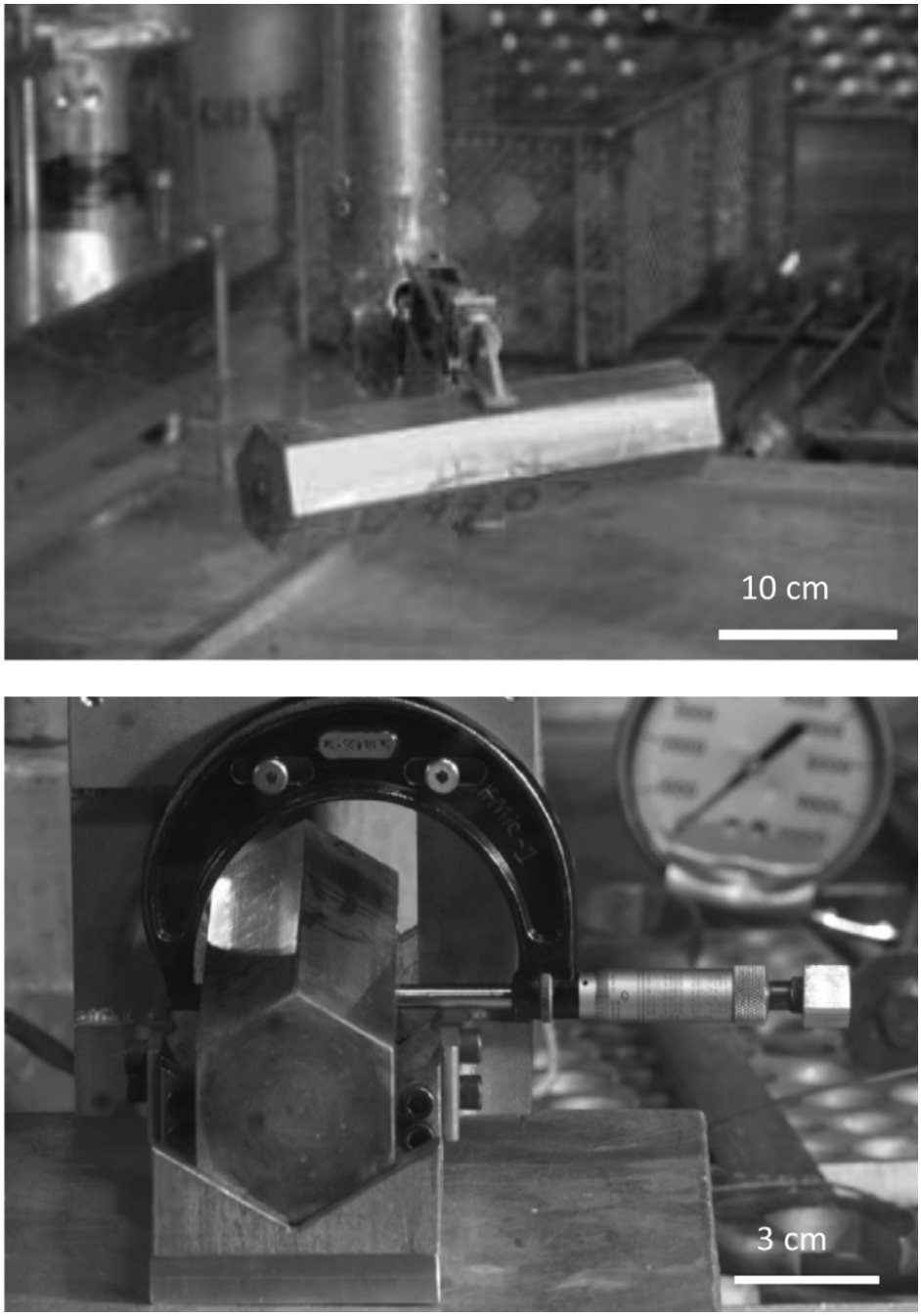

Figure 5.1: AISI 304 SS reflector block in the hot cell [4].

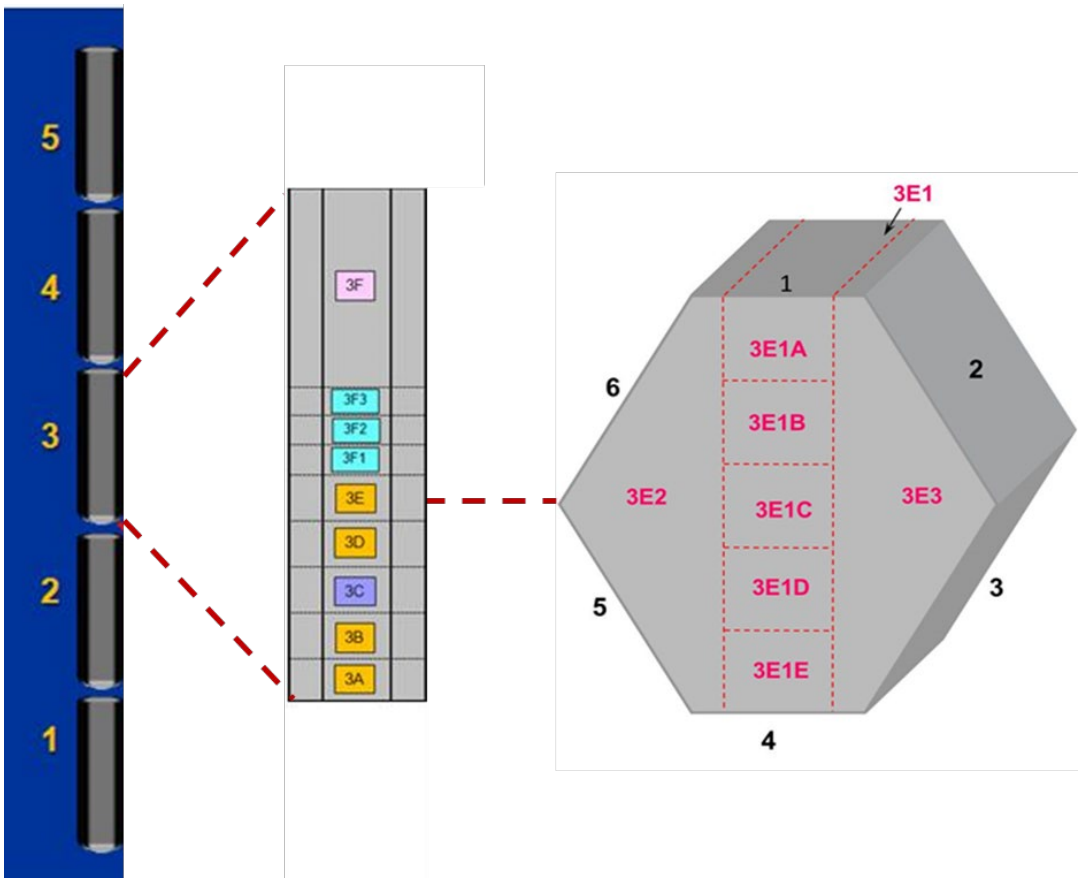

Figure 5.2: Cutting diagram for the block used for the project. The samples are prepared from the region corresponding to 3E1B and 3E1C.

5.2.2. Ion Irradiation

TEM disks of neutrion-irradiated304SS were irradiated with 5 MeV Fe^{2+} self-ions, using a 3 MV NEC tandem accelerator. The ion irradiation temperatures were 450°C, 500°C, 550°C, and 600°C, respectively. Note that 450°C is the neutron-irradiation temperature. At each temperature, ion irradiation fluences are equivalent to adding an additional 25, 50, and 75 peak dpa to the already present 28 dpa of neutron damage. The Stopping and Range of Ions in Matter (SRIM) code was used to simulate dpa profiles

and Fe implant profiles [6]. The Kinchin-Pease (K-P) calculation model was used, for the consistency with neutron damage simulations. The displacement threshold energies of Fe and alloying elements were 40 eV [7]. A static beam of beam spot size of 6mm×6mm was used, to avoid pulsed beam effect [8]. The multiple beam deflection technique was applied to minimize beam contamination [9,10]. The chamber vacuum during the irradiation was 6×10^{-7} torr or better.

5.2.3. Transmission electron microscopy characterization

The focused ion beam liftout technique was used to prepare specimens for transmission electron microscopy characterization. Swelling(S%) is calculated as $S\%=(\Delta V\%)/((1-\Delta V\%))$, where $\Delta V\%$ is the fraction of volume occupied by voids, and is calculated by counting each individual void. Void sizes and densities were analyzed using Image J software [11].

Figure 5.3 shows both the bright field TEM micrographs and the swelling results for the neutron irradiated only sample as well as the 75 peak dpa additional ion dose for the sample at 450°C, 500°C, 550°C, and 600°C, respectively. The original swelling level as characterized from the as received sample is shown in green. Also, as the swelling level increases, the injected ions start flying through a lot of empty space, thereby resulting in range extension and shift in both the dpa curve and injected ion implant profile. Both the unshifted and range extended profiles are shown. The swelling within ion irradiated region is reduced at 450°C, saturated at 500°C, slightly increased at 550°C, and significantly increased at 600°C.

Figure 5.4 shows the results of the void characterization for both the void densities and void diameters for these samples. Rather than showing raw data for these graphs however, Figure 5.4 shows the data normalized to the background level seen at the end of the ion range. In this way, any effects from annealing during the irradiation are eliminated. Void sizes are reduced at low temperature and increased at high temperature. Void densities are reduced at low temperatures and increased to a saturated value at high temperatures.

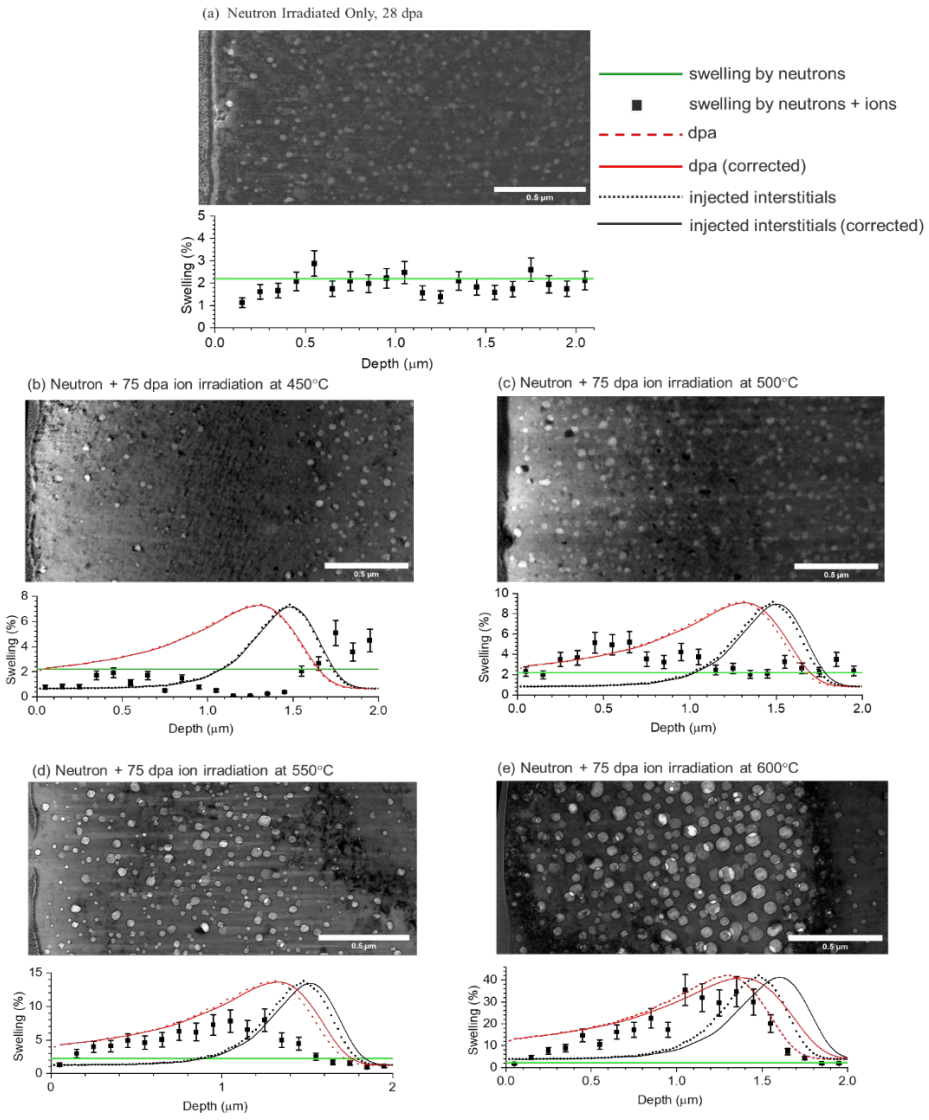

Figure 5.3: Cross sectional TEM images of neutron-irradiated and neutron + ion irradiated samples, and corresponding swelling depth profiles. (a) neutron irradiation only (at 450°C, equivalent to 28 dpa). (b) neutron (450°C/28 dpa) + ion irradiation (450°C/75 peak dpa). (c) neutron (450°C/28 dpa) + ion irradiation (500°C/75 peak dpa). (d) neutron (450°C/28 dpa) + ion irradiation (550°C/75 peak dpa. (e) neutron (450°C/28 dpa) + ion irradiation (600°C/75 peak dpa). The green line is the average swelling in neutron-irradiated-only sample. The red dash line is the SRIM-calculated dpa profile by 5 MeV Fe ion irradiation. The red solid line the dpa profile considering the effect of porosity in range extension. The black dashed line is SRIM-calculated Fe implant profile. The black solid line is the corrected profile considering porosity.

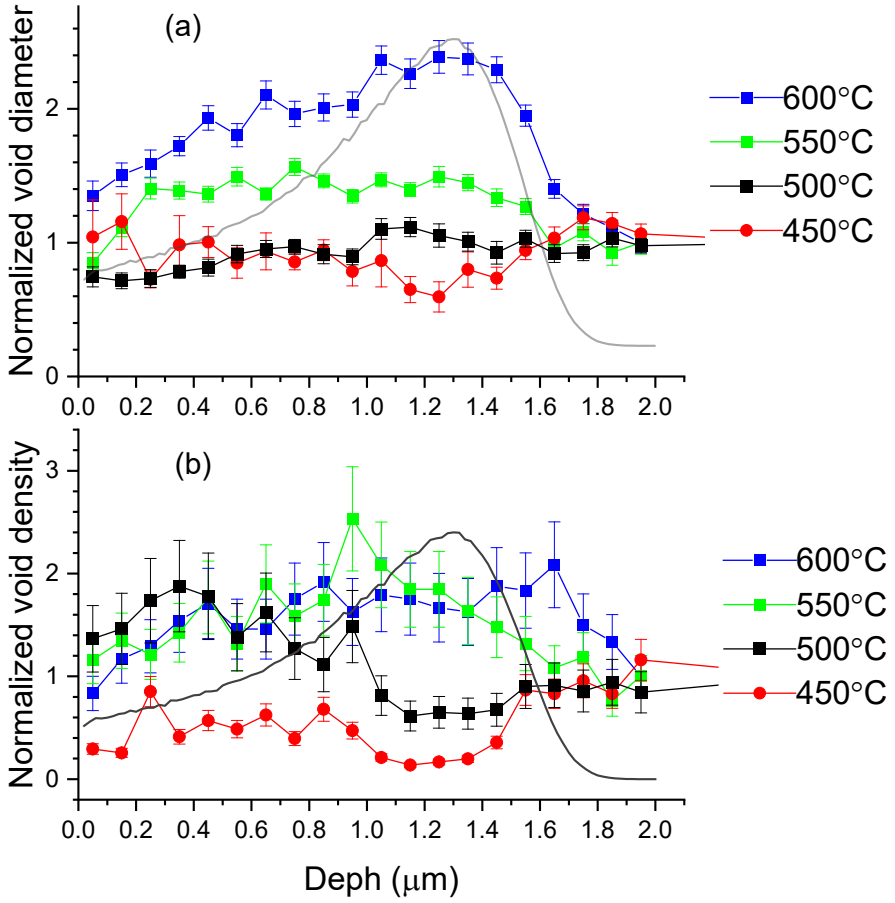

Figure 5.4: Void size and density changes in ion-irradiated neutron-preconditioned samples. Depth profiles of void sizes after 5 MeV Fe self ion irradiation at 450°C, 500°C, 550°C, and 600°C, respectively. (b) Depth profiles of void densities after 5 MeV Fe self ion irradiation at 450°C, 500°C, 500°C, and 600°C, respectively. Void sizes are reduced at low temperature and increased at high temperature.

5.3. Results

5.3.1. Temperature shifting and dpa rate effect

Adding additional radiation damage by using fast ion irradiation does not necessarily promote swelling. If the ion irradiation temperature is kept at the same temperature as the reactor irradiation temperature, swelling is reduced and even diminished (a

comparison from Figures. 5.3 a and b). For the neutron-only irradiated sample, spherical voids are randomly distributed, with an average void size of about 20 nm (Figure. 5.3 a). The average swelling is about 2% after neutron irradiation at 450°C (green line in Figure. 5.3 a). For the ion irradiation performed at the same temperature as the reactor irradiation, 450°C, the overall swelling is reduced in the ion damage region. Furthermore, there is a band of void-free region at the depths of 1.1 μm to 1.4 μm (Fig. 5.3 b). The void disappearance region matches well with the dpa profile (the red line in Fig. 1b) and the Fe implant profile (the black dashed line in Fig. 3b, peaks at about 1.5 μm). This is clear evidence of the injected interstitial effect, which is a function of irradiation temperature, local dpa rate, and the ratio of the injected interstitial numbers to dpa numbers. Early modeling studies have suggested that the injected interstitial effect becomes significant at lower temperature, higher local dpa rates, and higher ion deposition rate [12].

Increasing the ion irradiation temperature to 500°C, which is 50°C higher than the reactor irradiation temperature, is able to slightly increase swelling in the near surface region, and keep roughly the same swelling level at the dpa peak region (Figire. 5.3 c). In the swelling enhanced region, at depths from 0.3 μm to 1.1 μm, void sizes become slightly larger than the neutron-irradiated samples, suggesting this region is less affected or unaffected by the injected interstitial effect.

Increasing the ion irradiation temperature to 550°C further increases local swelling (Figure. 3 c). Swelling within the irradiated region has an overall enhancement in comparison with the neutron irradiated sample, and the swelling profile becomes closer

to the dpa profile. Void sizes (~34 nm) become noticeably larger than the neutron-only sample (~20 nm). Still, the amount of swelling increase does not reach the expected level. Swelling reaches a maximum ~8% at depth ~1.15 μm, which is slightly shallower than the dpa peak.

At the highest ion irradiation temperature of 600°C, swelling is significantly increased over the whole ion irradiated region. Very large voids, up to 60 nm, are observed. At such a high swelling level, the effect of porosity on the ion range extension must be considered. The actual dpa peak, after being corrected, shifts about 100 nm deeper [solid red line in Figure. 5.3 e). The depth of the maximum swelling (reaching about 35% at depth ~1.25 μm) is shallower than the dpa peak location, suggesting the injected interstitial effect still plays a role. The ion range extension (shifting of Fe implant peaks) are 0.01, 0.03, 0.05, and 0.13 μm for 450°C, 500°C, 550°C, and 600°C, respectively (Fig. 5.3 black solid vs dashed lines). For the dpa correction, the depth is divided into a bin of 100 nm (the same bin size of swelling analysis). At each bin, the average porosity change, assuming a linear swelling increase as a function of irradiation time, is used to adjust the bin width.

Reduced void swelling at the lowest temperature of 450°C is contributed to by both void size shrinkage (Fig. 5.4 a) and void density reduction (Fig. 5.4 b). Both changes are the largest in the dpa peak region. At 500°C, void sizes over the whole ion-damage region are comparable to the size prior to the ion irradiation (Fig. 5.4 a). Spatial difference of void swelling is largely determined by spatial difference of void density. Void densities are increased in the near surface region and become reduced in the deeper

regions, starting at about 1μm. The void density forms a dip like profile with the lowest densities around the dpa peak region. The amount of density reduction (up to 40%) in the dpa peak region, however, is less than that at 450°C (Figure. 5.4 b). At 550°C, there is an overall size growth (by about 50%) over the whole ion-damaged region, resulting in a relative flat size profile (Fig. 5.4 a). The void density profile shows fluctuations but the overall density profile does not show a close correlation with the dpa profile (Figure 5.4 b). At the highest temperature, 600°C, void size increase show a strong correlation with the dpa profile. The void density profile at 600°C, on the other hand, does not show noticeable dpa dependence. Instead, the densities exhibit saturation within the irradiated region (Fig. 5.4 b).

5.3.2. Safe analysis zone

Void size shrinkage and swelling suppression at the depth region around the Fe implant peak can be understood by the injected interstitial effect in which extra interstitials participate into local point defect recombination and reduce the amount of vacancies available for vacancy-void interactions. Shifting of the vacancy supersaturation level under the injected interstitial effect to a lower value also changes the competitive growth of voids of difference sizes. If the average vacancy concentration under ion irradiation becomes lower than the vacancy concentration established previously in the quasi steady state of void grow in reactors, large voids will shrink in the following ion irradiation.

The safe analysis zone (the region not affected by the injected interstitials effect) can be identified by plotting swelling vs. local dpa. If there is no injected interstitial effect, swelling solely depends on local dpa. Thus, the swelling at depths less than the dpa peak and depths greater than dpa peak follows the same local dpa dependence curve. In a comparison, under the injected interstitial effect, swelling-dpa dependence become asymmetric: the swelling at depths less than the dpa peak is greater than swelling at depths greater than the dpa peak, since the Fe implant peak is located deeper than the dpa peak.[13]

As shown in earlier parts of this work, the safe analysis zone can similarly be identified by plotting void diameter as a function of local dpa (Figure 5.5a). The change from a steep initial slope to more gradual slope for the void diameter identifies the surface effected region while the inflection point identifies the region affected by the injected interstitial. When multiple samples irradiated under the same conditions but to different peak doses are placed on the same plot one can identify where the slopes remain consistent and thus identify the safe analysis region for a series of doses. This has an internal consistency across samples under the same irradiation conditions. Figures 5.5b and 5.5c show the surface boundaries and injected interstitial boundaries respectively. Finally, all the swelling data from the safe analysis zones can be plotted together to yield the swelling trend to high doses against local dpa. Figure 5.5d.

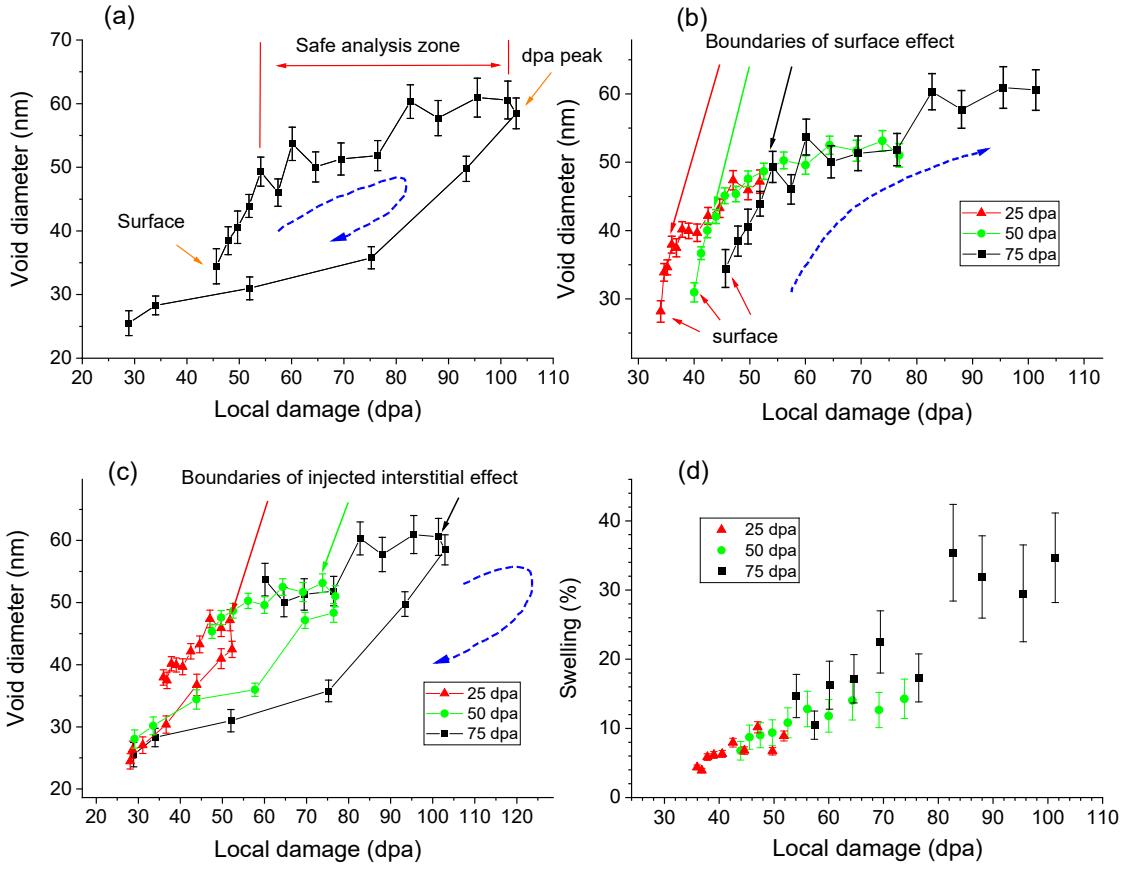

Figure 5.5: Identification of safe zone and the comparison of swelling within the safe analysis zones for 600°C ion irradiation of various peak dpa. (a) Void diameters as a function of local dpa for 75 peak dpa irradiation at 600°C. (b) Void diameters as a function of local dpa for 25, 50, and 75 peak dpa, all at 600°C showing only the surface effected region up to the irradiation peak. Surface boundaries are also marked. (c) Void diameters as function of local dpa for 25, 50, and 75 peak dpas, all at 600°C, showing only the middle depth range to end of range. Injected interstitial boundaries are marked. (d). Swelling vs local dpa for 25, 50, and 75 peak dpa, all at 600°C showing data points from the safe analysis region.

5.3.3. Extracting swelling-dpa curve from a single set of irradiation conditions

With temperature adjustment to compensate the dpa rate effect and the safe zone analysis to exclude both the surface and injected interstitial effects, it is feasible to use one set of ion irradiation experiments to different doses to obtain a swelling-dpa curve,

providing data for extrapolation towards extremely high dpa conditions. This greatly increases the testing efficiency and consistency. Figure 5.6 summarizes void swelling as a function of dpa (for neutron only irradiations) and local dpa (for neutron + ion irradiations). At the highest temperature 600°C, swelling suggests a swelling incubation period of about 20-25 dpa, and swelling rate of 0.75% per dpa in the steady state growth stage. There was no dpa dependent neutron irradiation data for the same alloy (except for one data point at 28 dpa). The swelling data fast neutron irradiated 304L SS, an alloy close to 304H SS, is plotted for a comparison (Figure 5.6). Due to the differences in irradiation temperature and dpa rate, the swelling incubation period is expected to be different. Note that the swelling rate of neutron-irradiated 304L SS is very close to neutron + ion irradiated 304H. The overall swelling behaviors of the two alloys are reasonably close.

Swelling of neutron + ion irradiated samples at the other three ion irradiation temperatures (450°C, 500°C, 550°C) shows not only significantly reduced swelling, but also reduced (or saturated) swelling at higher local dpas (Figure 5.6). Because of the combined dpa rate effect and the injected interstitial effect, these swelling data cannot be used to represent swelling resistance of the alloy.

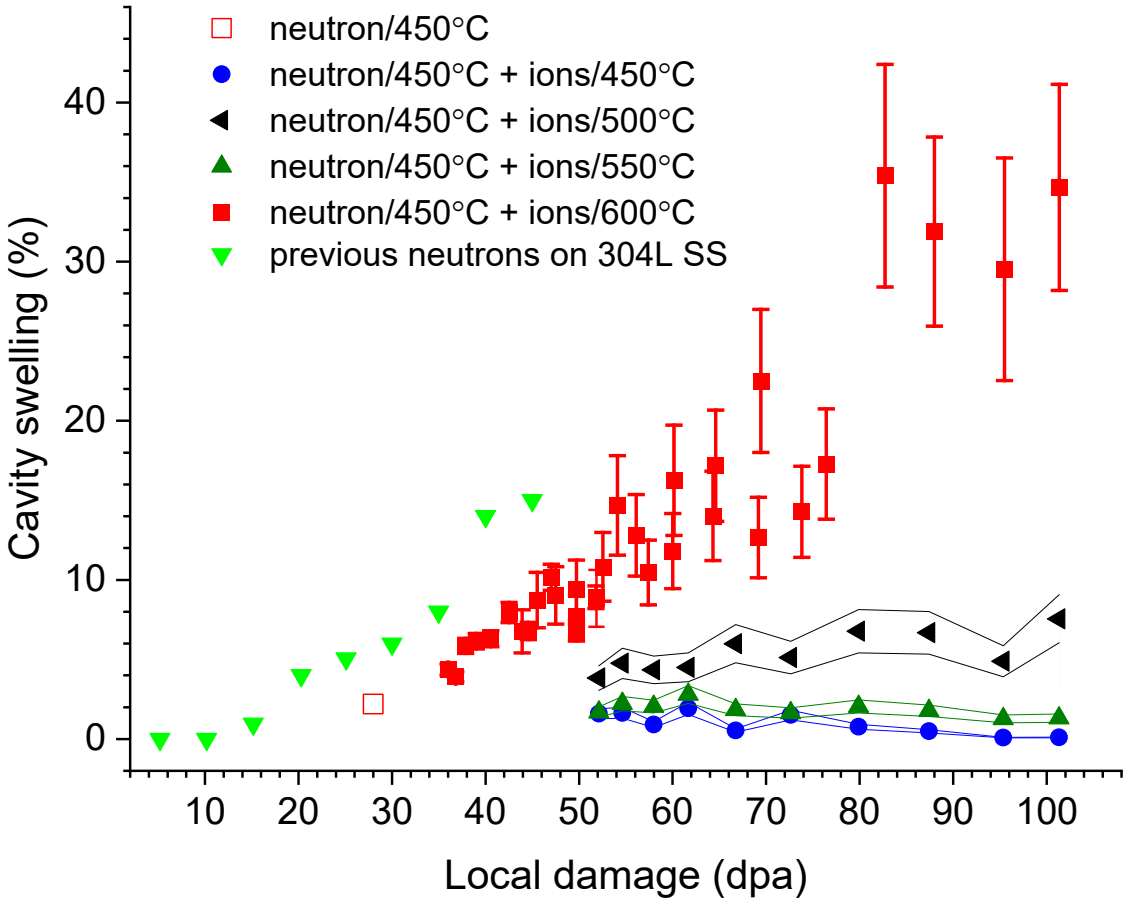

Figure 5.6: Swelling as a function of damage levels from previous neutron irradiation and the present neutron + ion irradiation studies. Hollow square refers to 28 dpa/450°C neutron irradiated 304H SS. Circle refers to 28 dpa/450°C neutron + 75 peak dpa/450°C ion irradiated 304H SS. Up-pointing tringle refers to 28 dpa/450°C neutron + 75 peak dpa/500°C ion irradiated 304H SS. Left-pointing tringle refers to 28 dpa/450°C neutron + 75 peak dpa/550 °C ion irradiated 304H SS. Solid square refers to 28 dpa/450°C neutron + (25, 50, and 75 peak dpa safe zone) samples at 600°C ion irradiated 304H SS. Down-pointing triangle refers to fast neutron irradiated 304L SS. Ion irradiation at 600°C continues void growth of neutron-preconditioned samples in a swelling rate close to the reactor irradiation. Ion irradiation at other temperatures have suppressed swelling.

5.4. Discussion

In the quasi-continuum reaction rate theory, the basic point defect reaction equations can be solved to obtain solutions under a steady state in which defect generation, point

defect recombination, and point defect absorption by sinks such as dislocations and voids reach a balance. Solutions allow the estimation of defect flux towards different types of sinks, or the integrated total defects absorbed/recombined through different reactions. These quantities or combinations of the quantities can be used as invariants to calculate the adjustment needed for one parameter in order to compensate for the effects from the other parameters. For void swelling, the invariant is the net flux of vacancies over interstitials to voids. Under different irradiation conditions involving different dpa rate, the temperature shifting for equivalent swelling is [14]:

$$T_2 - T_1 = \frac{\frac{kT_1^2}{E_v^m + nE_v^f}\ln\left(\frac{G_2}{G_1}\right)}{1 - \frac{kT_1}{E_v^m + nE_v^f}\ln\left(\frac{G_2}{G_1}\right)} \qquad \text{(Eq. 5.1)}$$

Where T is irradiation temperature, k is Boltzmann's constant, E_v^m is the vacancy migration energy, E_v^f is the vacancy formation energy, and G is the point defect generation rate. The value of n depends on primary defect removal model. $n = 2$ for recombination dominant case and $n = 1$ for sink dominant case [14].

Using $\frac{G_2}{G_1} = \frac{1.7\times10^{-3} dpa}{3.2\times10^{-7} dpa}$ as the ratio of dpa rates of ion irradiation to neutron irradiation, $T_1 = 450℃$, $E_v^m = 1.3\ eV$, [15] $E_v^f = 1.9\ eV$ [16], and $n = 1$, Eq. 5.1 gives a value for $T_2 = 594℃$, which is very close to the highest irradiation temperature 600℃.

5.5. Conclusions

The combination of neutron irradiation and ion irradiation as a hybrid approach can significantly reduce testing cost and speed up nuclear materials development. In this "neutron-preconditioned ion irradiation", 304 stainless steels was irradiated using the EBR-II fast rector to develop phase changes and void nucleation characteristic of rector environment, then ion irradiation with a damage introduction rate about four orders of magnitude higher was used to emulate neutron damage. The emulation requires temperature adjustment to compensate the effects from large dpa rate difference. An insufficient adjustment leads to swelling reduction or saturation at higher damage level. With sufficient adjustment and the technique to identify the safe analysis zones not affected by either surface effect or the injected interstitial effect, swelling vs. dpa curve can be extracted from a single ion irradiation experiment and this agrees well with the suggested temperature from rate theory calculations.

5.6. References

1. F. A. Garner and J. J. Laidler, Proceedings of Workshop on Correlation of Neutron and Charged Particle Damage, Oak Ridge, TN, June 4, 1976, pp. 177-240.

2. G.S. Was, "Fundamentals of radiation materials science: metals and alloys", Springer, New York, 2007

3. L.K. Mansur, J. Nucl. Mater. 78 (1978) 156-160.

4. Y. Huang, J.M.K. Wiezorek, F.A. Garner, P.D. Freyer, T. Okita, M. Sagisaka, Y. Isobe, T.R. Allen, Microstructural characterization and density change of 304 stainless steel reflector blocks after long-term irradiation in EBR-!!, Journal of Nucl. Mat. 465, 516-530 (2015).

5. Y. Dong, B.H. Sencer, F.A. Garner, E.A. Marquis, Microchemical and microstructural evolution of AISI 304 stainless steel irradiated in EBR-II at PWR-relevant dpa rates, J. Nucl. Mat. 467, 692-702 (2015).

6. J.F. Ziegler, M.D. Ziegler, J.P. Biersack. SRIM–The stopping and range of ions in matter (2010), Nuclear Instruments and Methods in Phys. Res. B 268, 1818-1823 (2010).

7. A.Yu. Konobeyev, U. Fischer, Y.A. Korovin, S.P. Simakov, Evaluation of effective threshold displacement energies and other data required for the calculation of advanced atomic displacement cross-sections, Nuclear Energy and Technology 3, 169–175 (2017).

8. Jonathan Gigax, Eda Aydogan, Tianyi Chen, Di Chen, Lin Shao, Y. Wu, W.Y. Lo, Y. Yang, F.A. Garner, The influence of ion beam rastering on the swelling of self-ion irradiated pure iron at 450°C, J. Nucl. Mater. 465, 343-348 (2015).

9. Jonathan G. Gigax, Hyosim Kim, Eda Aydogan, Frank A. Garner, Stu Maloy, Lin Shao, Beam-contamination-induced compositional alteration and its neutron-atypical consequences in ion simulation of neutron-induced void swelling, Mat. Res. Lett. 5, 478-485 (2017).

10. L. Shao, Jonathan Gigax, Di Chen, Hyosim Kim, Frank A. Garner, Jing Wang, Mychailo B. Toloczko, Standardization of accelerator irradiation procedures for simulation of neutron induced damage in reactor structural materials, J. Nucl. Mater. 409, 251-254 (2017).

11. C.A. Schneider, W.S. Rasband, K.W. Eliceiri, NIH Image to ImageJ: 25 years of image analysis, Nature Methods 9, 671-675, 2012.

12. D.L. Plumton, W.G. Wolfer, Suppression of void nucleation by injected interstitials during heavy ion bombardment, J. Nucl. Mat. 120, 245-253 (1984).

13. Yongchang Li, Aaron French, Zhihan Hu, Adam Gabriel, Laura R. Hawkins, Frank A. Garner, Lin Shao, A quantitative method to determine the region not influenced by injected interstitial and surface effects during void swelling in ion-irradiated metals, submitted to J. Nucl. Mat.

14. L.K. Mansur, Correlation of neutron and heavy-ion damage II. The predicted temperature shift if swelling with changes in radiation dose rate, J. Nucl. Mat. 78, 156-160 (1978)]

15. M Kiritani, H. Takata, J. Nucl. Mat. 277, 69-70 (1978)

16. N.O. Lam, A. Kumar, H. Wiedersich, in: H.R. Brager, J.S. Perrin (Eds.), Effects of Radiation on Materials: Eleventh Conf., ASTM STP 782, American Society for Testing and Materials, 1982, p. 985.

6. CONCLUSIONS

The radiation damage community has sought to use ion irradiations to fill a major gap in testing swelling resistance of reactor alloys. While this is an alternative with a lot of advantages, there are also significant neutron-atypical variables that must be accounted for if the results are to have predictive power. These include damage rate effects, microchemical phase changes, the injected interstitial effect, and the surface effect. This thesis addressed the credibility of ion simulation of swelling applied to neutron environments by presenting a series of ion irradiations on the simple chemical system of relatively pure iron across a range of irradiation conditions. A method was proposed to quantitatively identify a "safe analysis" zone within ion irradiated samples by looking at the void sizes and densities plotted against the local dpa. This surface influence was further refined and the safe zone boundary confirmed by investigating the effect of free surfaces on void denuded zones across a range of energies, temperatures and rates. The TEM measured void denuded zones were found to be linearly proportional to $\left(\frac{exp\left(-\frac{E}{kT}\right)}{K}\right)^{1/4}$ and the surface effected regions were found to be approximately twice the denuded zone width. Lastly, a systematic study of 5MeV Fe^{2+} irradiations helped identify key parameters, particularly some of the interplay between temperature and dpa rate influences on the interjected interstitial effect. The experimental results were also further confirmed and explained by modeling.

Finally, the insights gained from the initial three portions of this work were applied to a combination of neutron irradiation and ion irradiation as a hybrid approach. In this

"neutron-preconditioned ion irradiation", 304 stainless steels were irradiated using the EBR-II fast rector to develop phase changes and void nucleation characteristic of rector environment, then ion irradiation with a damage introduction rate about four orders of magnitude higher was used to emulate neutron damage. The emulation required temperature adjustment to compensate for the effects from large dpa rate differences. An insufficient adjustment can lead to swelling reduction or saturation at higher damage level. With sufficient adjustment and the insights gained from the pure iron portion of this work to identify the safe analysis zones not affected by either surface effect or the injected interstitial effect, swelling vs. dpa curves were extracted from a single ion irradiation set of experiments and this agrees well with the suggested temperature from rate theory calculations. It also agrees closely with neutron data from very similar alloys.

The insights gained and method developed using a simple model material (pure Fe) in this thesis work have been successfully applied to a complex reactor-relevant material. By refining how the ion irradiation community can account for the neutron atypical variables of damage rate effects, microchemical phase changes, the injected interstitial effect, and the surface effect, this work will strongly impact the use of ion irradiations to optimally emulate neutron damage, in both fundamental understanding and new testing method development.